



**Spectral Diagnostics, Ion Stopping Power,
and Radiation-Hydrodynamics Modeling in
Support of Sandia Light Ion Beam Fusion
Experiments**

J.J. MacFarlane, P. Wang, H.-K. Chung, G.A. Moses

April 1995

UWFDM-979

***FUSION TECHNOLOGY INSTITUTE
UNIVERSITY OF WISCONSIN
MADISON WISCONSIN***

DISCLAIMER

This report was prepared as an account of work sponsored by an agency of the United States Government. Neither the United States Government, nor any agency thereof, nor any of their employees, makes any warranty, express or implied, or assumes any legal liability or responsibility for the accuracy, completeness, or usefulness of any information, apparatus, product, or process disclosed, or represents that its use would not infringe privately owned rights. Reference herein to any specific commercial product, process, or service by trade name, trademark, manufacturer, or otherwise, does not necessarily constitute or imply its endorsement, recommendation, or favoring by the United States Government or any agency thereof. The views and opinions of authors expressed herein do not necessarily state or reflect those of the United States Government or any agency thereof.

**Spectral Diagnostics, Ion Stopping Power, and
Radiation-Hydrodynamics Modeling in Support
of Sandia Light Ion Beam Fusion Experiments**

J. J. MacFarlane, P. Wang, H.-K. Chung, G. A. Moses

Fusion Technology Institute
University of Wisconsin-Madison
1500 Johnson Drive
Madison, WI 53706

April 1995

UWFDM-979

Contents

1. Introduction	1
2. Analysis of Flat-Foil K_α Experiments on PBFA-II	4
2.1. Radiation-Hydrodynamics Models	4
2.2. Radiation-Hydrodynamic Simulations of PBFA-II Flat-Foil K_α Experiments	6
2.3. Comparison of Experimental and Simulated K_α Satellite Spectra	25
2.4. Simulation of Higher Intensity Li Beams	35
3. An Unified Self-Consistent Field Model for Ion Energy Deposition in Ion-Driven Inertial Confinement Fusion Targets	37
3.1. Introduction	37
3.2. Lindhard's Formalism of Stopping Power and Local Density Approximation	39
3.3. Atomic Model And Electron Density Distribution Function	40
3.4. The Random-Phase-Approximation Stopping Interaction Function	44
3.5. Numerical Results	49
3.6. Summary	57
Appendix A.	62
Time-Dependent Collisional-Radiative Modeling for Analyzing Spectra Obtained in Light Ion Fusion Experiments	62
Appendix B.	63
K_α Spectral Diagnostics for Mg and Al Plasmas Irradiated by Intense Li Beams	63

1. Introduction

The purpose of this report is to summarize work performed by the University of Wisconsin during March 1994-March 1995 in support of beam-plasma interaction experiments at Sandia National Laboratories. During the past 4 years we have developed detailed collisional-radiative equilibrium (CRE) and atomic physics codes which have been used to analyze spectra obtained in PBFA-II experiments. In the past year, we have made substantial improvements in our capabilities for modeling: (1) ion stopping powers, (2) radiation-hydrodynamics of beam-heated plasmas, and (3) time-dependent collisional-radiative processes in anode and gas cell plasmas. A description of the modeling improvements and their application to Sandia light ion beam experiments is described in this report.

The tasks for the March 1994-March 1995 period are listed in Table 1.1. The first two tasks concern the analysis of K_α emission spectra in PBFA-II Li beam experiments. These spectra were obtained in experiments using planar, “plastic sandwich” targets (CH : Au : Al : CH). In these experiments, the Al provides diagnostic information about the plasma conditions from its K_α emission spectra, while the Au layer — via Rutherford scattering — provides diagnostic information about the Li beam characteristics. Additional experiments with mixed Mg/Al tracer layers were attempted, but useful K_α spectral measurements as yet have not been successfully obtained. Nevertheless, the calculations of Mg K_α spectra discussed in this report should be applicable to future experiments.

In Section 2, radiation-hydrodynamic simulations and spectral calculations for the flat-foil K_α experiments are described. The primary input data to the calculations are the time-dependent Li beam voltage and current density. The ion energy is deposited in the target using a stopping power model based on the work of Mehlhorn [1]. The resulting time-dependent temperature and density distributions, as well as the beam voltage and power density in the Al layer, were post-processed with our CRE model to predict K_α emission spectra. Synthetic time-integrated spectra were then obtained for direct comparison with experimental data by post-processing the computed CRE spectra, and adding the effects of instrumental broadening. Well-diagnosed experiments of this type are very valuable because good agreement between the calculated and measured K_α spectra suggests a good understanding of key physics issues for light ion beam fusion [2] including: (1) coupling of the Li beam energy to the target; (2) energy transport within the target; (3) atomic processes affecting the target emission spectra; (4) the ability to diagnose the Li beam properties; and (5) the ability to spectroscopically diagnose the target plasma conditions. Comparisons between calculated and measured K_α spectra for PBFA-II Shots 5851, 5846, and 6347 are shown in Section 2. Results are also shown for targets heated by Li beams with higher intensities to provide predictions for future experiments.

Table 1.1. Tasks for March 1994–March 1995

-
1. Generate atomic models for target materials and compute relevant beam-plasma interaction cross sections for predicting inner-shell line emission.
 2. Analyze spectral data obtained in PBFA-II experiments. Perform CRE calculations to determine plasma conditions obtained in experiments — especially for two-material experiments (e.g., Mg and Al).
 3. Develop a time-dependent collisional-radiative model for analyzing spectra obtained in intense light ion beam experiments.
 4. Document results in final report to Sandia National Laboratories.
-

In Section 3, we describe a new approach for calculating ion stopping powers using a unified self-consistent field model. This approach utilizes a muffin tin atomic model to compute finite temperature electron distributions for the target plasma and a full Random-Phase-Approximation stopping interaction function. The primary strengths of the model are that: (1) it includes the stopping effects of electrons in ground state, excited states, and continuum states in a self-consistent manner; thus, the “bound” and “free” electrons are not treated separately; and (2) it provides a physically consistent picture at both high and low projectile energies so that a smooth transition occurs between the LSS and Bethe limits. Results for Al and Au target plasmas are presented in Section 3.

In Appendix A, sample results from our initial time-dependent collisional-radiative calculations to study the ionization dynamics of SABRE anode plasmas are presented. These results were presented at the American Physical Society Division of Plasma Physics Meeting in November 1994 at Minneapolis, MN [3]. This model is being developed by H.-K. Chung as part of her Ph.D. dissertation research, which will focus on the spectral analysis of PBFA-II Ar gas cell data and its implications for light ion beam transport. The model is similar to that of our collisional-radiative equilibrium (CRE) code [4,5], except that time-dependent multilevel atomic rate equations are solved as opposed to steady-state rate equations. The model also uses the same detailed atomic data bases [6,7] as used by our CRE code. Initial calculations have been performed for SABRE anode plasmas. In addition, we have made several comparisons with previous calculations [8]. A more detailed discussion of the anode plasma work will be presented in the future.

Finally, in Appendix B, we present results from K_{α} spectral calculations for Mg-Al targets irradiated by intense Li beams. The work was presented at the 10th International Conference on High Power Particle Beams in June 1994 at San Diego, CA.

2. Analysis of Flat-Foil K_α Experiments on PBFA-II

Radiation-hydrodynamic simulations of PBFA-II Li beam experiments with flat-foil (“plastic sandwich”) targets were performed using our BUCKY-1 simulation code [9]. The goal is to determine whether the temperatures predicted in the Al layers in the radiation-hydrodynamics simulations — which utilize measured beam parameters as input — are consistent with measured time-integrated K_α satellite emission spectra. Time-dependent Li beam voltages and current densities from several PBFA-II shots [10] were used in the simulations.

The major features of the radiation-hydrodynamics models are described in Section 2.1. Results from radiation-hydrodynamics simulations of PBFA-II Shots 5851, 5846, and 6347 are discussed in Section 2.2. At selected simulation times, the temperature, density, beam voltage, and beam current density profiles in the Al layer were post-processed using our CRE code to compute K_α satellite spectra. Comparisons of the calculated and measured K_α spectra are shown in Section 2.3. Several simulations were also performed for relatively high intensity Li beams to estimate target plasma conditions which could be achieved in future experiments. These results are described in Section 2.4. A discussion of spectral calculations for Mg/Al foils is presented in Appendix B.

2.1. Radiation-Hydrodynamics Models

Calculations were performed using the BUCKY-1 radiation-hydrodynamics code. As is illustrated in Fig. 2.1, this code integrates physics models from several codes: PHD-IV, CONRAD, NLTERT, and EOSOPA. PHD-IV [11] is an ICF target physics code which simulates implosions, explosions, ion beam energy deposition, fusion burn, charged particle transport, and target breakup. It is a 1-D Lagrangian code which solves the single-fluid equation of motion with pressure contributions from electrons, ions, radiation, and fast charged particle reaction products. Energy transport in the plasma is treated with a two-temperature model — i.e., separate ion and electron temperatures. Radiation emission and absorption terms couple the electron temperature equation to the radiation transport equations. Radiation is transported using a choice of several models: (1) a multigroup Eddington factor model; (2) a multigroup diffusion model; (3) a multiangle, multigroup model based on the method of short characteristics [12]; or (4) an escape probability model [13,14] for detailed line radiation transport.

CONRAD [15] is a 1-D radiation-hydrodynamics code which descended from PHD-IV and MF-FIRE [16]. It is used to study the radiative and hydrodynamic processes within ICF target chambers following the explosion of a high-gain target. It includes models to simulate the stopping of target x-rays and fast debris ions in a buffer gas and the target chamber first wall. Time-dependent vaporization of the first wall is also simulated.

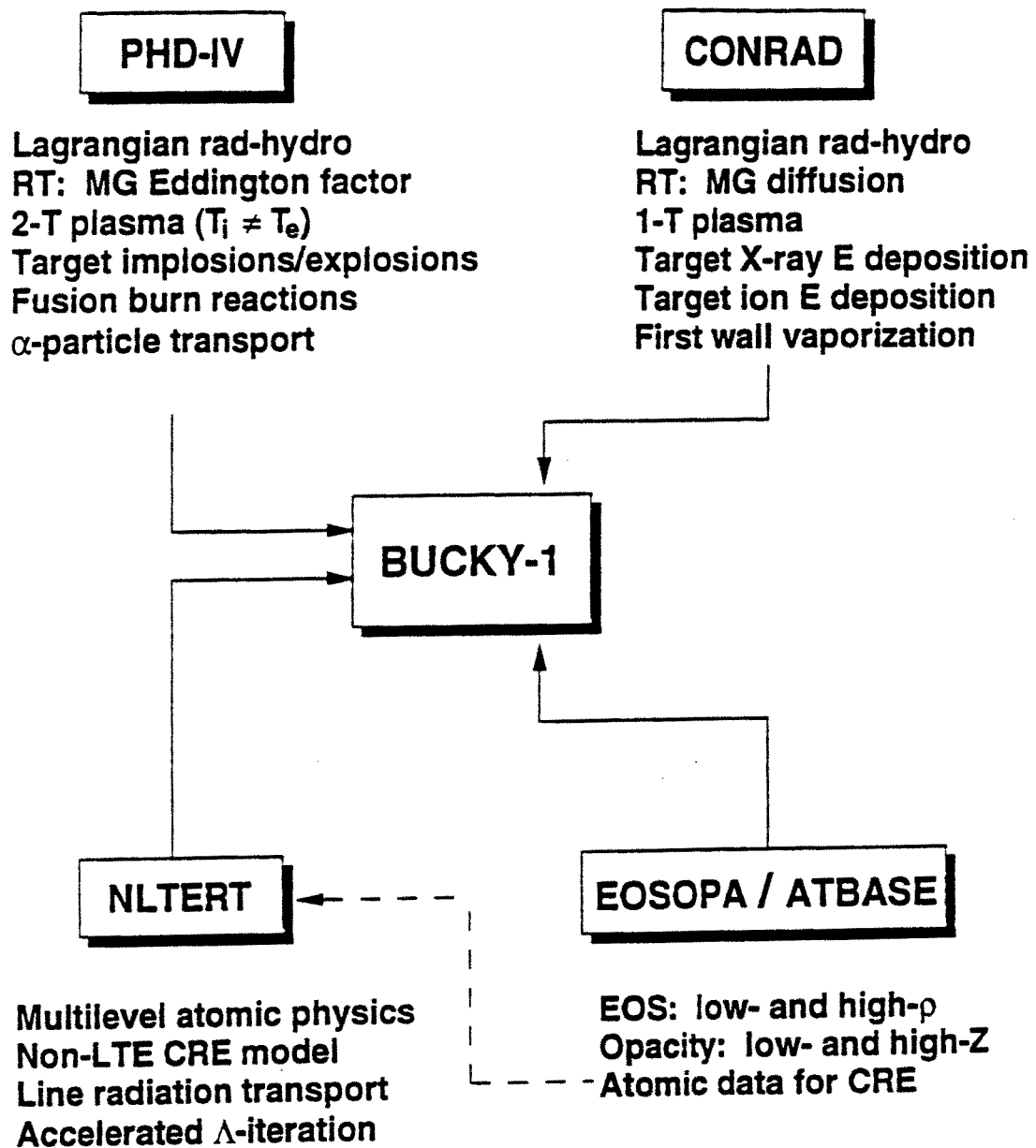


Figure 2.1. Schematic illustration of codes used to build the BUCKY-1 radiation-hydrodynamics code.

NLTERT [5] is a non-LTE radiative transfer code which has been used to analyze spectra obtained in laboratory plasma experiments. Selected parts of this code were recently incorporated into BUCKY-1 [17]. When this model is invoked, atomic level populations are calculated using a collisional-radiative equilibrium (CRE) model at each hydrodynamic time step. By default, the atomic populations are computed self-consistently with the radiation field; however, options also exist where the user can specify that LTE (local thermodynamic equilibrium) populations or optically thin populations (i.e., where photoexcitation and photoionization are neglected) be used. After the atomic level populations are computed, radiation losses due to line emission are computed using an escape probability radiation transport model. This model was also recently used to study radiation transport effects in ICF target chambers with a single-species buffer gas [18].

EOSOPA [19] and ATBASE [7] are a suite of atomic physics codes which generate atomic data for equations of state, multigroup opacities, and spectral analyses. Equation of state tables are generated using a hybrid model in which high-density thermodynamic properties are calculated using a muffin-tin model, while lower density properties are computed using a detailed configuration accounting (DCA) model. Example results from EOSOPA are shown in Fig. 2.2, which shows energy and pressure isotherms for Al. In the low-density regime, the nonlinear behavior due to ionization/excitation is clearly seen. The cohesive, degenerate, and pressure ionization effects are also apparent for the high-density regime. EOSOPA also computes high quality opacities for both low-Z and high-Z materials.

2.2. Radiation-Hydrodynamic Simulations of PBFA-II Flat-Foil K_α Experiments

Figure 2.3 shows a schematic illustration of the plastic sandwich targets used in the PBFA-II experiments, along with the layer thicknesses used to simulate Shots 5851, 5846, and 6347. Unless otherwise noted, the following assumptions and options were used in our radiation-hydrodynamics simulations. In particular, we address the areas which significantly impact the predicted target temperature: the beam parameters, the stopping power model, and the radiation physics. Radiation was transported using a multigroup, multiangle model based on the method of short characteristics. A radiation diffusion model was not used because the continuum for the lower-Z regions was optically thin over a large part of the spectrum. For the Au region, opacities — which include contributions from bound-bound, bound-free, and free-free transitions — were computed using an unresolved transition array (UTA) model [19]. For the CH and Al regions, the line and continuum radiation were treated separately. This was done to avoid overestimating radiation losses from the low-Z regions. Continuum radiation from the low-Z regions was transported using the same model as for the Au.

For most of the calculations described in this section, line radiation effects from the low-Z layers were neglected. This was done in order to save computer time while assessing the effects of various physical processes. When it was included, line radiation was transported using a frequency-

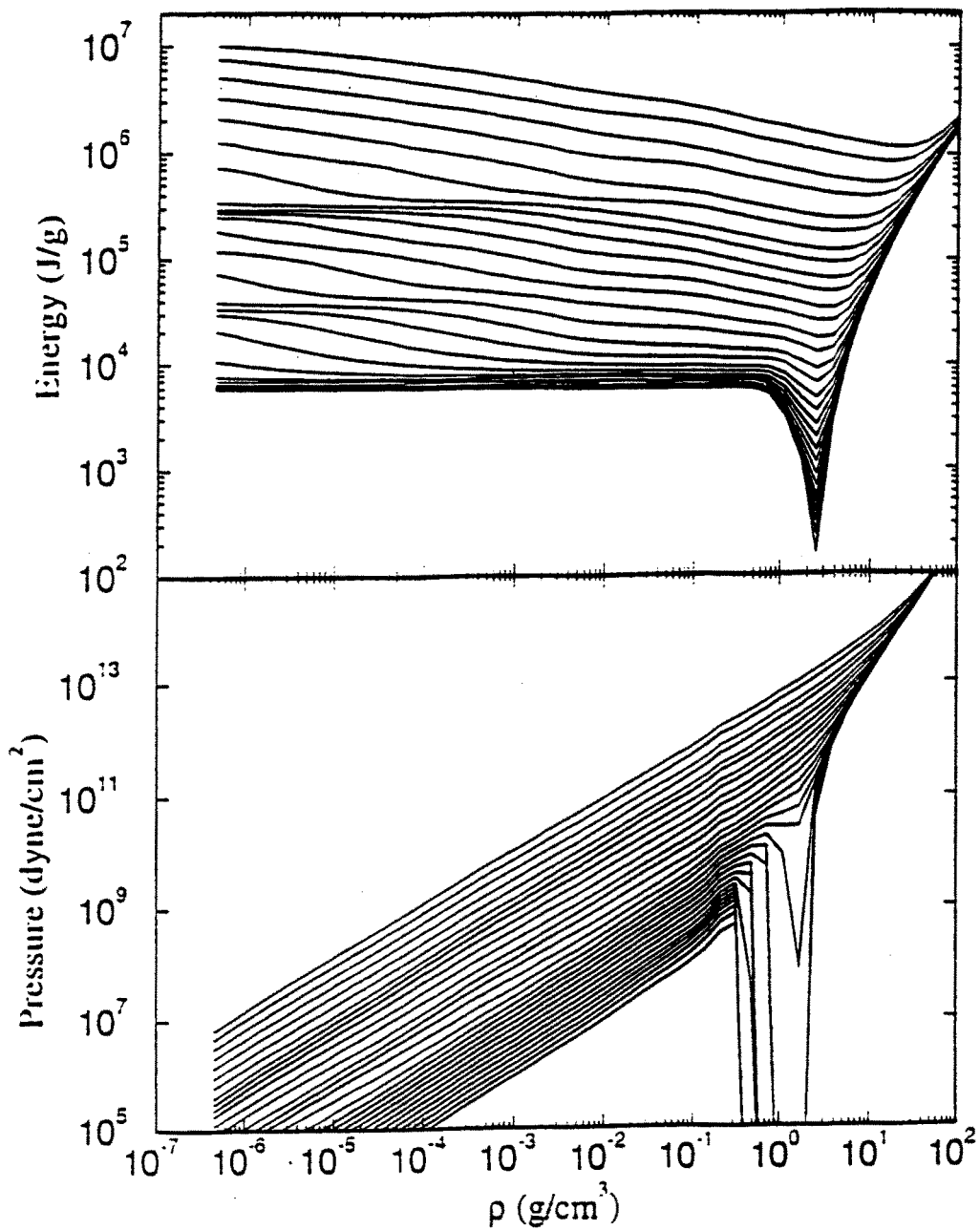
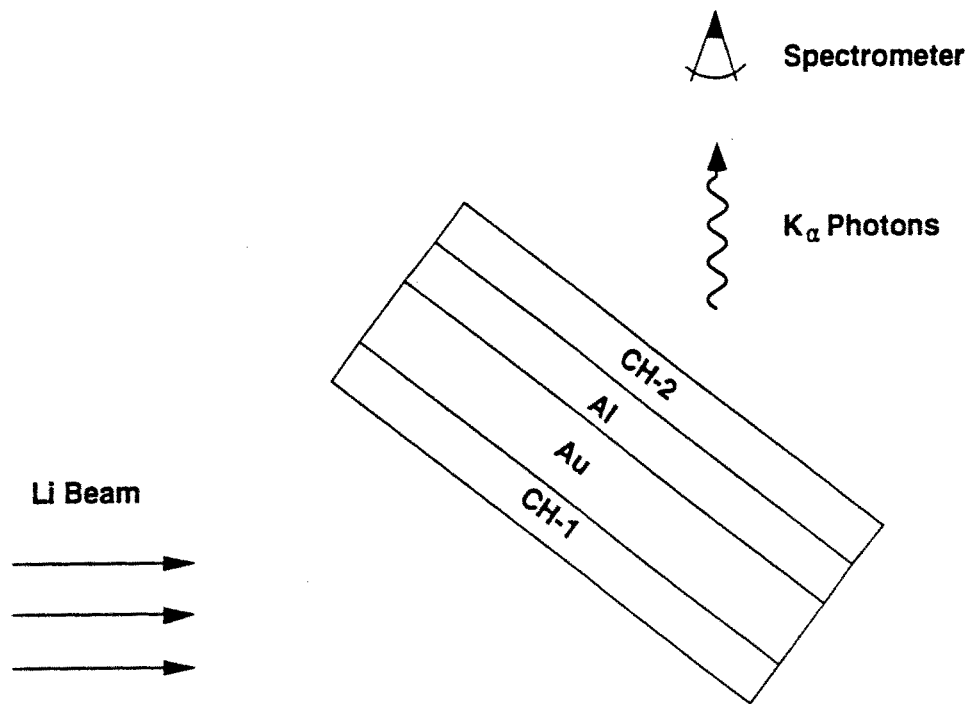


Figure 2.2. EOSOPA hybrid model equation of state for Al. Isotherms of total energy density and pressure.



PBFA-II Shot	Thickness (μm)			
	CH-1	Au	Al	CH-2
5851	0.14	0.54	0.18	0.14
5846	0.14	0.56	0.19	0.14
6347	0.12	0.55	0.70	0.12

Figure 2.3. Initial target thicknesses used in simulation of PBFA-II flat-foil target experiments.

and angle-averaged escape probability model in which each line is transported individually. This requires knowing the atomic populations and opacities for each line. Atomic level populations were computed at each hydrodynamic time step using a CRE model, which included effects of resonant self-absorption. Line profiles include the effects of natural, Doppler, and Stark broadening. Because of the hybrid nature of the model, line radiation which escaped a material region was assumed to escape the entire target (e.g., Al line radiation was not reabsorbed by the Au). In addition, low-Z line opacities did not contribute to radiative heating. Thus, the low-Z lines did not see radiation from the Au. For the CRE line transport calculation, the atomic model consisted of 175 levels and 267 lines for Al, 71 levels and 254 lines for C, and 7 levels and 15 lines for H.

The stopping power model is based on the method developed by Mehlhorn [1]. However, we use an adjusted stopping power because the experiment was not truly 1-D because the beam hits the planar target at a 45° angle. To compensate for this, we multiplied the stopping power, (dE/dx) , by a constant determined by SOPHIA particle-in-cell (PIC) calculations [10]. The constant was determined by equating the beam energy deposited per unit mass calculated with the PIC code using the experimental geometry, to that using an enhanced beam power density for a geometry in which the incident beam is normal to the target surface (which is the geometry used in the 1-D radiation-hydrodynamic simulations). The (dE/dx) multipliers for PBFA-II Shots 5846, 5851, and 6347 are 1.535, 1.500, and 1.530, respectively. Note that these numbers are several percent larger than $\sqrt{2}$, which accounts for the 45° tilt of the target with respect to the beam. The additional enhancement occurs due to “focusing” effects, in which the beam ions above and below the plane of the target converge at the target (additional heating can occur because ions can cross paths, instead of having parallel trajectories).

In accounting for the 45° angle of incidence of the beam, one has a choice of enhancing either the beam current density or the stopping power to attain a specific energy deposition rate consistent with the PIC calculations. We chose to enhance the stopping power because this should more accurately simulate the energy loss of an ion in a given layer. That is, the energy loss in a layer of thickness ΔL is:

$$\Delta E = \left(\frac{dE}{dx} \right) \left(\frac{\Delta L}{\cos \theta} \right),$$

where θ is the beam angle of incidence with respect to normal. Since $\theta = 0$ in our radiation-hydrodynamics simulations, one can get the appropriate ΔE by enhancing (dE/dx) .

The Li beam parameters are constrained by PBFA-II ion diagnostics (magnetic spectrometer, ion movie camera, etc.). In our radiation-hydrodynamics simulations we assume a monoenergetic Li beam which is fully ionized. Time-dependent beam power densities and voltages incident at the target surface were tabulated from SOPHIA runs [10]. In deriving the beam parameters at the target surface, corrections for enhanced stopping power due to the heated target plasma were also included.

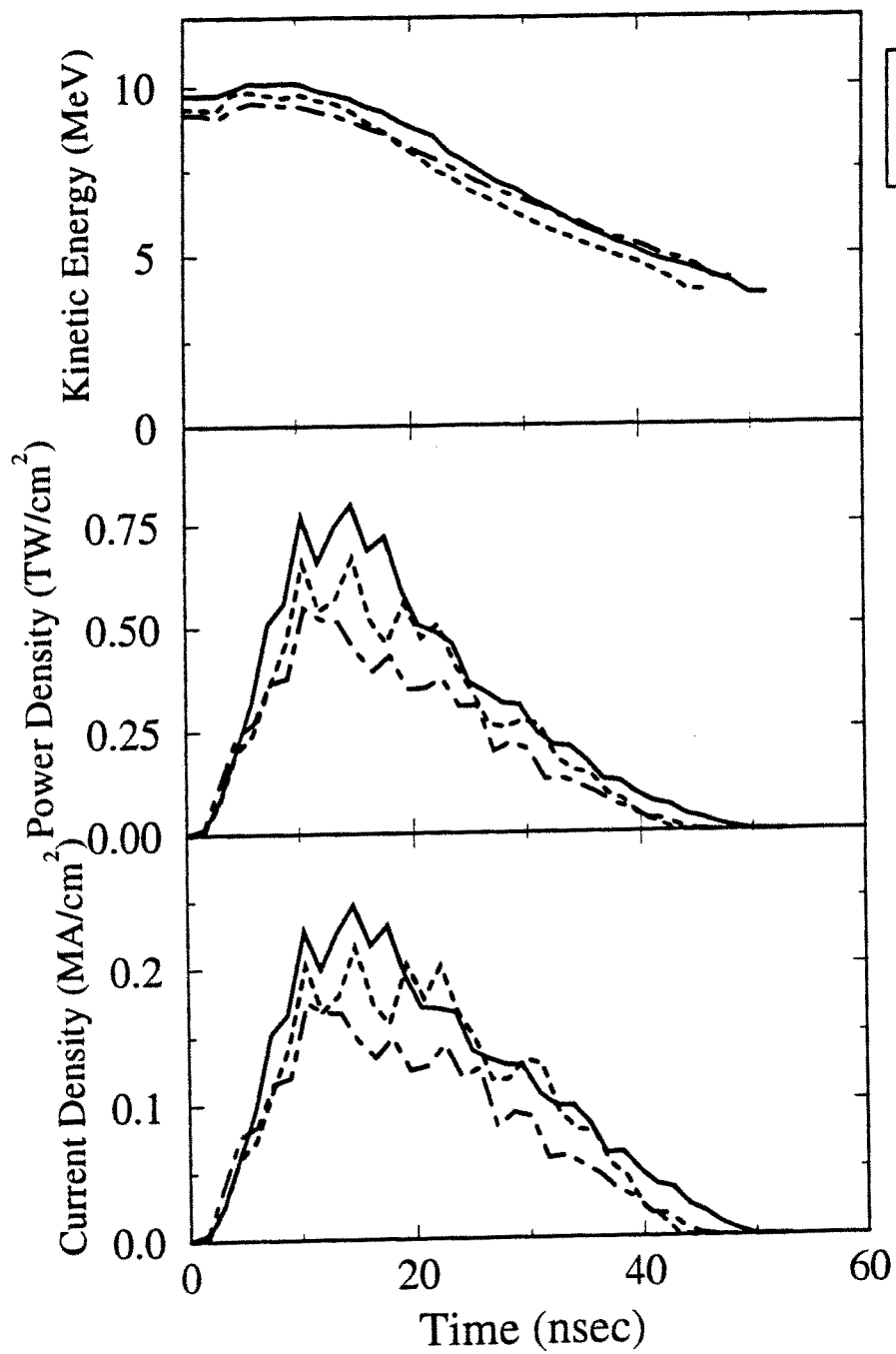


Figure 2.4. Beam parameters incident on the target surface in radiation-hydrodynamic simulations of Shots 5851, 5846, and 6347. From [10].

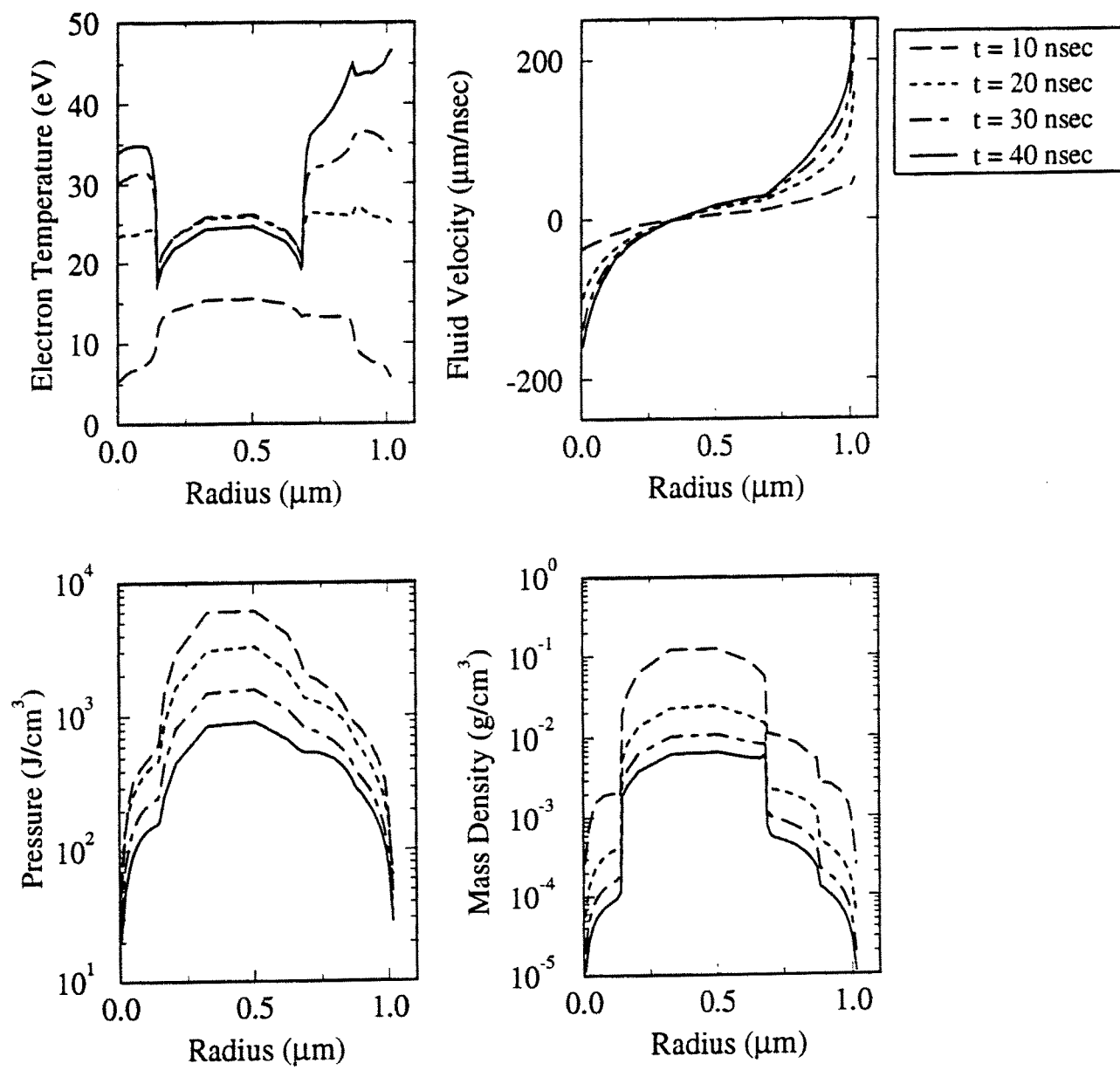


Figure 2.5. Spatial distributions of electron temperature, pressure, fluid velocity, and mass density at times of 10, 20, 30, and 40 ns for the Shot 5851 baseline simulation.

The beam parameters used in the radiation-hydrodynamic simulations of Shots 5846, 5851, and 6347 are shown in Fig. 2.4, where the Li beam voltage, power density, and current density incident on the target surface are shown as a function of time. (These times have an offset of 50–60 ns with respect to the SOPHIA output; the beam “turns on” at $t = 0$ in the hydro simulations.) In each case the Li beam voltage starts at approximately 10 MeV and then decreases with time. The beam power and current densities peak between 10 and 20 ns before decreasing at later times. Figure 2.4 shows the peak power densities were approximately 0.8, 0.7, and 0.55 TW/cm² for Shots 5851, 5846, and 6347, respectively, while the corresponding peak current densities were 0.25, 0.21, and 0.17 MA/cm². Note that for these shots only one quarter of the PBFA-II beam irradiated the target, and that the target in each case was tilted at an angle of 45° with respect to the vertical. It is also important to note that the maximum temperature in the Al region of the target is not attained until roughly 40 ns. Thus, diagnosing the behavior of the beam at late times is important for obtaining a good understanding of these flat-foil experiments.

Before doing a shot-to-shot comparison, let us first examine the particular case of 5851 in detail to assess the importance of various physical processes in these experiments. Figure 2.5 shows the temperature, pressure, fluid velocity, and mass density distributions at simulation times of 10, 20, 30, and 40 ns. The results are plotted as a function of their original (pre-expansion) positions in the target, which were 0–0.14 for the first plastic tamper, 0.14–0.68 for Au, 0.68–0.86 for Al, and 0.86–1.0 for the second plastic tamper. (Results are not displayed in the usual manner of areal mass density (g/cm²) because the details of the low- Z regions are more difficult to see.) A clearer picture of the time-dependent temperature in each region is shown in Fig. 2.6, where the mean temperature (mass-weighted average over hydro zones) of each of the target layers is plotted as a function of time. Here, it is seen that the temperature in all regions increases during the first 20 ns. After 20 ns the temperature of the Au is roughly constant out to about 40 ns, and later decreases.

The Au remains at a lower temperature than the Al and CH regions (CH-1 \equiv the tamper facing the incoming Li beam) because the lower- Z materials are less efficient radiators. The Au is optically thick at virtually all frequencies (the exception being extremely high frequencies), and thus radiates like a blackbody. The same is not true for Al and CH, which has been discussed previously [20]. This can be understood by examining Fig. 2.7, which shows a calculated emission spectrum for an Al plasma at $T = 30$ eV and $n = 1 \times 10^{20}$ ions/cm³. The plasma thickness is 120 μ m, which corresponds to a solid density (pre-expansion) thickness of 2000 Å. The lower plot in Fig. 2.7 shows the frequency-dependent optical depths for the same calculation. Only for the strongest optically thick lines does the flux approach the Planckian (blackbody) flux. The continuum, however, is optically thin over much of the spectrum, and because of this the emitted flux is substantially lower than the Planckian value. This allows the temperatures of the Al and

CH regions to rise to a higher temperature. Note that this also presents challenges for accurately simulating the radiation losses for plasmas with these conditions.

Figure 2.6 shows that for our Shot 5851 “base case”, the peak mean temperature in the Al is 40 eV, and occurs at a simulation time of about 45 ns. This is well after the peak in the Li beam intensity. The distribution of temperatures in the Al can be seen in Fig. 2.5, where at $t = 40$ ns (solid curves) the temperature in the Al is seen to range up to about 45 eV, which is $\sim 15\%$ higher than the mean temperature shown in Fig. 2.6. By comparison, the peak temperature inferred from the analysis of the K_α satellite emission spectrum for this shot is about $44 \text{ eV} \pm$ about 10–15% [20]. A direct comparison of the simulation predictions with experimental K_α spectra is described in Section 2.3.

The temperature evolution of the 2 tamper regions is seen to be very different. The tamper last hit by the beam (CH-2) reaches a substantially higher temperature than the first tamper (48 eV vs. 34 eV). This occurs because the kinetic energy of the Li beam drops significantly as it passes through the Au, which in turn leads to a higher stopping power for the second tamper region. Although the CH regions were not spectrally observed in these experiments, it seems that interesting physics experiments could be performed in which the temperatures of materials on both the incoming and outgoing sides of the Au could be inferred from their K_α spectra.

The importance of radiation losses in these experiments can be seen by examining Figs. 2.8 and 2.9. Figure 2.8 shows the energy partitioning for the total target as a function of time. The total beam energy deposited in the target is 3.5 kJ/cm^2 , which is about 22% of the total 15.9 kJ/cm^2 on target. Of this, roughly 50% is lost from the target by radiation by 40 ns. The energy contained within the target at 40 ns is 1.6 kJ/cm^2 , of which $\sim 66\%$ is in the form of internal energy (temperature plus ionization), while the remainder is in the form of hydrodynamic kinetic energy.

Figure 2.9 shows the time-dependence of the mean temperature in each of the target layers from calculations of Shot 5851 using 3 different radiation models. The upper plot shows results from our base case, which includes low- Z continuum opacities but no line transport. The bottom plot shows results from a calculation in which radiation effects in all layers were completely neglected. Thus, without radiation losses, the Au is heated to $T = 47 \text{ eV}$, which is substantially higher than the 25 eV for the base case. Similarly, the temperature in the Al layer reaches a peak of 56 eV, versus 40 eV for the base case. If the temperature inferred from the Al K_α spectral analysis of Shot 5851 is approximately correct ($T \approx 44 \text{ eV}$), these results indicate that the beam clearly has the potential of heating the Al to a temperature consistent with the observed spectrum. However, it is also clear that the predicted temperatures depend sensitively on the amount of radiative energy lost by the target plasma.

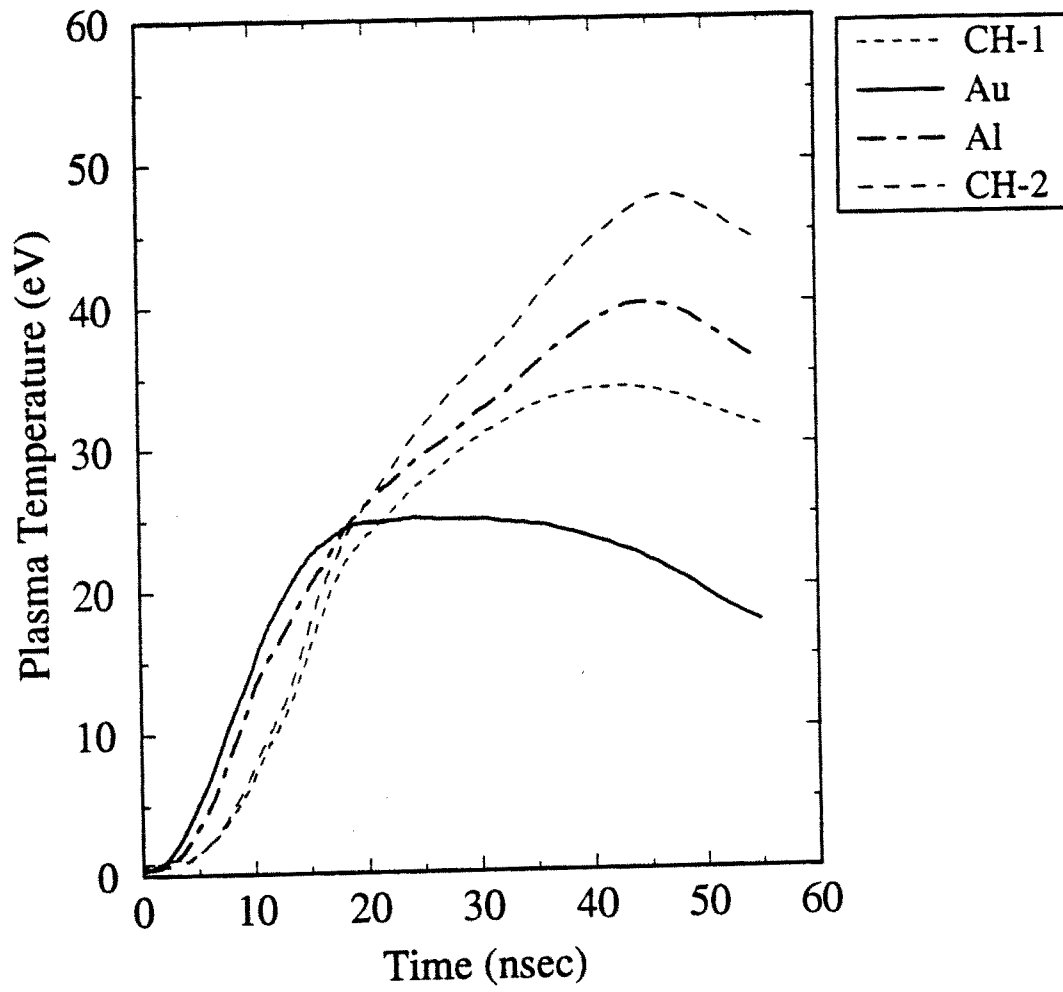


Figure 2.6. Time-dependence of spatially-averaged temperature in each target region for Shot 5851 baseline simulation.

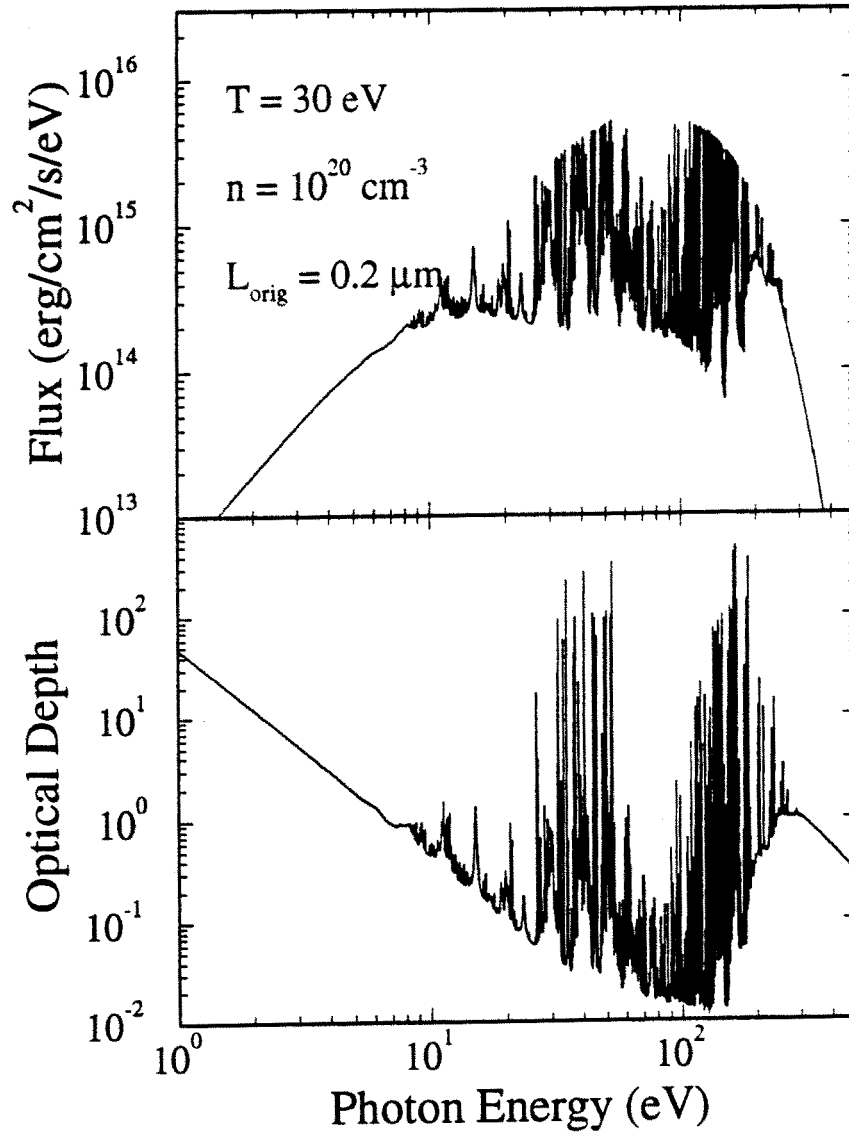


Figure 2.7. Emission spectrum and frequency-dependent optical depths calculated for an Al plasma with $T = 30 \text{ eV}$, $n = 10^{20} \text{ ions/cm}^3$, and a thickness of $120 \text{ } \mu\text{m}$.

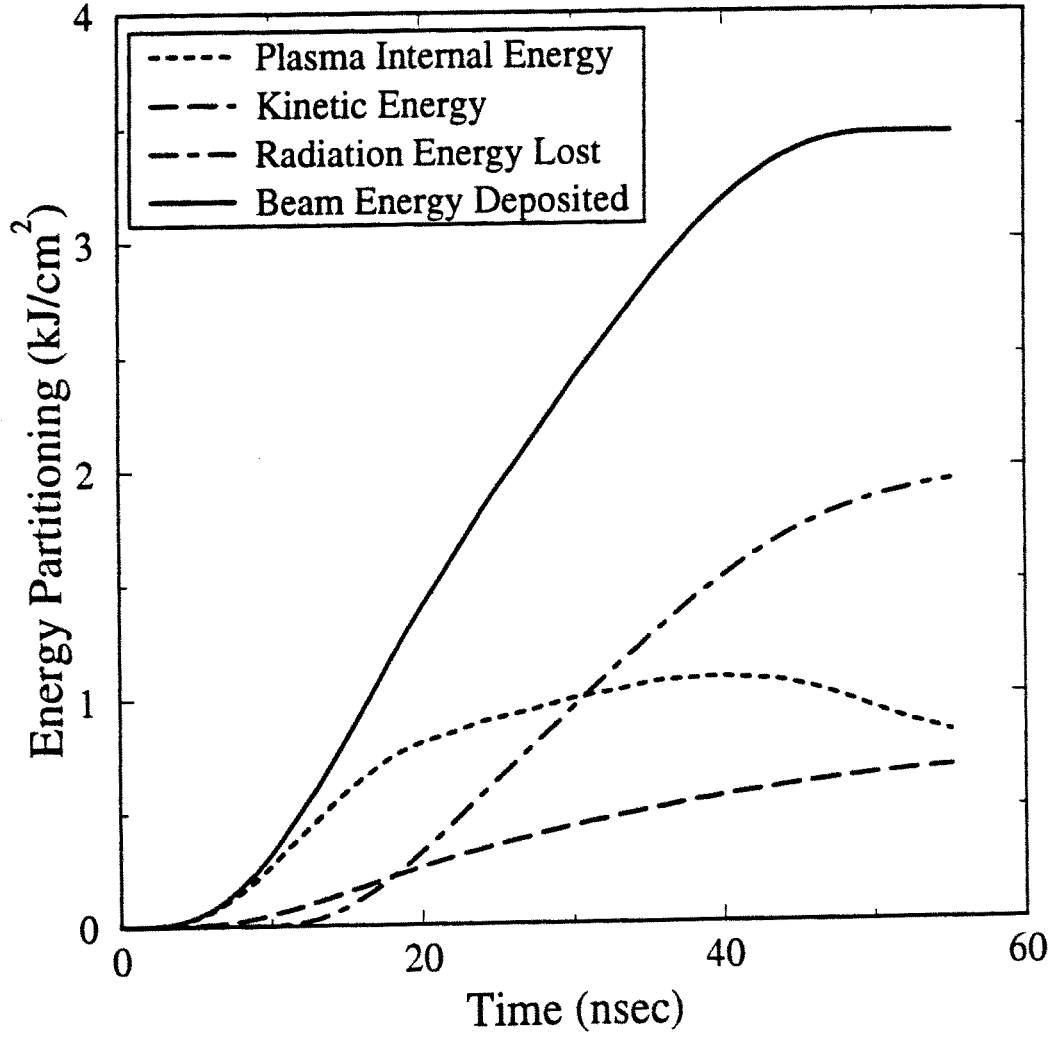


Figure 2.8. Energy partitioning in total target (all layers) from Shot 5851 baseline simulation.

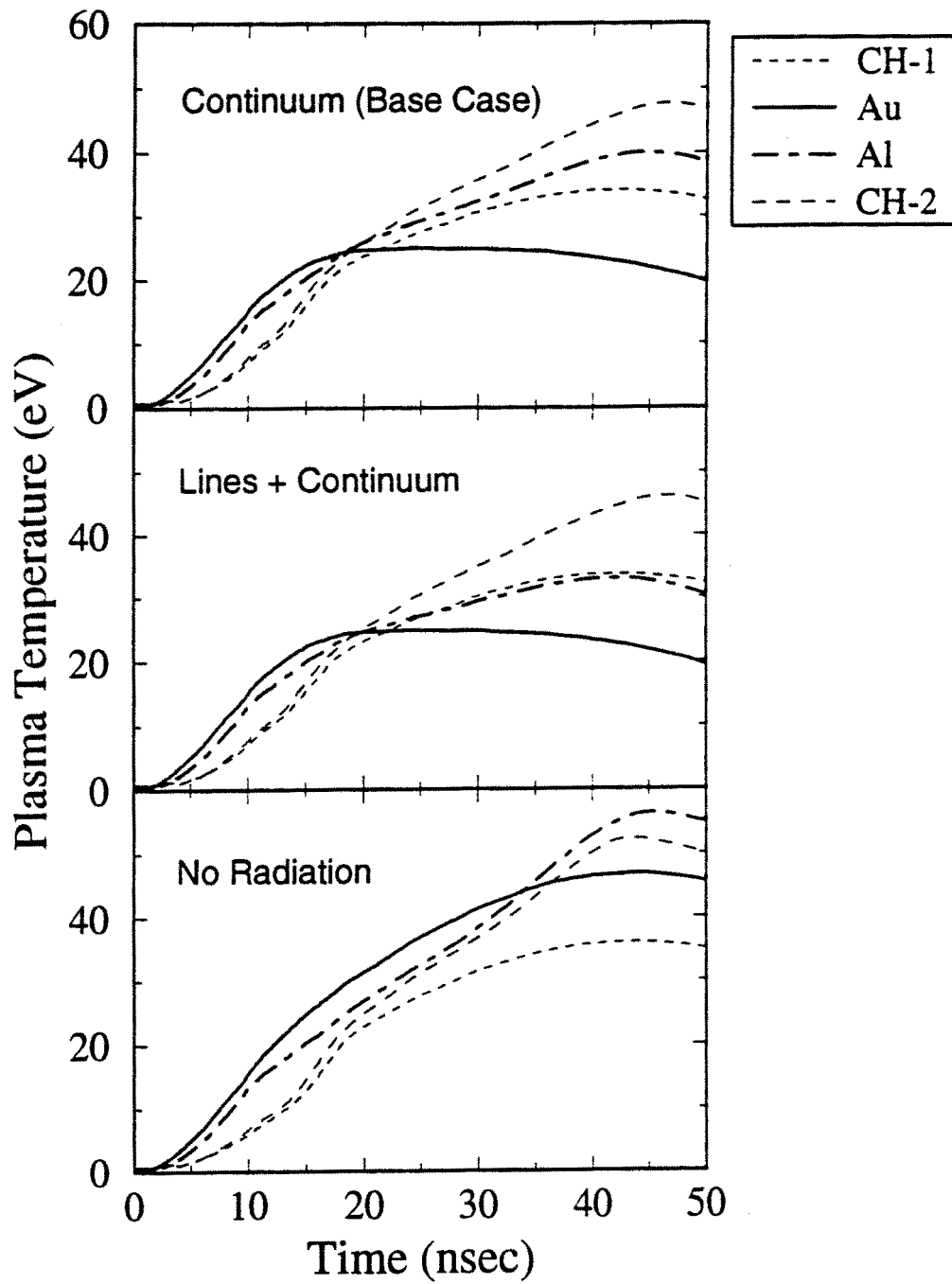


Figure 2.9. Time-dependent temperatures in target layers from 3 radiation-hydrodynamics simulations. Top: Baseline case, in which only continuum radiation transport is considered for Al and CH regions. Middle: Both lines and continuum radiation transport is included. Bottom: No radiation effects included.

The middle plot in Fig. 2.9 shows results from a calculation in which line radiation from the low- Z layers was transported using our CRE/escape probability model. This calculation results in lower temperatures for the Al and CH regions; this should be expected because only radiation *loss* effects are considered by this model. Heating of the low- Z lines due to radiation from an external source (e.g., the Au) is not included in the model. In this calculation the peak mean temperature in the Al reaches only 33 eV. One can argue that if the radiation flux from the Au exceeds the intensity in the wings of an Al line (which is where photons escape in the case of optically thick lines), then there should be net heating in that line. This effect, however, is not included in our calculations. Thus, the results in the middle and lower plots of Fig. 2.9 in a sense provide conservative lower and upper brackets arising from uncertainties in the radiation modeling.

Figure 2.10 shows the time-dependence of several quantities important for understanding the Li beam energy deposition in the target. Plotted for the Al region are the mass-weighted means for the electron temperature (in units of 10 eV), the charge state $\langle Z \rangle$, the stopping power (dE/dx) enhanced by the multiplier 1.5 to account for the incidence angle of the beam, and Li beam kinetic energy averaged over the Al layer. Perhaps the most interesting point is that at the time of peak temperature the Li beam energy within the Al has fallen to below 3 MeV (or ~ 0.4 MeV/amu). This is near the peak in the stopping power curve — i.e., the region between the Bethe and Lindhard limits — as is evidenced by the maximum in the (dE/dx) curve (dash-dotted curve). Thus, the peak temperature in the Al should to some degree be sensitive to the physics near the peak in the stopping power curve (see Section 3 for more details on stopping power curves).

The effect of radiative heating of the Al by the Au is predicted in these simulations to be significantly smaller than direct heating by the Li beam. This is shown in Figs. 2.11 and 2.12. (We again point out, however, that the complex interaction of the Al lines with Au radiation may not be accurately simulated at this point.) Figure 2.11 shows the spatial distribution of heating in the target by the Li beam and by radiation at four simulation times. In addition to the radiative heating and cooling rates, the net radiative heating rate (heating minus cooling) is shown as well. (The discontinuities occur at the interfaces between the various target layers.) The Au ($r_{\text{init}} \approx 0.14 - 0.68 \mu\text{m}$) is heated at a rate of $\sim 70 - 80$ TW/g up to $t \sim 30$ ns, and then decreases as the beam intensity decays. Comparison with the net radiative heating in the Au shows that at $t \gtrsim 20$ ns the beam heating is nearly balanced by the radiative cooling. Because of this, the temperature of the Au does not increase at these times. Note also that absolute heating and cooling rates in the Au are quite large and nearly in balance because the Au is optically thick.

In the Al layer, the heating rate due to the Li beam is 200–300 TW/g. By comparison, the total radiative heating rate in the Al by the Au, except near $t \sim 20$ ns, is $\lesssim 100$ TW/g. At $t \lesssim 10$ ns, the heating rate is lower because the target temperature is relatively low. At late times the heating is also lower, presumably because the Al opacity is dropping due to it becoming more

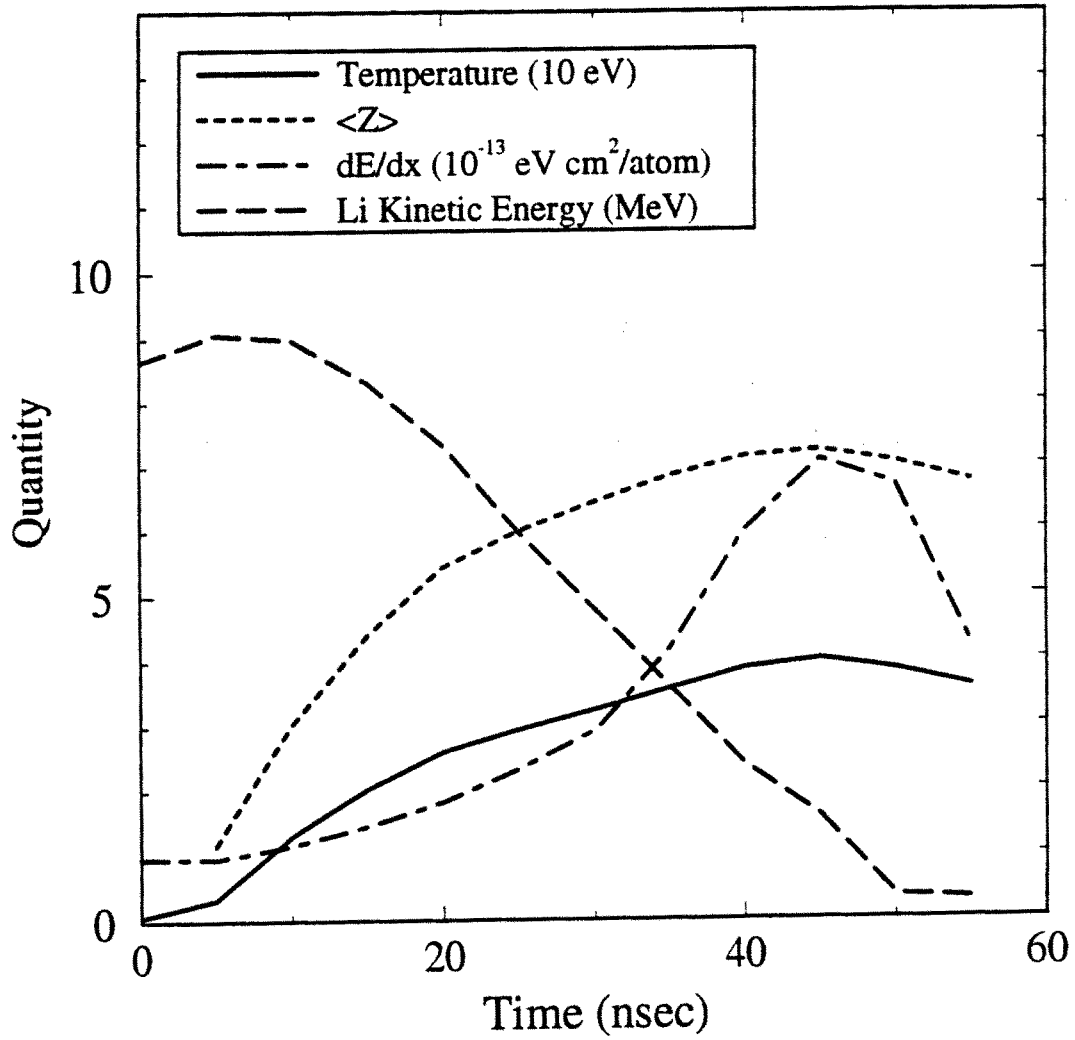


Figure 2.10. Time-dependence of the electron temperature, mean charge, stopping power, and Li beam voltage from baseline simulation of Shot 5851. All quantities are spatially averaged over the Al layer.

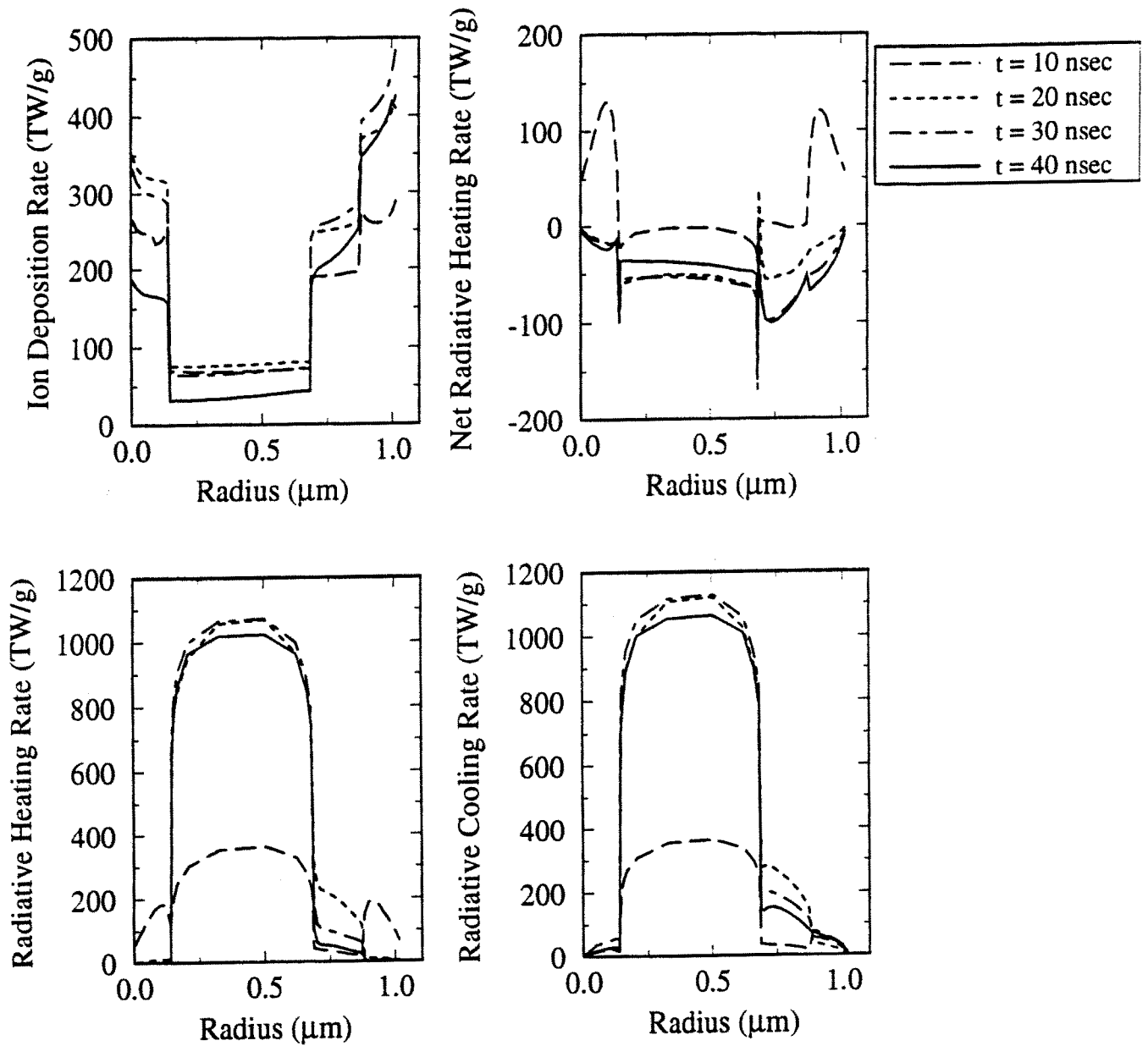


Figure 2.11. Spatial distribution of Li beam energy deposition, net radiative heating, and absolute radiative heating and cooling at times of 10, 20, 30, and 40 ns for Shot 5851 baseline simulation.

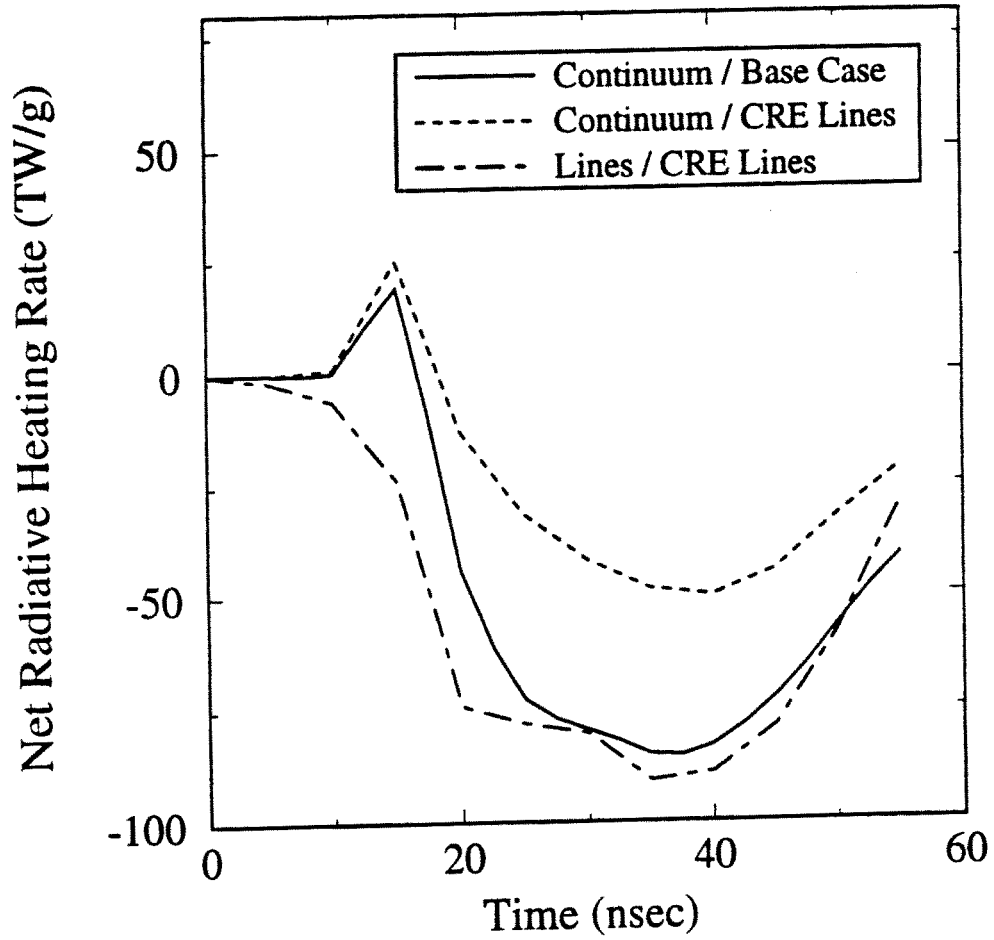


Figure 2.12. Net radiative heating rate in the Al layer as a function of time. In the base case (solid curve), only continuum radiation transport was considered. In the simulation which included line radiation transport for the low-Z layers, the contributions from the lines and continuum are shown separately.

ionized. Thus, it appears from these calculations that the heating of Al in these flat-foil experiments is mostly due to direct heating by the beam.

Figure 2.12 breaks down the contribution to the net radiative heating rate in the Al layer from lines and continuum. In the base case calculation (solid curve) line radiation effects of the low-Z materials were neglected. The results show that there is net heating in the Al continuum (most of the radiation likely originates in the Au) out to about 20 ns. At later times, there is net cooling as the Al temperature rises above the Au temperature. In the calculation with line transport effects included (“CRE lines”) the total net cooling — i.e., lines plus continuum — exceeds the “continuum only” base case by roughly 50% at times \gtrsim 20 ns. Because the total net cooling in the Al is larger in the CRE lines case, the peak temperature is lower (see Fig. 2.9).

It is also interesting to investigate the sensitivity of the predicted temperatures to various target and beam parameters. Figure 2.13 shows the time evolution of the mean temperature in each of the target layers from four different radiation-hydrodynamics simulations. In each case, the calculations are identical to the “base case” calculation with the exception of a single parameter. The plots on the upper half of Fig. 2.13 show results from calculations in which the stopping power (left) and Li beam current density (right) were enhanced by 10%. The higher (dE/dx) lead to an increase in the peak temperature of the Al of 14% (45.4 eV vs. 40.0 eV), while enhancing the beam current density increased the Al temperature by 9%. Enhancing the (dE/dx) has a somewhat larger effect because it results in a lower beam voltage in the Al after it passes through the Au.

The lower portion of Fig. 2.13 shows the effect of changing the target layer thicknesses. When a thickness of the Au is decreased from 5400 Å to 3000 Å, the peak temperature in the Al decreased to 34.4 eV (14% lower than the base case). This is due to the fact that the Al sees a higher beam voltage when the Au is thinner, and thus has a lower stopping power. When a thicker Al layer is used (7000 Å vs. 1800 Å) the maximum temperature predicted for the Al is slightly lower (37.6 eV vs. 40.0 eV). This appears to be due to the Li beam ranging out in the thicker Al at late times.

We now compare the predictions for several PBFA-II shots in which Al K_α satellite spectra were recorded from flat-foil targets. Figure 2.14 shows the time-dependent mean temperature in each target layer for Shots 5851, 5846, and 6347 using the beam parameters shown in Fig. 2.4. The K_α spectra observed for these shots were qualitatively similar [2], suggesting the temperatures attained in the Al layers were roughly the same. The peak temperatures in the Al from simulations of Shots 5851 and 5846 are 40 and 41 eV. On the other hand, the peak temperature predicted for Shot 6347 was only 31 eV. This is clearly the result of the lower beam intensities used in this calculation (see Fig. 2.4).

The lower temperature predicted for Shot 6347 is somewhat puzzling at this time since its K_α satellite spectrum is similar to that of Shots 5851 and 5846 [2]. One possible explanation is the

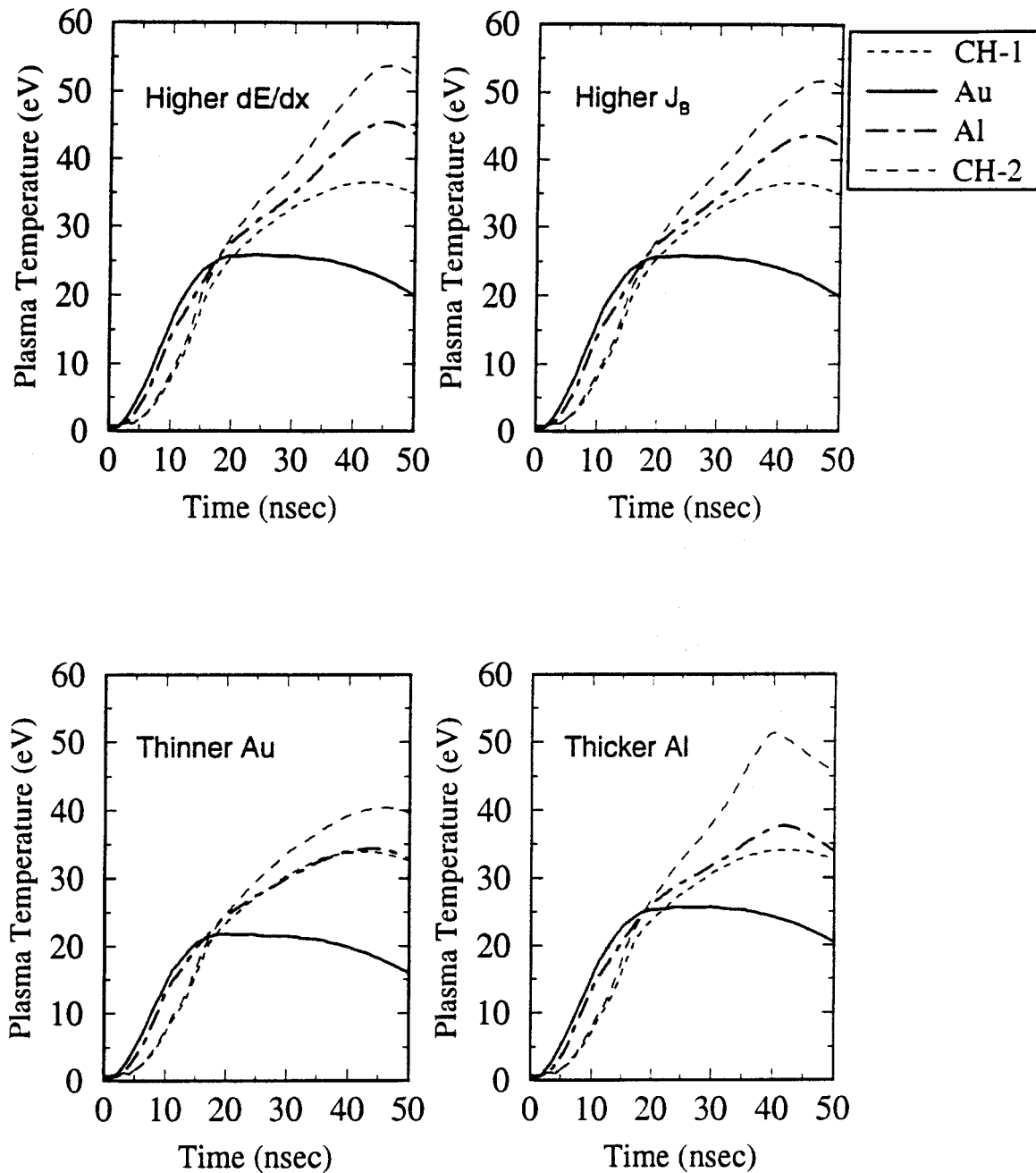


Figure 2.13. Time-dependence of mean temperature in each target layer from 4 different radiation-hydrodynamics simulations. Comparison with our Shot 5851 baseline case shows the sensitivity of the temperatures to the stopping power (upper left), the Li beam current density (upper right), and the thicknesses of the Au and Al layers. See text for calculation details.

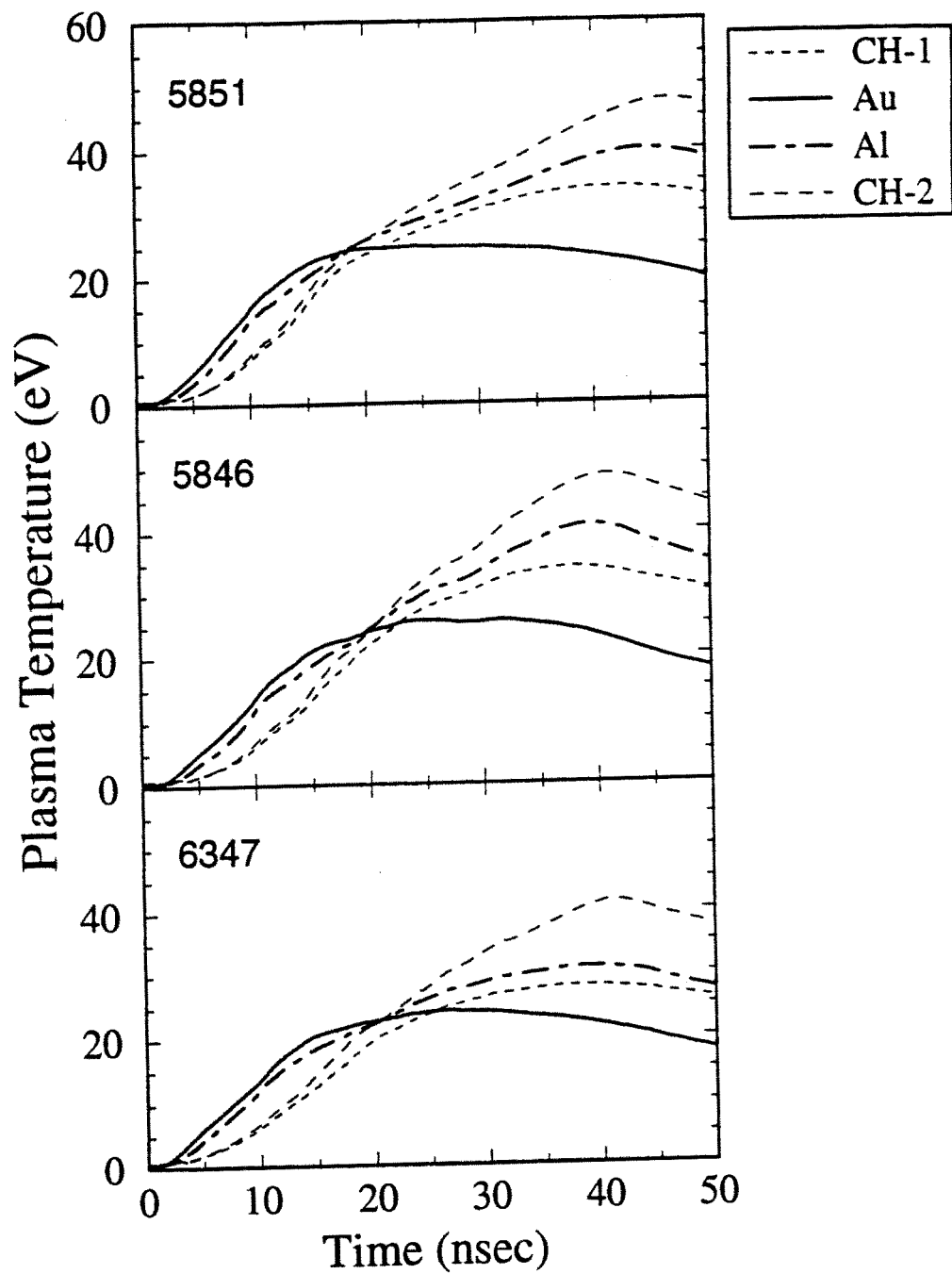


Figure 2.14. Time-dependence of mean temperatures in each target layer from simulations of PBFA-II Shots 5851, 5846, and 6347.

true Li beam intensity for Shot 6347 was higher than that used in the simulation, or its pulse width was significantly longer. It is hard to explain this apparent inconsistency between the K_α spectrum and beam diagnostics for Shot 6347 on the physics models in the radiation-hydrodynamics and/or CRE codes because one would expect similar inconsistencies to show up in Shots 5851 and 5846. On the other hand, the radiation-hydrodynamics simulations for Shots 5851 and 5846 appear to predict temperatures which are more consistent with their K_α satellite spectra.

This suggests that to “first order” a good understanding of the basic physics exists of how the target is heated and how the K_α satellite spectrum is formed. The radiation-hydrodynamics calculations have also been used to identify which physical processes most influence the target temperatures attained in the flat-foil PBFA-II experiments. We find for these types of experiments that it is desirable to be able to accurately diagnose the beam characteristics at relatively late times in the pulse, which is when the peak temperatures in the Al are achieved. In regards to modeling, two areas which play a key role in these experiments are stopping power physics and radiation transport. In particular, the interaction between the Au radiation and low-Z line opacities is not particularly well-understood at this time. Theoretical stopping power work which could potentially lead to a more accurate picture of fast ions stopping in hot plasmas is discussed in Section 3.

2.3. Comparison of Experimental and Simulated K_α Satellite Spectra

In this section, we present results from CRE/atomic physics calculations of K_α satellite emission spectra based on the radiation-hydrodynamics target plasma conditions and Li beam parameters described in Section 2.2. To make a direct comparison with measured time-integrated K_α spectra, we produce “synthetic” time-integrated spectra using the following procedure. The spatial distribution of temperatures, densities, and Li beam current densities and kinetic energies in the Al layer of the target are output at selected times (every 2.5 ns) in the radiation-hydrodynamics calculations. This data is then used as input for our CRE calculations to compute the K_α satellite spectrum at each simulation time. The calculated spectra are then time-integrated, and convolved with a Gaussian with a FWHM of 1.5 eV, which corresponds to an instrumental resolution of $\lambda/\Delta\lambda \approx 1000$.

Details of the atomic physics and collisional-radiative models have been described in detail elsewhere [4–6]. The major features of these codes are summarized in Tables 2.1 and 2.2.

We now describe results based on 3 radiation-hydrodynamics simulations. The first is our baseline calculation for Shot 5851, which predicted a peak mean temperature in the Al layer of 40 eV. The second is the simulation of Shot 6347, in which the peak Al temperature was calculated to be only 31 eV. The third is from the simulation of Shot 5851 in which radiation losses were neglected, and the maximum Al temperature was 56 eV. This set of calculations therefore provides insights on how the Al K_α spectrum changes for temperature differences of $\sim 30\%$.

Table 2.1. Major Features of Collisional-Radiative Equilibrium Code

- Multilevel, steady-state atomic rate equations are solved self-consistently with the radiation field and ion beam properties.
- Any state in the atomic model can be coupled to any other state; thus, transitions between excited states of differing ions can be considered, as can transitions between non-adjacent ions.
- Ion beam-induced multiple ionization effects are included as direct transitions in the statistical equilibrium matrix equations.
- Emission and absorption spectra include contributions from bound-bound (lines), bound-free (recombinations), and free-free transitions (Bremsstrahlung).
- Inner-shell line emission induced by intense ion beams is calculated by tracking the populating and depopulating rates of autoionizing levels which are explicitly included in the model.
- Line shapes include effects of natural, Doppler, Auger, and Stark broadening.
- Radiation transport is modeled using either:
 - (i) an angle- and frequency-averaged escape probability method, or
 - (ii) a multiangle, multifrequency model based on the second-order form of the transfer equation.

Table 2.2. Major Features of Atomic Physics Models

- Atomic structure and radiative data are computed using configuration interaction (CI) method with Hartree-Fock wavefunctions.
- Multiconfiguration Hartree-Fock and Dirac-Fock calculations provide accurate transition energies and oscillator strengths for lines of interest.
- Atomic collisional data are computed using a combination of distorted wave, Coulomb-Born, and semiclassical impact parameter models.
- Ion-impact ionization cross sections are computed using a plane-wave Born approximation model with Hartree-Fock wavefunctions and with the inclusion of binding energy, Coulomb-deflection, and relativistic corrections.
- Multiple ionization cross sections are computed using an independent event model with a binomial distribution probability.
- Term-dependent Auger rates and fluorescence yields are calculated using an LS coupling formalism with Hartree-Fock wavefunctions.

Figure 2.15 compares the experimental and calculated time-integrated K_α satellite spectra from Shot 5851 (baseline case). Calculated spectra (bottom) are shown for integration times up to 10, 20, 30, and 55 ns, thus showing the buildup in the spectrum with time. The results show that the bulk of the emission from the F-like (cold) and O-like satellites comes from times $\lesssim 10$ ns, and N-like and C-like at times $\lesssim 20$ ns. Roughly half of the B-like emission occurs between 10 and 20 ns. Thus, the satellites with the strongest intensity in the experimental spectrum (O-like through B-like) likely emit the majority of their photons during the peak of the Li beam intensity ($t \sim 10 - 20$ ns; see Fig. 2.4). Most of the emission from the Be-like through He-like satellites is predicted to occur at $t \lesssim 35$ ns (see Fig. 2.15), which is somewhat earlier than the time at which the maximum Al temperature is attained in the simulations. Little emission occurs at later times for two reasons: (1) the beam current density is decreasing, and (2) the beam-impact ionization cross section is decreasing because of the lower Li beam kinetic energy in the Al. Between 20 ns and 35 ns the current density drops by roughly 50% and the beam voltage in the Al drops from about 7.3 MeV to 3.6 MeV (see Fig. 2.10). The latter leads to a decrease in the beam-impact ionization cross section by about a factor of 5, as is shown in Fig. 2.16. Thus, the total rate of K-shell ionizations ($R \sim J_B \cdot \sigma_K(E_B)$) drops by about one order of magnitude between 20 and 35 ns. It therefore appears likely, based on the above simulations, that there is little contribution to the K_α spectrum after $t \sim 35$ ns. This would suggest that the peak temperatures that occurred in the Al were not “recorded” in the measured spectrum.

Figure 2.17 shows the calculated K_α spectra at 5 ns intervals for the Shot 5851 baseline case. For clarity, the He $_\alpha$ through Be-like Al spectral region is enhanced on the right side of the figure. Note the clear dropoff in K_α line intensities at later times due to the lower Li beam kinetic energies in the Al.

Figure 2.18 compares synthetic time-integrated spectra for the Shot 5851 baseline case, Shot 5851 with no radiation losses, and Shot 6347. Again, the He $_\alpha$ to Be-like spectral region is enhanced for clarity (on the right). For the 5851 baseline case, and Li-like satellite fluxes are predicted to originate between 15 ns and 35 ns in the simulation, suggesting the K_α spectrum for these lines forms over a fairly long period of beam pulse. It is also seen that for the 5851 baseline case that the intensities of these higher ionization stage satellites are significantly lower than the experimental values. For instance, the He/Li ratio — i.e., the He $_\alpha$ intensity divided by the Li-like satellite intensities (integrated from 7.780 Å to 7.885 Å) — is 0.053. By comparison, the experimental value is 0.28. Similarly, the calculated Li/Be ratio is 0.24, while the experimental value is 0.58. (Note that roughly half of the intensity quoted for the experimental He value is due to a second feature located 17 mÅ to the long-wavelength side of the He $_\alpha$ [2]; this suggests the observed He $_\alpha$ /Li ratio is $\sim .14$).

The situation for Shot 6347 is substantially worse because of the lower predicted temperatures in the Al. Very little intensity from the He $_\alpha$ and Li-like satellites is predicted in

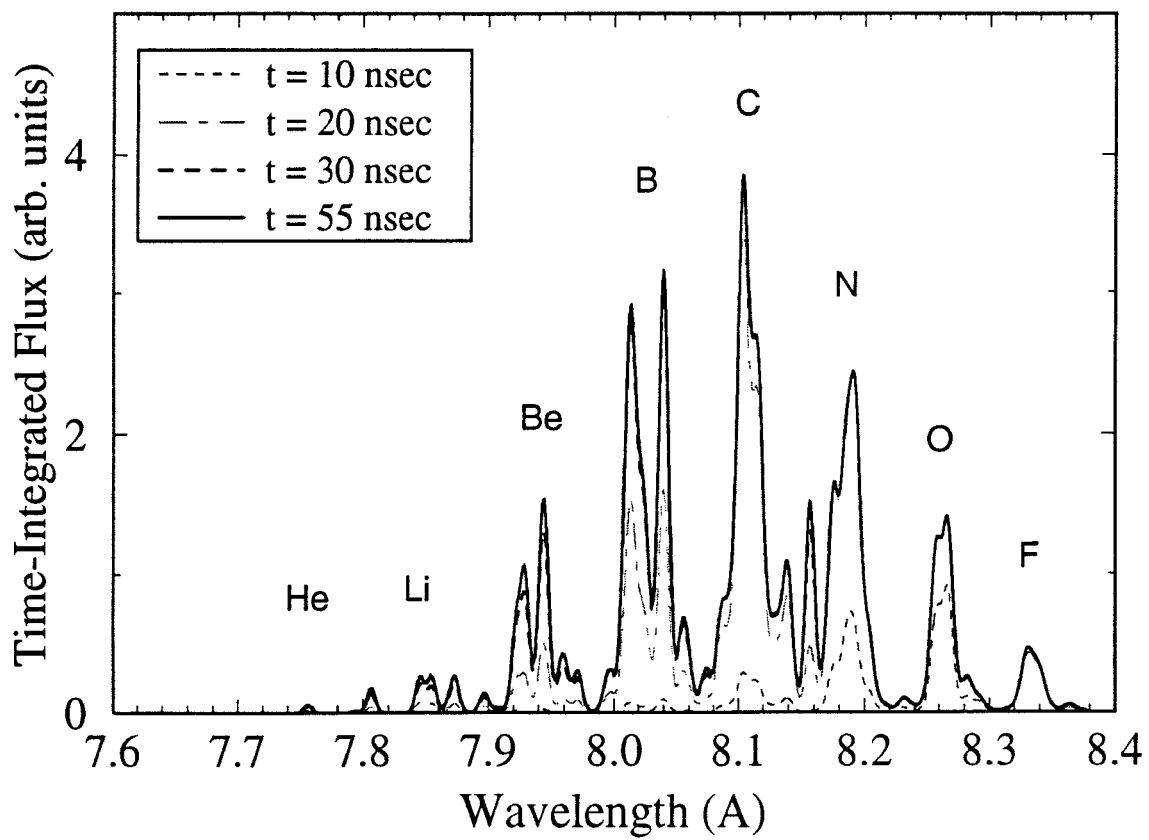
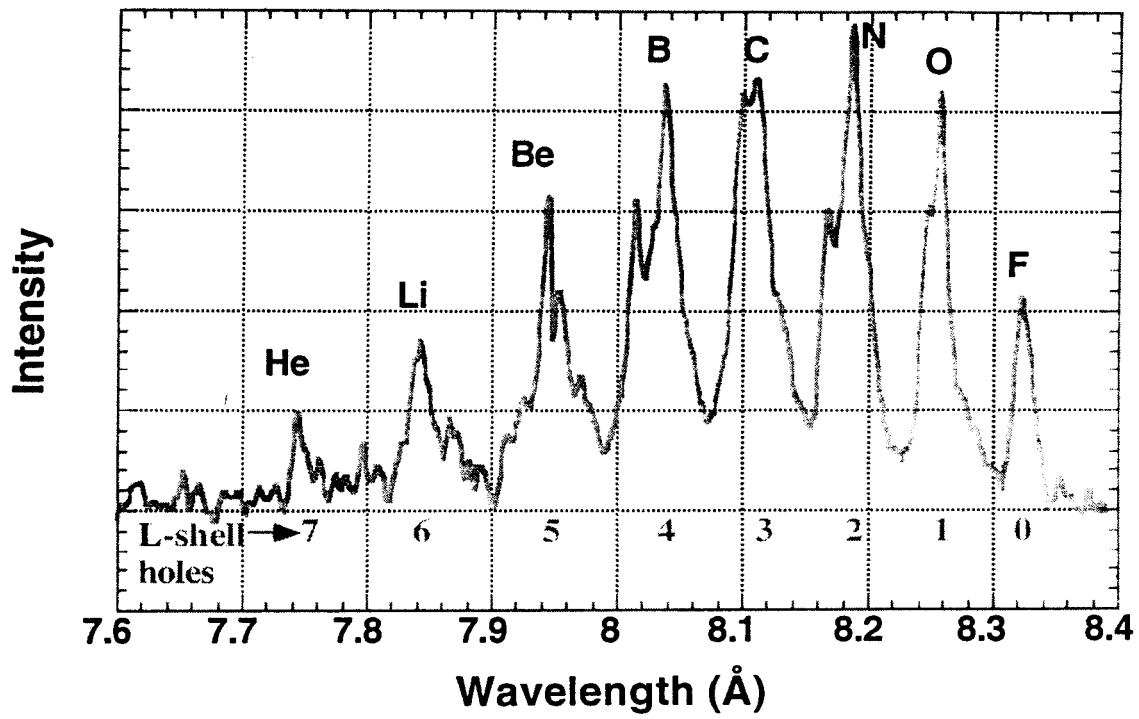


Figure 2.15. Comparison of time-integrated experimental and simulated Al K α satellite spectra for Shot 5851.

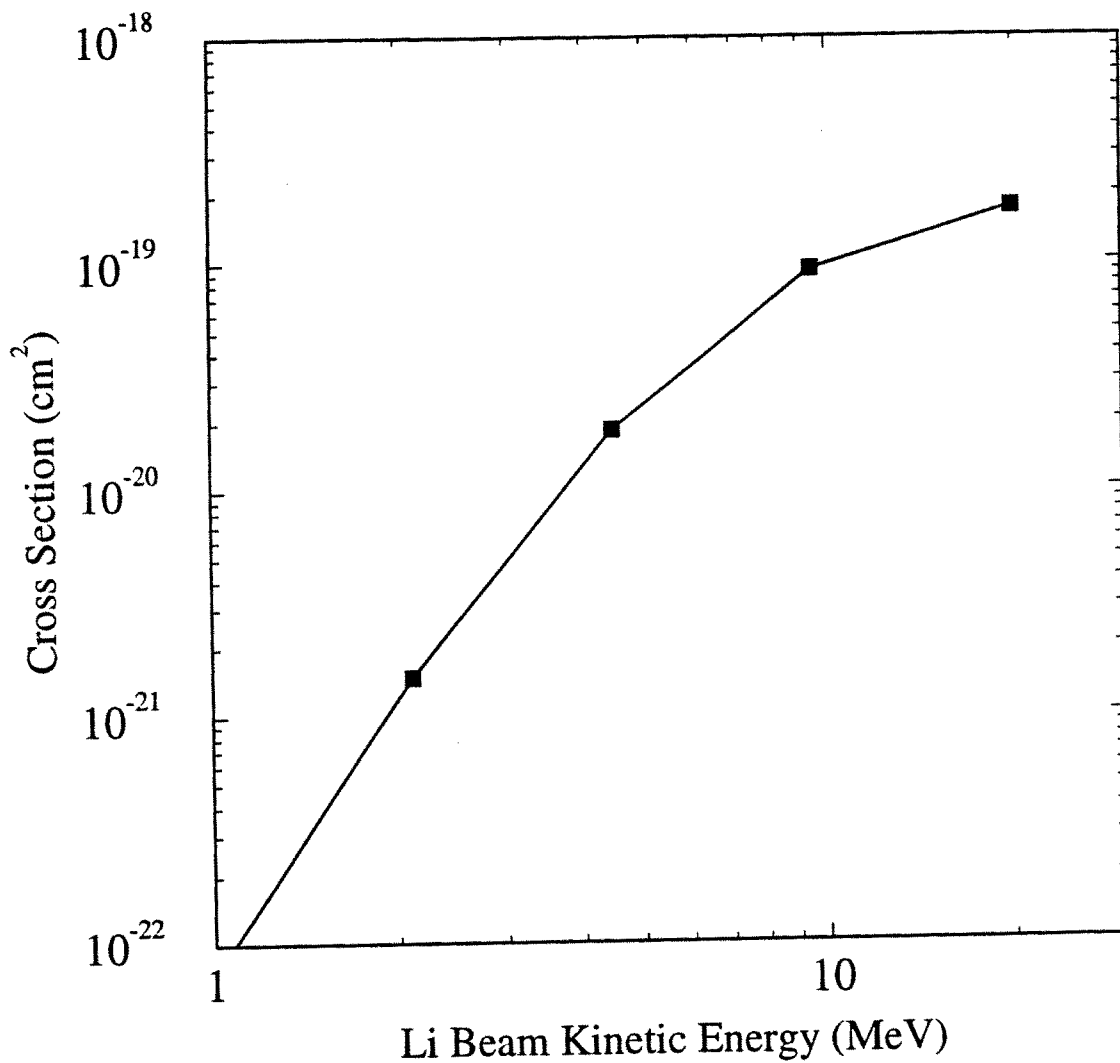


Figure 2.16. Li-impact ionization cross-section for K-shell of Be-like Al: $1s^2 2s^1 2p^1 \rightarrow 1s^1 2s^1 2p^1$.

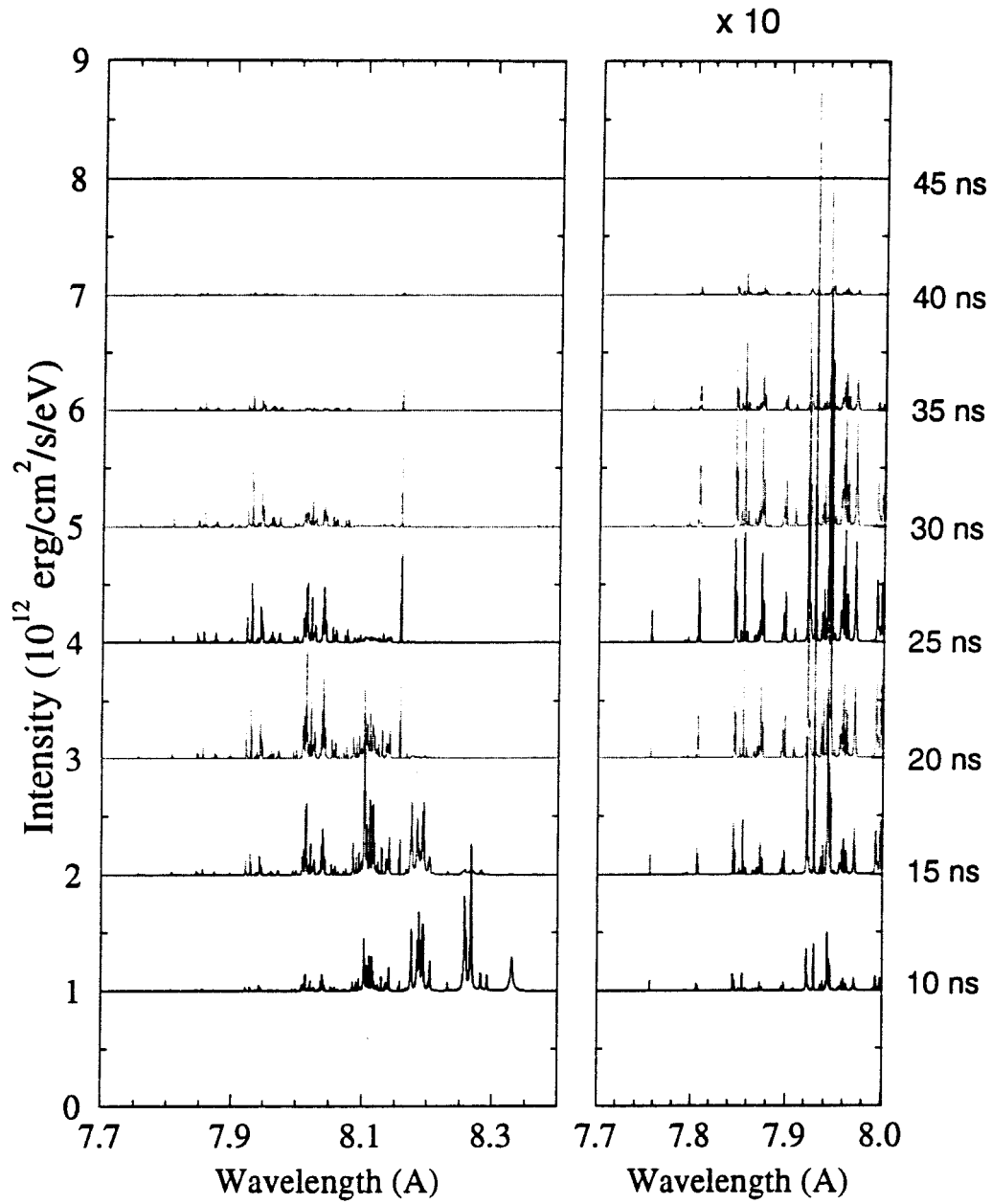


Figure 2.17. Calculated K_α satellite spectra for Shot 5851 baseline case at 5 ns intervals.

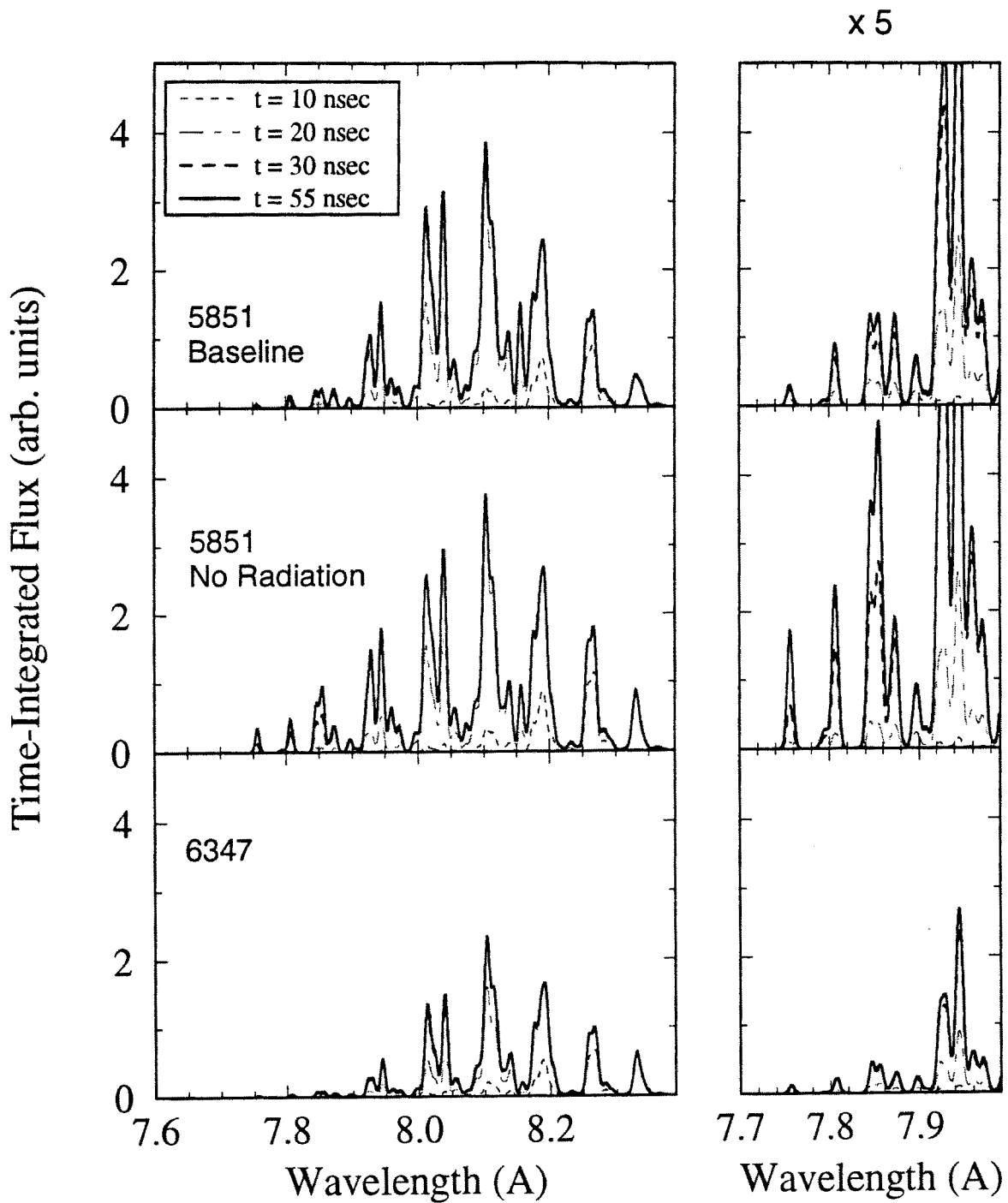


Figure 2.18. Time-integrated Al K_{α} spectra from 3 simulations. Top: Shot 5851 baseline simulation; middle: Shot 5851 with no radiation losses; bottom: Shot 6347. The curves on the right show the intensities in the He α through Be-like region, magnified by a factor of 5 for clarity.

the simulations. On the other hand, in the simulation of 5851 which neglected radiation losses, significantly more radiation from the He_α line and Li-like satellites is predicted. In this case, the calculated He/Li ratio is 0.12, while the Li/Be ratio is 0.40, which is in substantially better agreement with the experimental spectrum.

In summary, it appears the target temperatures predicted from the radiation-hydrodynamics simulations using measured Li beam parameters from Shots 5851 and 5846 are somewhat low compared to those inferred from their K_α satellite spectra. This is indicated by the fact that the calculated intensities of the He_α and Li-like satellites are weaker than the observed values. For Shot 6347, the calculated temperatures in the Al region of the target are even lower, thereby producing an even larger discrepancy with the measured K_α spectrum.

There are several possible explanations for the calculated temperatures being too low. First, the Li beam parameters used in the simulations may be inaccurate. This in some sense is supported by the fact the beam parameters inferred for Shots 5851 and 6347 are very different — with the beam intensity for 6347 being $\sim 50\%$ lower — while their K_α spectra are qualitatively similar. Also, the beam parameters inferred using different diagnostics for the same shot can vary significantly. Calculations performed for Shot 5851 using Li beam current densities which are $\sim 25\%$ greater than those inferred from the data produce significantly better agreement with the K_α spectrum.

A second possible source of error is the stopping power model for Li ions in Au and Al. If the model underpredicted the Au stopping power, the beam voltage in the Al layer would be too high. This has two competing consequences: (1) the Al stopping power would be too low, resulting in a lower temperature for the Al; and (2) the beam-impact ionization cross sections would be too high, resulting in an enhancement of the K_α satellite line intensities for the ions present at that particular time. In future calculations, we will attempt to utilize stopping powers from the model described in Section 3.

A third possible explanation is the interaction of the radiation emitted from the Au layer and the Al. In the radiation-hydrodynamics simulations, the heating at photon energies where Al lines dominate the opacity was not considered. Thus, the radiative heating of the Al by the Au may have been underestimated. It is also worth noting that the effects of the Au radiation have also not been included in the CRE K_α spectral calculations for the Al. These effects could be considered in more detail with relatively minor changes in our models. It would also be useful to design experiments to isolate the effects of some of the physical processes described above.

Fourth, if significant contaminants (non-Li ions) were present in the beam, particularly at relatively late times ($t \gtrsim 20$ ns) when the He_α and Li-like Al satellites are formed, this could produce an anomalous source of heating, and perhaps also an anomalous source of ion-impact ionizations which might have influenced the K_α satellite spectra.

It is also worth noting the rather long times over which the He_α and Li-like lines are built up in the simulations (see Figs. 2.15 and 2.17). In previous work [20] we described how K_α line intensity ratios could be used to deduce target plasma conditions. We feel this is a particularly powerful diagnostic technique for intense light ion beam experiments in which *time-resolved* spectra can be obtained. However, because the times over which the K_α emission lines form can be fairly long, one must be somewhat cautious when applying this technique to time-integrated spectra.

To conclude, we feel a reasonably good overall understanding of these PBFA-II flat-foil experiments has been achieved. Although several discrepancies appear to remain in the analysis of these experiments, it is felt that considerable progress has been made in developing a better understanding of some of the key physics issues for light ion fusion that were mentioned in the introduction and which motivated these experiments [2]. We have examined the sensitivity of predicted results to various physical effects, target parameters, and diagnostic uncertainties. This analysis has also led to an improved understanding of the atomic processes affecting the formation of K_α satellite spectra in intense Li beam experiments, which could prove to be a very useful technique for diagnosing target plasma conditions in future light ion fusion experiments.

2.4. Simulation of Higher Intensity Li Beams

In this section, we present results from simulations for relatively high intensity Li beams. The purpose is to provide predictions for what can be expected in future PBFA-II or PBFA-X experiments. These simulations were done in a very simple manner. The model parameters and assumptions were the same as in the “base case” calculation of Shot 5851 (see Section 2.2), except that the current density was multiplied by a constant.

Figure 2.19 shows the time-dependent mean temperatures in each of the target layers. The top plot corresponds to the Shot 5851 base case (reproduced here for convenience). The middle and bottom plots show results from calculations in which the Li beam current density was enhanced by a factor of 2 and 3, respectively. Note that the temperature of the Au remains relatively low ($T \lesssim 40$ eV) throughout the beam pulse. This again is due to the fact that the Au is optically thick and a very efficient radiator. The Al, on the other hand, is able to attain a much higher temperature, scaling roughly linearly with the beam current density. Thus, our calculations suggest that by enhancing the current density by a factor of about 2.5 over that of Shot 5851 that one could obtain an electron temperature in the Al of ~ 100 eV. In experiments of this type, one would of course also want to choose a somewhat higher-Z tracer than Al to provide spectral diagnostic information.

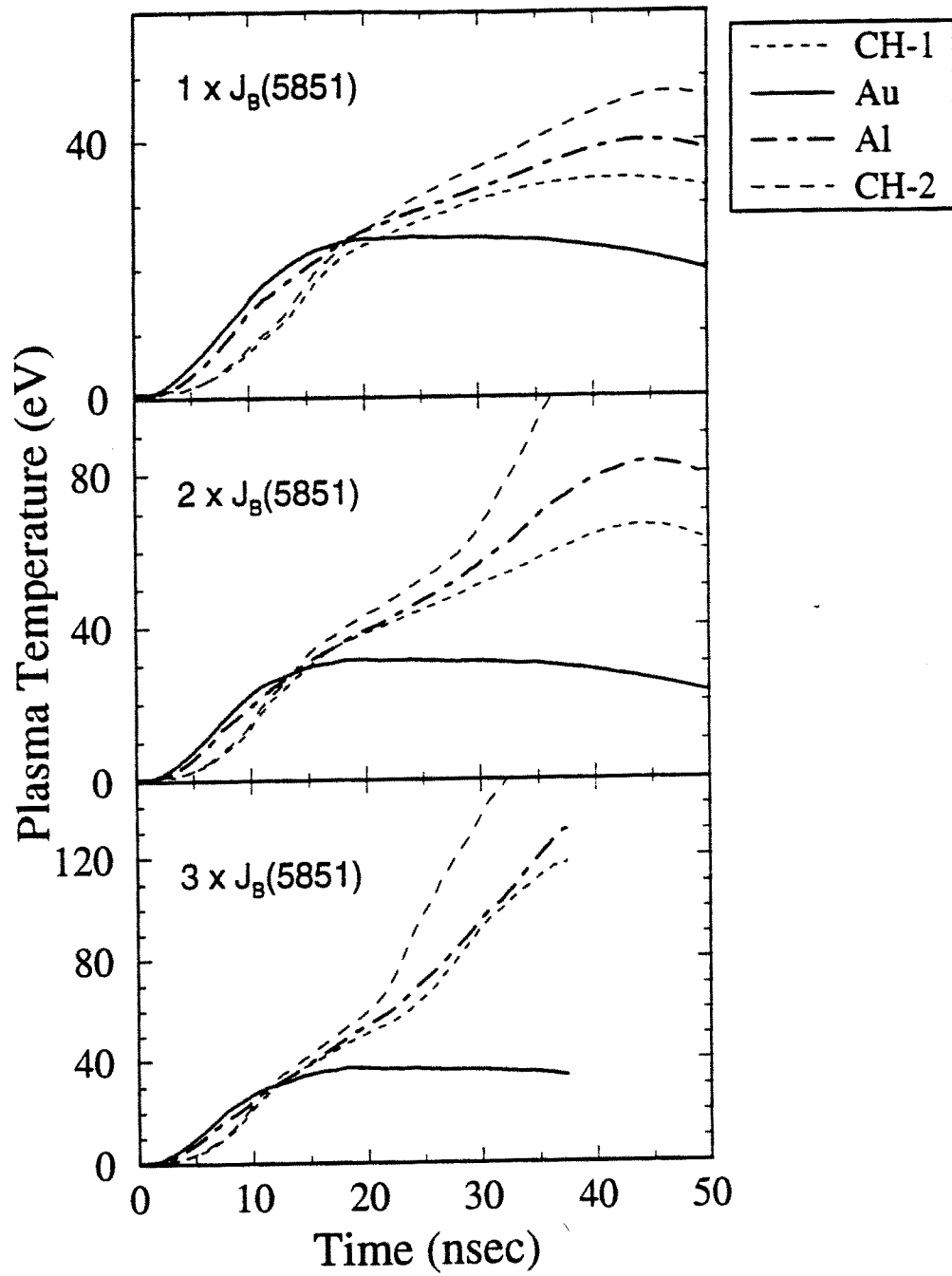


Figure 2.19. Time-dependent mean temperatures in each target layer from simulations in which Shot 5851 Li beam current densities were multiplied by factor of 1 (top), 2 (middle), and 3 (bottom).

3. An Unified Self-Consistent Field Model for Ion Energy Deposition in Ion-Driven Inertial Confinement Fusion Targets

3.1. Introduction

For many years, the stopping of energetic ions in matter has been a subject of great interest to theoretical and experimental physicists. In the context of ion driven-inertial confinement fusion (ICF) experiments, the stopping power of ions in matter in both solid and plasma states is crucial for target design. For a reliable diagnostic evaluation of ion beam and target parameters — such as beam intensity, temperature, and density — one must know the stopping power accurately. Several comprehensive reviews of calculations and measurements of ion stopping power in ICF targets have been given by Mehlhorn [21,22], Deutsch [23], and Peter [24].

For typical plasma conditions in ion beam-target interaction experiments, the target plasmas are often partially ionized. Both bound and free electrons can therefore contribute to the stopping power. A commonly used approach for calculating ion stopping powers in partially ionized plasmas is to treat the stopping electrons as two components: those bound to the plasma ions and those which constitute the plasma free electrons. The number of free electrons in the plasma is determined by solving the Saha equation. The contribution of each group of electrons to the stopping power is calculated separately. For example, many stopping power calculations [21,25] use the Bethe equation [26] for the bound electrons and use a separate term for the plasma free electrons. A weakness of this approach is that the “bound” and “free” electrons are not treated self-consistently. If we represent the effect of the plasma by a fluctuating microfield, the perturbations of it can cause an orbital electron to have some nonzero probability of becoming unbound from its original nucleus. However, an electron which is unbound in a one-center system may still be bound in a two-center system consisting of the original nucleus and a neighboring ion. Moreover, the electron may also be bound in a 3,4,..., center system which includes additional neighboring ions. A relevant discussion of these quasi-free electrons has been given by More [27], who makes use of the formal collision theory to describe these electrons within the framework of the ion sphere atomic model. Since the characteristic interaction velocities of “bound” and “free“ electrons are different in ion stopping, the “quasi-bound” electrons play the role of bridging them. The effects of “quasi-bound” electrons on stopping power have not been studied in detail before. Another drawback of the combined stopping power model is that it uses different models for different energy regimes, and the separation boundary of “low” and “high” energy regimes is somewhat ambiguous.

In 1963 the first unified approach to ion stopping and range theory was made by Lindhard, Scharff, and Schiott [28] and their approach is commonly called the LSS-model. This work brought together Lindhard’s elegant dielectric formulation of stopping theory and local density approximation, and bridging approximations were made so that calculations of stopping power of cold material could, for the first time, be made within a single model. However, since the LSS-model is based on Thomas-Fermi statistical atoms, it naturally shows no shell effects and is only accurate

for atoms with many electrons in the intermediate range where they are neither fully stripped nor almost neutral. With the LSS-model it is possible to predict the ion stopping power of solids within a factor of 2. Later on, significant improvement [29] has been made with the incorporation of more realistic Hartree-Fock atoms into the LSS-model. Now, a natural question should be asked is how should we extend the LSS-model to form a single unified model that is capable of accurately predicting the ion range and energy deposition profile as a function of material composition, density, temperature, and degree of material ionization for a variety of different ionic species and beam energies.

In this work we develop a unified self-consistent-field model for ion energy deposition in ion-driven inertial confinement fusion targets. As a starting point, we noticed while looking through many calculations of cold material stopping power in the framework of the LSS-model that the overall accuracy is much better when the solid state Hartree-Fock electron density distribution is used instead of an isolated Hartree-Fock atomic model. On the other hand, Lindhard's stopping power formalism needed to be extended to included finite temperature effects. Hence the present work is concerned with establishing two main points.

The first main point is how to choose an atomic model which is appropriate for the conditions relevant to the ion-driven inertial confinement fusion targets. The requirement for the model is that it should recover the electron density distributions of both solid-state and isolated atom Hartree-Fock models in the corresponding conditions. In 1979 Liberman [30] developed a self-consistent-field “muffin-tin” atomic model for high density plasmas. This model has much of the simplicity of an isolated atom but captures much of the physics of the band-structure model. It provides a self-consistent treatment for both “bound” and “free” electrons in a wide range of plasma conditions. We will use this atomic model to determine the electron density distribution function. Since we are interested in both low- Z and high- Z materials, the relativistic formulation is used. The second main point of this work concerns the stopping characteristics of the ICF-relevant hot plasmas with an electron temperature comparable or smaller than the Fermi temperature. In this respect, we take advantage of the full Random Phase Approximation (RPA) dielectric function developed by Maynard and Deutsch [31].

In Section 3.2 we review the Lindhard stopping power formalism and the local density approximation which form the framework of this study. In Section 3.3 we describe the muffin-tin atomic model used to compute the electron distributions of the target atoms. In Section 3.4 we discuss the full RPA stopping interaction function. Numerical results and discussions are presented in Section 3.5. A summary of this investigation is given in Section 3.6.

3.2. Lindhard's Formalism of Stopping Power and Local Density Approximation

For an ion of charge Ze moving with velocity V in a medium of uniform density ρ , the energy loss due to electron excitation can be conveniently written in the form

$$-\frac{dE}{dx} = \frac{4\pi}{m} \left(\frac{Ze^2}{V} \right) \rho L(\rho, V), \quad (3.1)$$

where L is the stopping number and m is the mass of electron. In the dielectric formalism, L is written as

$$L = \frac{i}{\pi\omega_0^2} \int_0^\infty \frac{dk}{k} \int_{-kV}^{kV} \omega d\omega [\varepsilon^{-1}(k, \omega) - 1], \quad (3.2)$$

where ω_0 is the plasma frequency; i.e.,

$$\omega_0^2 = \frac{4\pi e^2 \rho}{m}, \quad (3.3)$$

and $\varepsilon(k, \omega)$ is the wave number- and frequency-dependent longitudinal dielectric constant.

Lindhard's formalism for the interaction of a charged particle with a free electron gas makes the following assumptions:

- The free electron gas consists of electrons at zero temperature (single electrons are described by plane waves) on a fixed uniform positive background with overall charge neutrality.
- The initial electron gas is of constant density.
- The interaction of the charged particle is a perturbation on the electron gas.
- All particles are non-relativistic.

With these assumptions, Lindhard obtained the stopping number, L , as

$$L = \frac{6}{\pi} \int_0^{V/V_F} u du \int_0^\infty dz \frac{z^3 f_2(u, z)}{[z^2 + \chi^2 f_1(u, z)]^2 + [\chi^2 f_2(u, z)]^2}, \quad (3.4)$$

where

$$f_1(u, z) = \frac{1}{2} + \frac{1}{8z} [1 - (z - u)^2] \left| \ln \frac{z - u + 1}{z - u - 1} \right| + \frac{1}{8z} [1 - (z + u)^2] \left| \ln \frac{z + u + 1}{z + u - 1} \right| \quad (3.5)$$

and

$$f_2(u, z) = \begin{cases} \frac{1}{2}\pi u & \text{for } z + u < 1 \\ (\frac{\pi}{8z})[1 - (z - u)^2] & \text{for } |z - u| < 1 < z + u \\ 0 & \text{for } |z - u| > 1. \end{cases} \quad (3.6)$$

The quantities z and u are the reduced wave number and frequency:

$$z = \frac{k}{2k_F} \quad \text{and} \quad u = \frac{\omega}{kV_F} \quad (3.7)$$

with k_F and V_F denoting Fermi wave number and velocity which are related to Fermi energy as

$$E_F = \frac{1}{2} mV_F^2 \equiv \frac{\hbar^2 k_F^2}{2m} = \frac{\hbar^2}{2m} (3\pi^2 \rho)^{2/3}. \quad (3.8)$$

The dimensionless quantity χ^2 is defined by

$$\chi^2 = \frac{V_0}{\pi V_F}, \quad (3.9)$$

with $V_0 = e^2/\hbar$ denoting the Bohr velocity. Some typical curves illustrating the variation in the Lindhard stopping number with electron density and energy are shown in Fig. 3.1.

The Lindhard stopping power formalism is a many-body self-consistent treatment of an electron gas responding to a perturbation by a charged particle. It naturally includes the polarization of the electrons by the charged particle, the resultant charge-screening, and the plasma density fluctuations. It treats smoothly both individual electron excitation and collective plasmon excitations without separate “distant” and “close” collision processes. However, Eq. (3.1) is strictly valid only for a uniform free electron gas. For a partially ionized plasma, the electron density distribution is no longer uniform because of the presence of bound electrons. In such cases, the Lindhard stopping power formalism can still be directly applied with the use of the local-density approximation [32].

In the local-density approximation, the nonuniform electron cloud is divided into small independent volume elements, and the electron density distribution in each volume element is assumed to be uniform. The stopping power is calculated for a charged particle in a free electron gas of each volume element’s density, and the final stopping power is computed by averaging over these values, weighted by their distribution in the nonuniform electron cloud; i.e.,

$$\left(-\frac{dE}{dx}\right) = \frac{4\pi}{m} \left(\frac{Ze^2}{V}\right)^2 \int_0^\infty \rho(r) L(\rho, V) 4\pi r^2 dr, \quad (3.10)$$

where $\rho(r)$ is the spherically-averaged electron density of the target atom.

It can be seen from Eq. (3.10) that the electronic stopping of an ion in a plasma is determined by two key functions, the electron density distribution function $\rho(r)$ and stopping number $L(\rho, V)$.

3.3. Atomic Model And Electron Density Distribution Function

The electron density distribution of an atom is affected by its surrounding environment. This is particularly true for the outer-shell electrons. Figure 3.2 illustrates the difference between

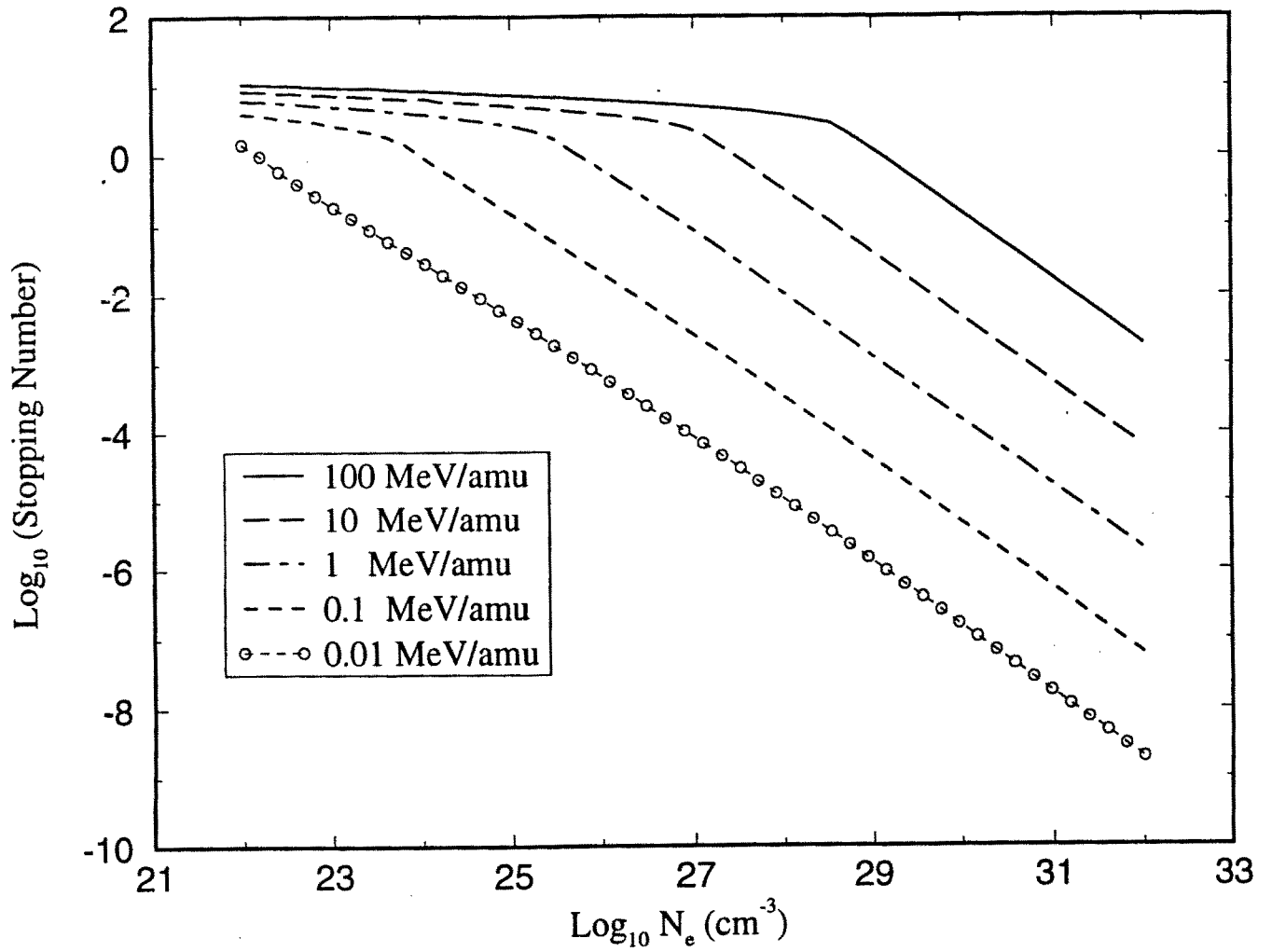


Figure 3.1. Variation in Lindard stopping number with electron density for select projectile energies.

the calculated electron distribution for an isolated atom (denoted HFS for Hartree-Fock-Slater) and that of the same atom in a solid-state lattice [33]. It can be seen that there is a pronounced difference in the spatial variation of the solid-state and isolated atomic electron densities away from the interior of the target atom due to solid-state bonding effects. It was found [34] that this spatial variation in electron density gives rise to a marked change in density-averaged stopping number. Therefore, it is necessary to use solid-state electron densities in the calculation of stopping power of solids.

What should be the appropriate electron density distribution function in stopping power calculations for a plasma atom? To date, the isolated atom model has been most commonly used in calculations of ion stopping powers for plasmas. However, just as for solids, its applicability to hot dense ICF plasmas is questionable [22] because of the marked perturbation of surrounding environment. In order to account for environmental effects on the electron distribution properly, we choose a self-consistent-field “muffin-tin” atomic model [30] in our stopping power calculations. One important feature of this model is that it smoothly connects the solid-state self-consistent-field atomic model and the isolated atom Hartree-Fock model. It naturally extends the solid-state Hartree-Fock model into finite temperature, high-density plasmas. On the other hand, in the low density regime it correctly describes an isolated atom or an ion in equilibrium with an electron gas. Therefore, plasmas over a wide range of temperatures and densities can be treated with this atomic model.

Figure 3.3 illustrates several aspects about the charge distribution for this model [30]. At the center of a spherical cavity is a point nucleus, outside the cavity there is a uniform distribution of positive charge which takes the place of the surrounding ions. There are sufficient electrons in the system to give overall electrical neutrality, and the additional requirement of electrical neutrality inside the sphere is imposed. A muffin-tin approximation is used for the electron density outside the sphere. The electrons are governed by a set of self-consistent-field one-electron Dirac equations:

$$[c\vec{\alpha} \cdot \vec{p} + \beta c^2 - c^2 + V(r)] \phi_i(\vec{r}) = \epsilon_i \phi_i(\vec{r}), \quad (3.11)$$

where $\phi_i(\vec{r})$ is the normalized one-electron orbital function. The potential function is

$$V(r) = \begin{cases} -\frac{Z}{r} + \int_{r' < R} \frac{\rho(r')}{|\vec{r} - \vec{r}'|} - \frac{[3\pi^2 \rho(r)]^{1/3}}{\pi} - \nu & \text{for } r < R \\ -\frac{(3\pi^2 \bar{\rho})^{1/3}}{\pi} & \text{for } r > R, \end{cases} \quad (3.12)$$

where R is the radius of the cavity which is electrically neutral, and is determined by the conditions of the plasma. The Lagrangian multiplier ν is given by

$$\nu = \left\{ \left[4 - \frac{\bar{\rho}}{\rho(R)} \right] (3\pi^2 \bar{\rho})^{1/3} - 3[3\pi^2 \rho(R)]^{1/3} \right\} / 4\pi. \quad (3.13)$$

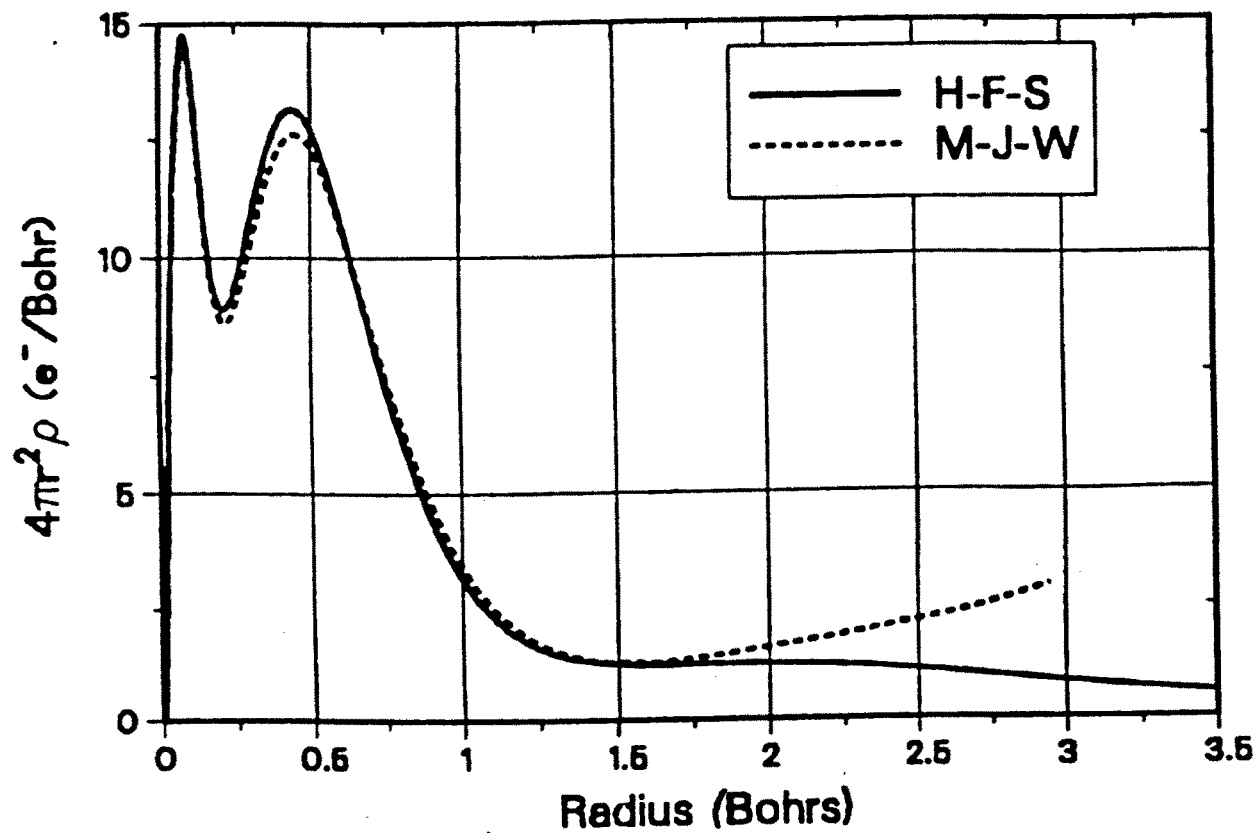


Figure 3.2. Radial electron density profiles for neutral aluminum atoms. Results for free atoms [H-F-S] and atoms within a solid-state [M-J-W] lattice are shown.

The electron density itself is given in terms of normalized one-electron orbital functions and muffin-tin approximation

$$\rho(r) = \begin{cases} \frac{\int \rho_-(\vec{r}) \sin \theta d\theta d\varphi}{4\pi} & r < R \\ \frac{\int_{x>R} \rho_-(\vec{x}) d\vec{x}}{\int_{x>R} d\vec{x}} = \bar{\rho} & r > R \end{cases} \quad (3.14)$$

$$\rho_-(\vec{r}) = \sum_i n_i |\phi_i(\vec{r})|^2$$

and the orbital occupation number is determined by the Fermi-Dirac distribution function:

$$n_i = \frac{1}{\exp\left[\frac{(\epsilon_i - \mu)}{kT}\right] + 1}, \quad (3.15)$$

where μ is the chemical potential of the plasma. The sum in Eq. (3.14) includes electrons in ground states, excited states, and an integral over the continuum. The continuum states are treated on the same basis as the bound states in this model, and as a result there is a smooth transition from bound state to narrow resonance and then to broad resonance. The implication of this treatment is that there is no sharp cutoff in the statistical distribution between “bound” and “free” electrons.

The electron density distributions generated by this atomic model are shown in Fig. 3.4 and Fig. 3.5. Figure 3.4 shows the calculated electron density distribution of a gold atom at normal matter density along with that of the isolated atom Dirac-Fock calculation. It is seen that while the muffin-tin electron density distribution is almost identical to that of the isolated atom for inner-shell electrons, there is a significant difference in the outer-shell regime. The temperature effect on electron density distributions is shown in Fig. 3.5. As the temperature increases, more and more electrons are excited and ionized. Therefore, we see that the electron density decreases in the inner region and increases in the outer region. It is important to note that the muffin-tin model provides a self-consistent picture for electrons in all states.

3.4. The Random-Phase-Approximation Stopping Interaction Function

For ICF-relevant hot dense plasmas, the standard Lindhard stopping number (Eq. 3.4) is no longer valid. In order to extrapolate the zero-temperature Lindhard stopping quantity to plasmas at any temperature, Maynard and Deutsch [31] have developed a model which makes use of the full RPA dielectric function to give formulae for the temperature-dependent stopping number of electron stopping:

$$L = \frac{6}{\pi\chi^2} \int_0^{V/V_F} u du \int_0^\infty dz \frac{z^3 \chi^2 f_2(u, z)}{[z^2 + \chi^2 f_1(u, z)]^2 + [\chi^2 f_2(u, z)]^2} \quad (3.16)$$

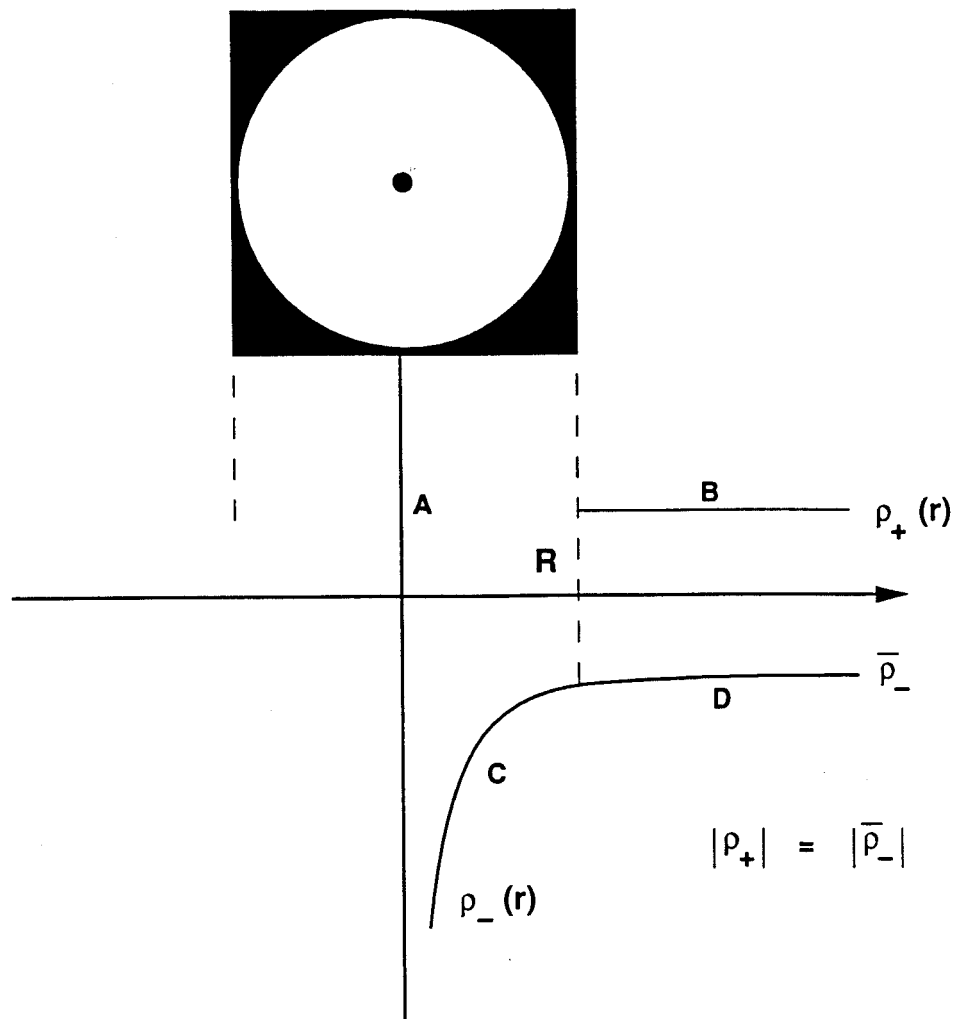


Figure 3.3. A schematic charge distribution for the “muffin-tin” atomic model: (a) a point nucleus at the center of a spherical cavity; (b) a constant positive charge density outside the cavity which represents surrounding ions; (c) a spherically symmetric electronic charge density inside the cavity; (d) a volume averaged electronic charge density outside the cavity. R is the radius of the cavity.

Radial Charge Density Profiles for Neutral Gold Atoms

(T=0)

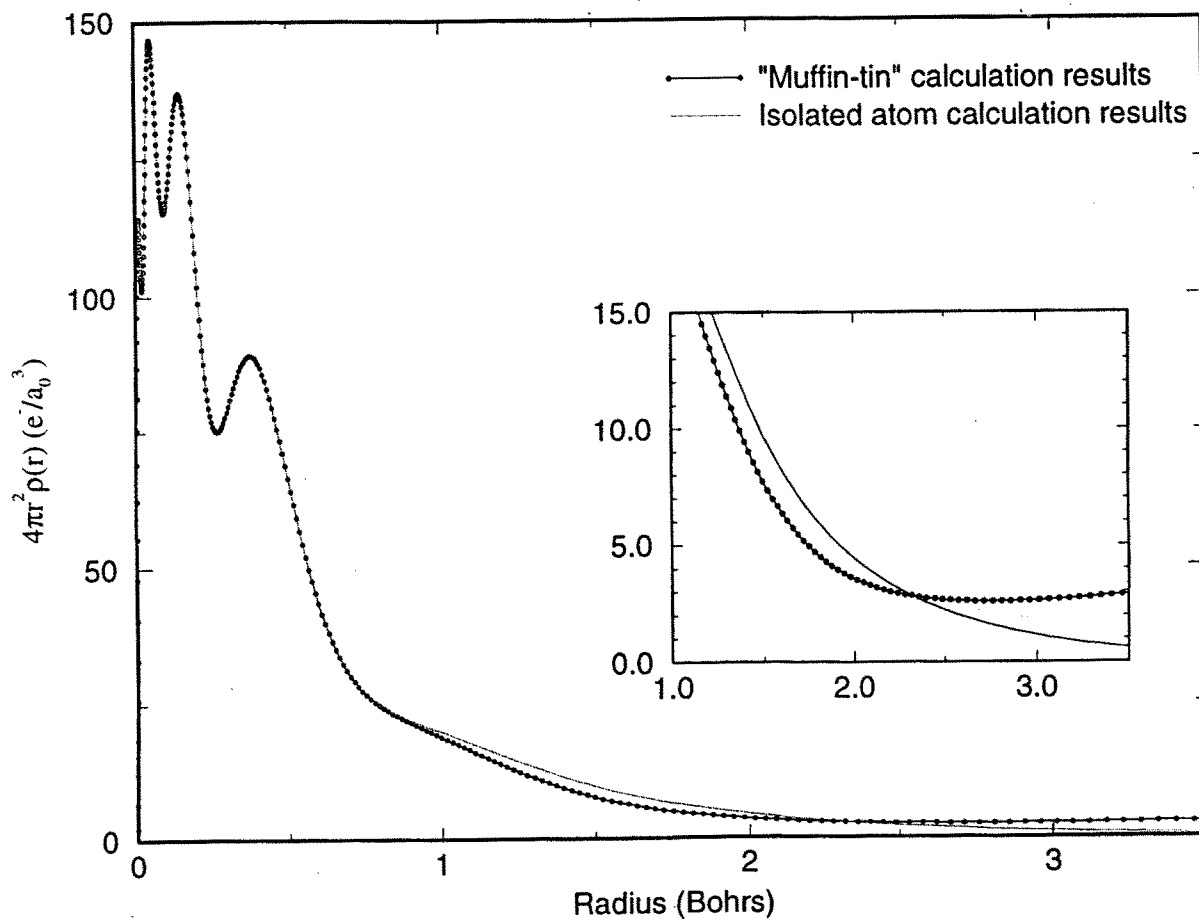


Figure 3.4. Comparison of isolated atom Dirac-Fock radial electron density with that from the muffin-tin model.

Radial Charge Density Profiles for Au at Various Temperatures

(plasma density = 1.93 g/cm^3)

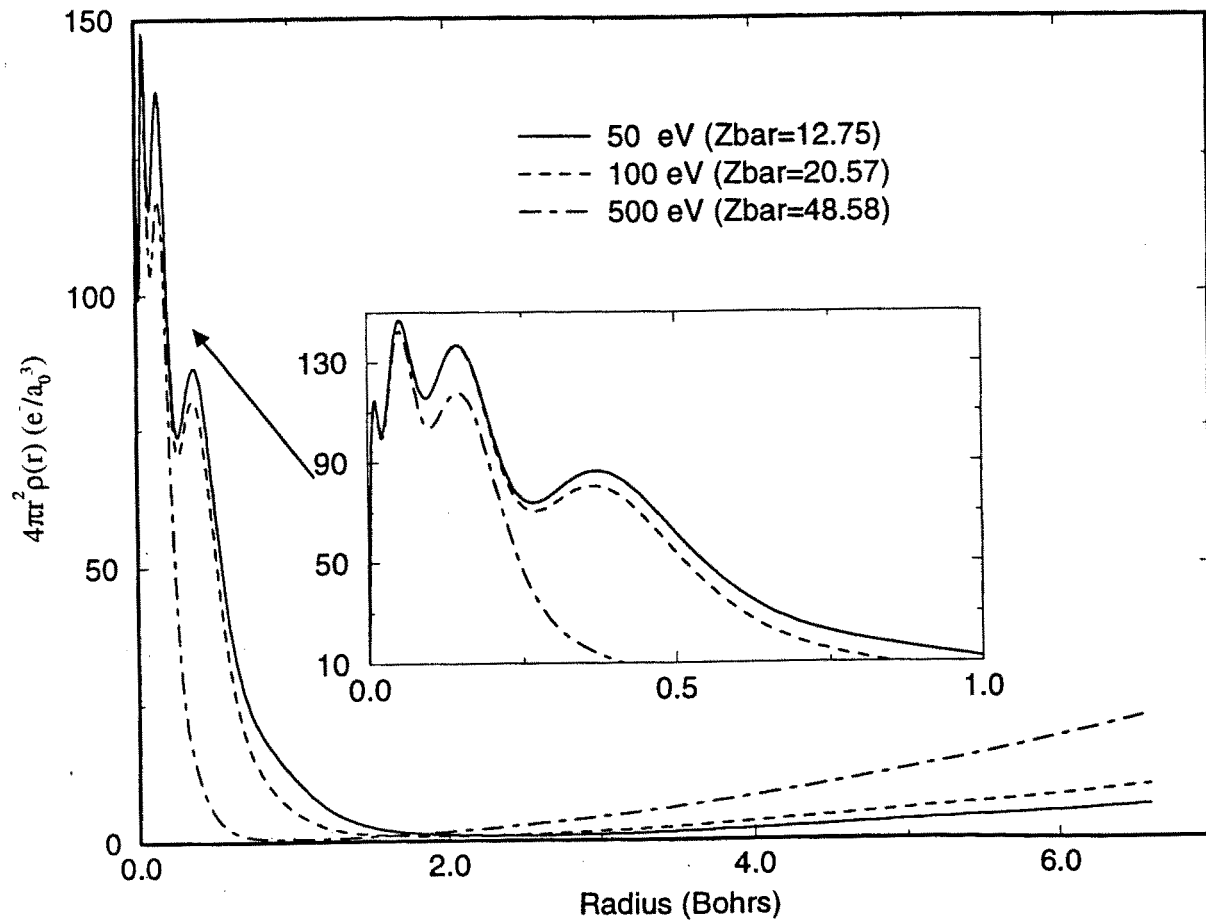


Figure 3.5. Radial electron density profiles for gold at selected temperatures. Results are calculated with muffin-tin atomic model.

where

$$f_1(u, z) = \int_0^\infty dk n^0(k) + \pi T_e \sum_{n=0}^\infty \left\{ \frac{b_n}{\gamma_n} - \frac{1}{4z} \left[\tan^{-1} \left(\frac{P_+ + a_n}{b_n} \right) + \tan^{-1} \left(\frac{P_+ - a_n}{b_n} \right) - \tan^{-1} \left(\frac{P_- + a_n}{b_n} \right) - \tan^{-1} \left(\frac{P_- - a_n}{b_n} \right) \right] \right\} \quad (3.17)$$

$$f_2 = -\frac{\pi T_e}{8z} \ln \left\{ \frac{1 + \exp \left[\frac{\gamma - P_+^2}{T_e} \right]}{1 + \exp \left[\frac{\gamma - P_-^2}{T_e} \right]} \right\} \quad (3.18)$$

with

$$\begin{aligned} n^0(k) &= \left[\exp \left(\frac{k^2 - \gamma}{T_e} \right) + 1 \right]^{-1} \\ T_e &= \frac{T}{T_F} \\ P_\pm &= u \pm z \\ \gamma &= \alpha T_e \end{aligned} \quad (3.19)$$

and α is determined from

$$F_{1/2}(\alpha) = \frac{2}{3} T_e^{-3/2}, \quad (3.20)$$

where $F_n(\alpha)$ denotes the Fermi function. The coefficients a_n and b_n are given by

$$\begin{aligned} a_n &= \pm \frac{1}{2} \{ \gamma + [\gamma^2 + (2n+1)^2 \pi^2 T_e^2]^{1/2} \}^{1/2} \\ \text{and} \\ b_n &= \pm \frac{1}{2} \{ \gamma + [\gamma^2 + (2n+1)^2 \pi^2 T_e^2]^{1/2} \}^{1/2} \end{aligned} \quad (3.21)$$

It is important to note that with Eq. (3.17) and (3.18), one can recover two well-known results in the low- and high-temperature limits [31].

Direct application of the RPA stopping number to large scale stopping power calculations is a formidable task since f_1 is a very slowly converging quantity. We have chosen an interpolation formula of $L(T, V)$ which bridges the accurate asymptotic expression of Eq. (3.16) in both the small and large projectile velocity limits [31]:

$$L(V, T_e) = \begin{cases} L^1 = \left(\frac{V}{V_F} \right)^3 C(\chi^2, \alpha) \frac{1}{1+GV^2} & V \leq V_{\text{int}} \\ L^2 = \ln \left(\frac{2mV^2}{t\omega_p} \right) - \frac{\langle V_e^2 \rangle}{V^2} - \frac{\langle V_e^4 \rangle}{2V^4} & V \geq V_{\text{int}} \end{cases} \quad (3.22)$$

where

$$\left\langle \frac{V_e^{2n}}{V_F^2} \right\rangle = \frac{T_e^n F_{n+1/2}(\alpha)}{F_{1/2}(\alpha)} \quad (3.23)$$

$$C(\chi^2, \alpha) = \int_0^\infty \frac{dz z^3}{(z^2 + \chi^2 \int_1(z, 0))^2 \left[1 + \exp\left(\frac{z^2}{T_e} - \alpha\right)\right]} \quad (3.24)$$

and G is fixed by $L^1(V_{int}) = L^2(V_{int})$. Detailed numerical calculations have shown that the relative error of this interpolation formula is smaller than a few percent at any temperature.

In order to demonstrate the sensitivity of stopping number on temperature, we have calculated RPA stopping numbers for ions of various energies stopped in a uniform electron gas with density of 10^{23} cm^{-3} . The calculated results are shown in Fig. 3.6. We see that for slow ions, the stopping number is very sensitive to the temperature, while for fast ions the temperature effect is negligible.

3.5. Numerical Results

The stopping of protons on cold aluminum has been well-studied. We begin by studying the case of a monoenergetic beam of protons incident on an aluminum target so that we can assess the influence of the charge density distribution represented by the muffin-tin atomic model on stopping power. Figure 3.7 shows the calculated proton stopping powers in neutral aluminum as compared to experimental data. Calculated results are from models of isolated atom HFS electron distributions and muffin-tin electron distributions. It can be seen that while in the high-energy regime both atomic models give good agreement with the experimental data, the low-energy stopping power is over-predicted for the isolated atom model. It is known that low-energy ions and high-energy ions are mainly stopped by two different parts of electrons of the target atom. Most of the energy from low-energy ions is lost to outer-shell electrons, while the inner-shell electrons play a major role in stopping high energy ions. As mentioned above, while outer-shell electrons are strongly affected by the surrounding environment, the inner-shell electron distribution is relatively stable. Significant differences occur in the spatial variation of the muffin-tin electron densities and isolated atom HFS electron densities away from the interior of the target atom due to solid-state bonding effects. For inner-shell electrons, especially for K-shell electrons, the density distributions of the two models are almost identical. The good overall agreement of the calculated stopping power with the experimental data demonstrates that the electron density distribution of the muffin-tin atomic model is quite accurate for both outer and inner shell electrons of an atom in a solid.

In Figure 3.8 the calculated proton stopping power on a cold gold target with two different atomic electron densities is shown together with experimental data [35]. It is seen that for this high-Z target, the calculated stopping power with the muffin-tin electron density shows good overall agreement with the experimental data.

Finally, we come to the main point of this work: the study of the ion stopping characteristics of hot targets using a self-consistent treatment for both bound and free electrons.

Temperature Sensitivity of Stopping Number

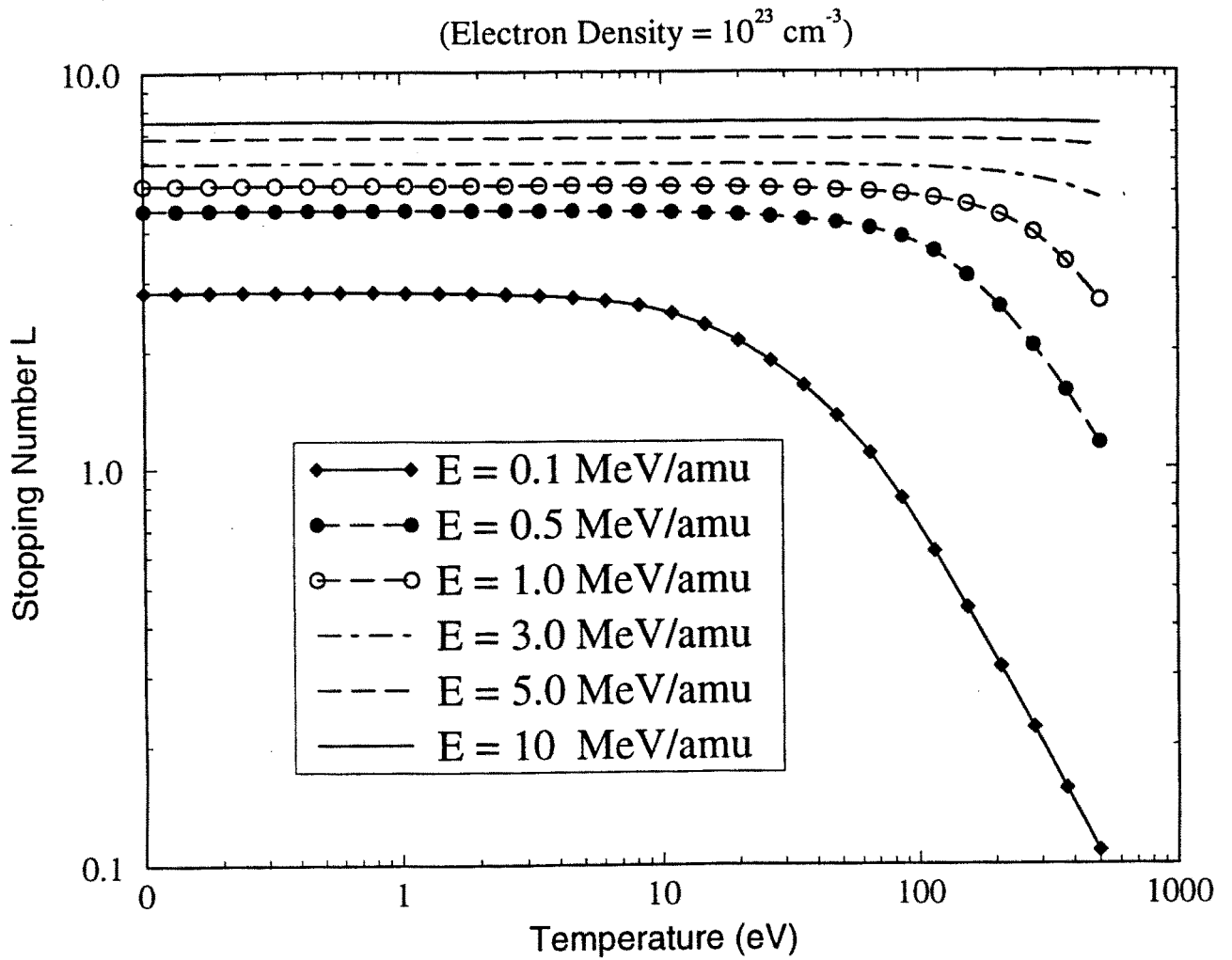


Figure 3.6. Variation in RPA stopping number with temperature for selected projectile energies.

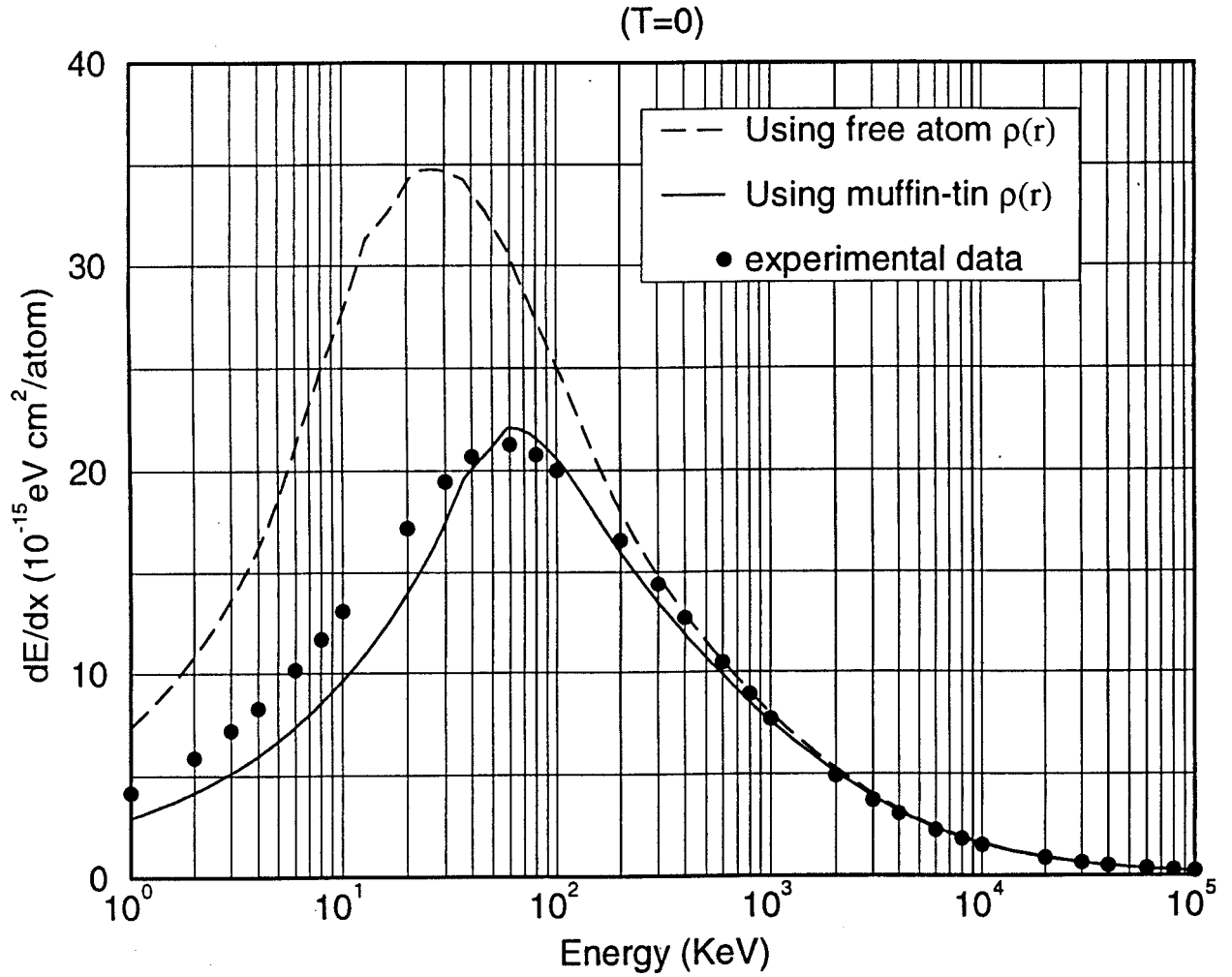


Figure 3.7. Comparison of proton stopping power in neutral aluminum as a function of energy.

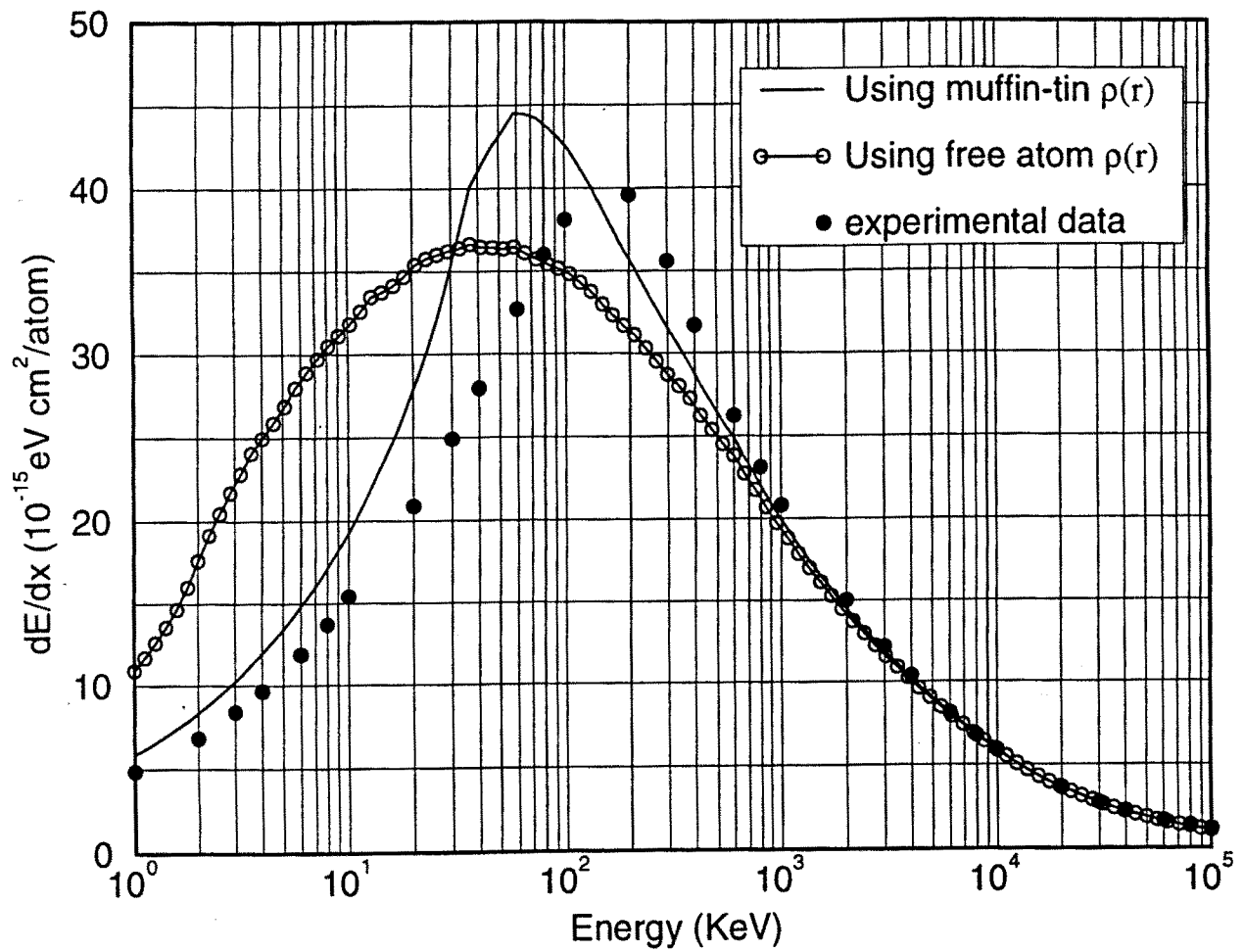


Figure 3.8. Comparison of proton stopping power in neutral gold as a function of energy.

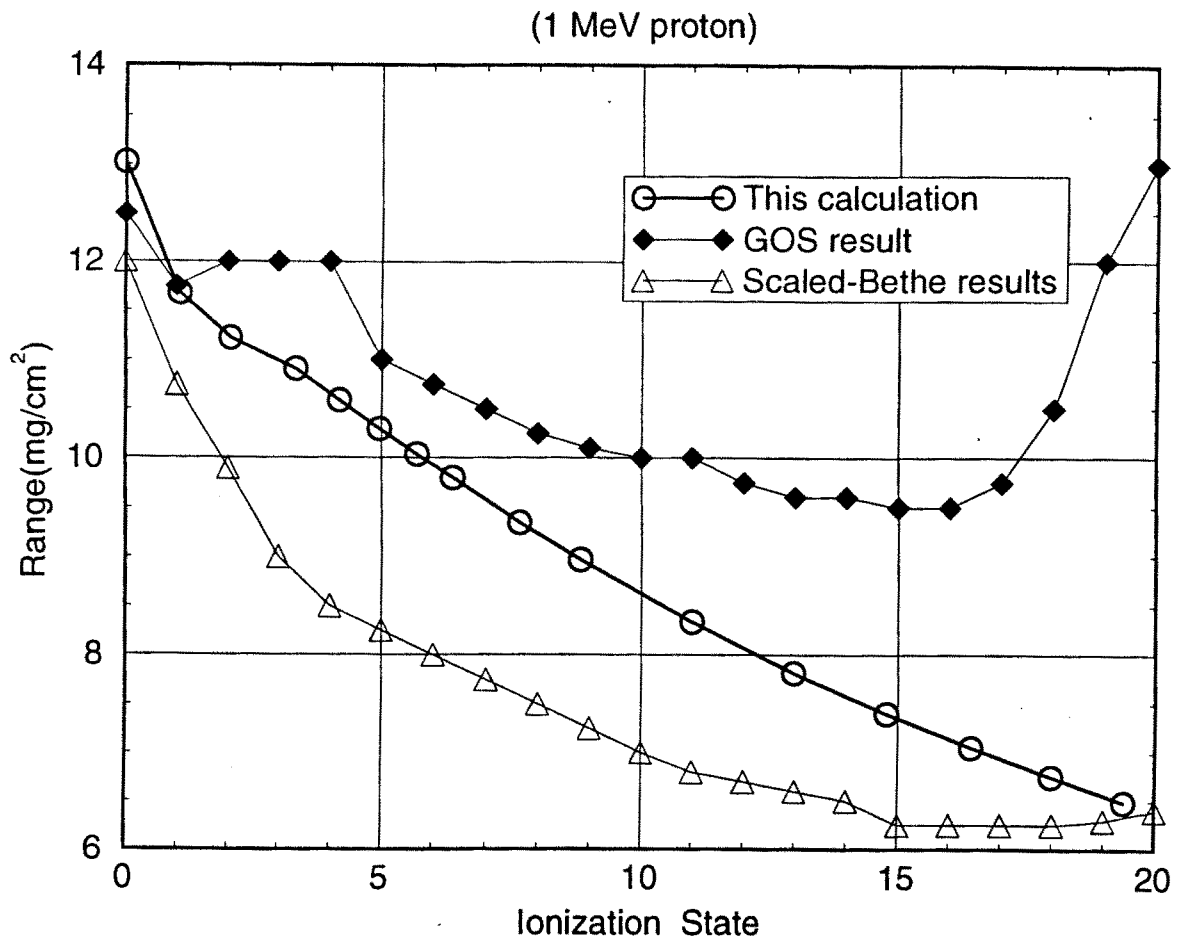


Figure 3.9. Stopping range of 1 MeV protons in gold as a function of ionization state of the target. Three different calculation results are shown.

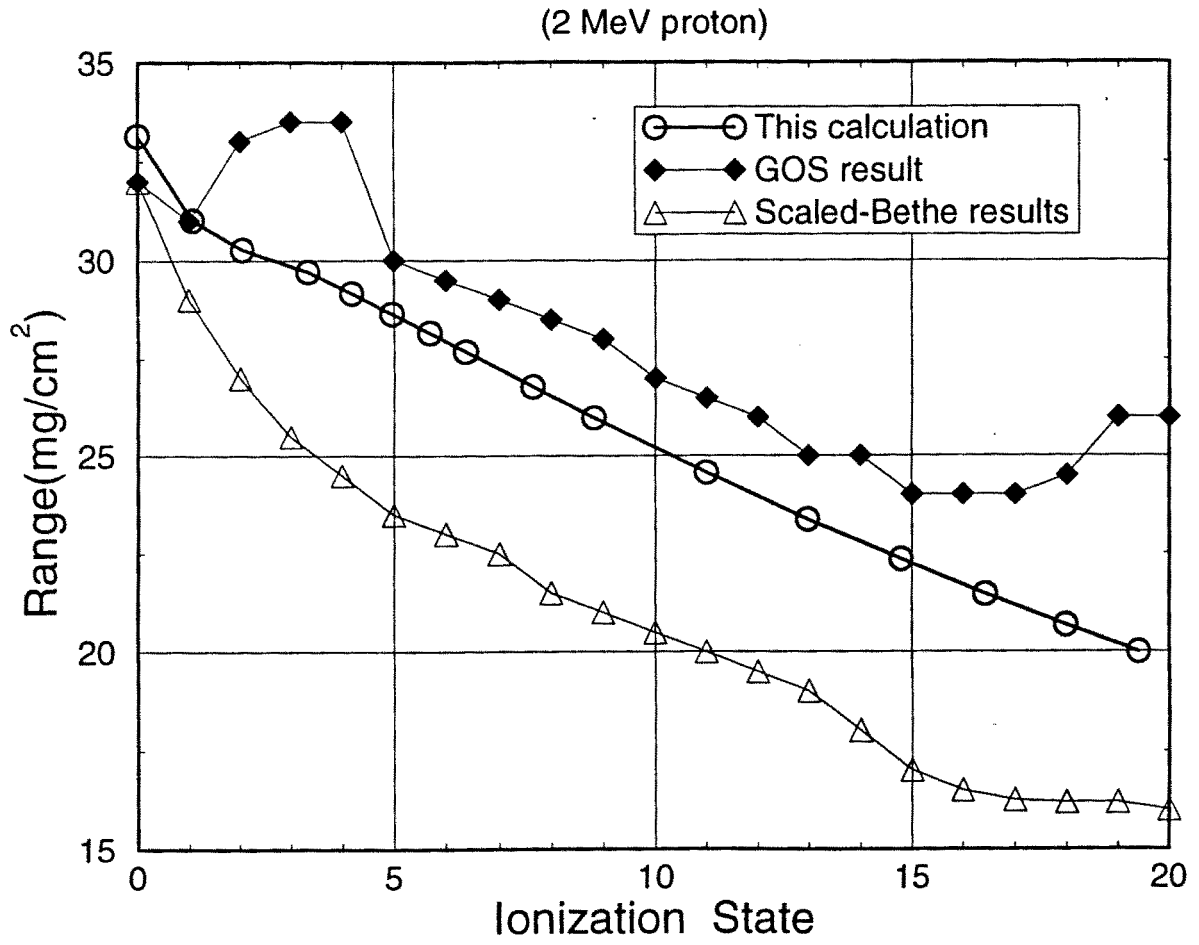


Figure 3.10. Stopping range of 2 MeV protons in gold as a function of ionization state of the target. Three different calculation results are shown.

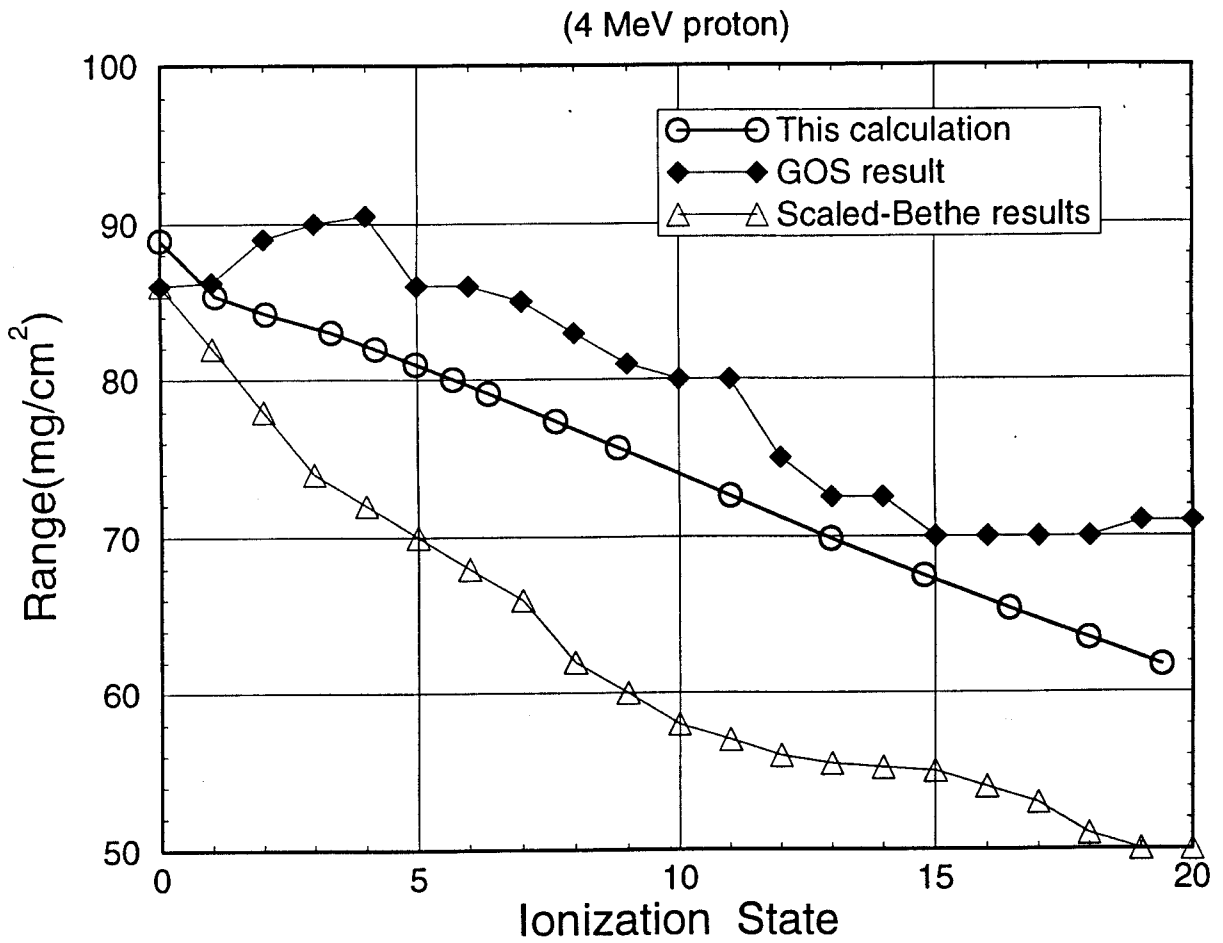


Figure 3.11. Stopping range of 4 MeV protons in gold as a function of ionization state of the target. Three different calculation results are shown.

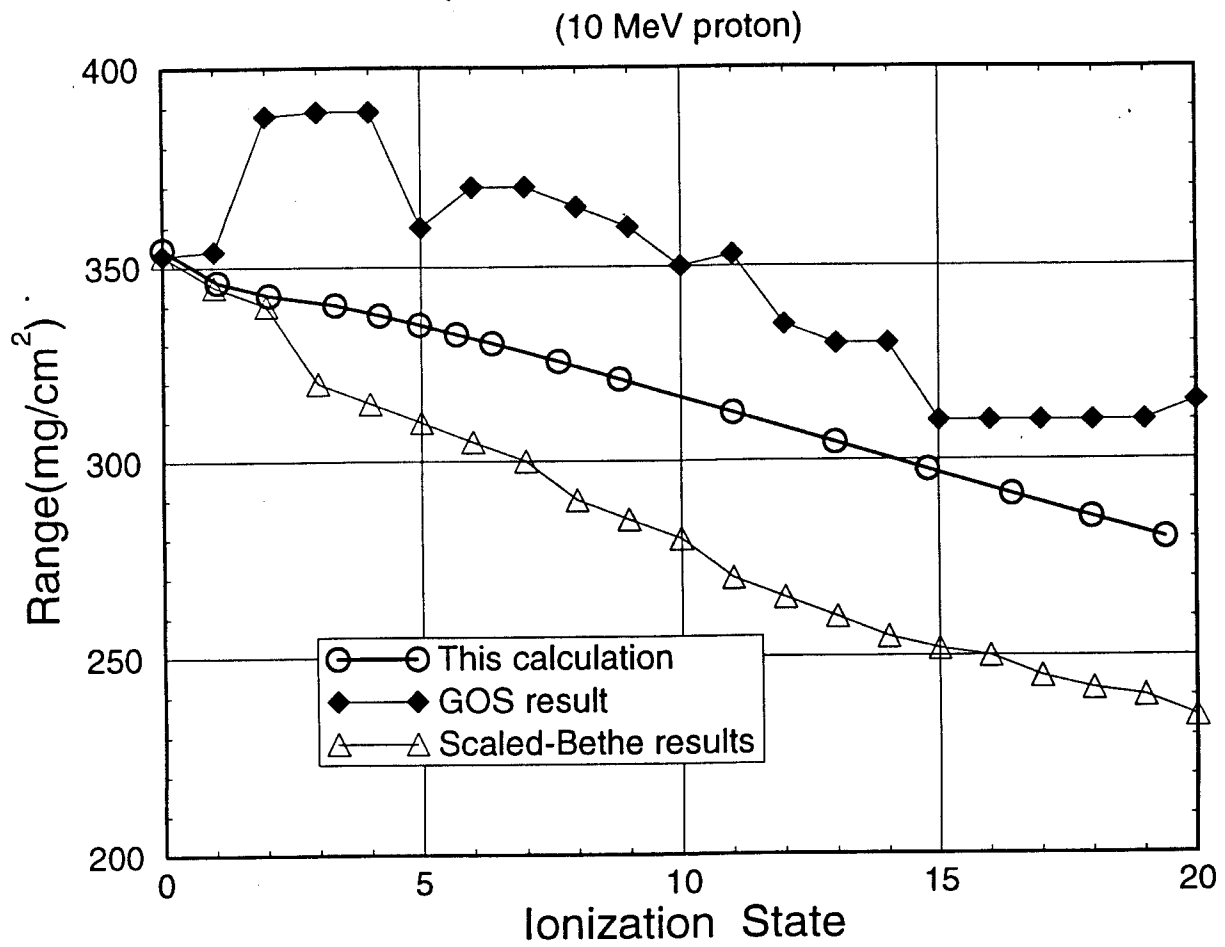


Figure 3.12. Stopping range of 10 MeV protons in gold as a function of ionization state of the target. Three different calculation results are shown.

In this regard, we have calculated the proton range in a hot gold target with the model discussed in previous sections and made comparisons with the results of the Generalized Oscillator Strength (GOS) model [36] and of the scaled-Bethe model [22]. Figures 3.9–3.12 show calculated results for the stopping range in gold with ionization for protons of various energies. Results of this work, GOS results, and those using the scaled-Bethe model are shown. There are two points of interest in this comparison. First, the range is predicted to decrease more slowly with ionization for GOS results. Our results lie somewhere between GOS results and scaled-Bethe results. Secondly, our results show a smooth decrease with ionization in all the cases, while the GOS model predicts that the range for high-energy projectiles can initially increase with ionization of the atom.

It has been argued [22] that such an initial range lengthening characteristic in high-Z targets can be interpreted in terms of the difference in the interaction velocities of the target electrons when they are in their bound and free states. It should be noted that the key point of this interpretation is that there is a sharp cut between the bound and free electrons. The characteristic velocity of a bound electron is given by the local Fermi velocity and the characteristic velocity of a free electron is the thermal velocity. However, this is not the case in reality. On the other hand, the GOS model neglects the contributions from bound electrons in excited states. These excited electrons are less bound than those in the subshells of the ground configuration, and their characteristic velocities should be somewhere between the local Fermi velocity and the thermal velocity. If the stopping effect from excited electrons is included in a GOS calculation, we expect that the initial range lengthening features in the GOS results could be removed. This needs to be verified in future investigations. In our calculations, contributions from electrons in all states (ground, excited, and continuum states) are essentially taken into account in a self-consistent manner. This characteristic of the model is reflected in Eq. (3.14). The sum in Eq. (3.14) runs through the ground state, all excited states, and continuum states. The population of each state is determined by the Fermi-Dirac distribution function. The differences between our results and GOS results demonstrate that the contributions from electrons in excited states, which can be interpreted as “quasi-bound” electrons in high density plasmas, is important in stopping power calculations and must be treated accurately.

3.6. Summary

We have developed a model to study the energy deposition of an ion in a material of arbitrary composition, density, and temperature. This model includes a reasonably sophisticated treatment of the electron density distribution of an atom embedded in a hot plasma and a full Random Phase Approximation stopping number which extrapolates the zero-temperature Lindhard stopping number to arbitrary temperatures. Therefore, it can accommodate a wide range of temperatures and densities relevant to ICF plasmas. Comparisons with experimental data indicate that this model provides quite accurate ion stopping powers in cold materials, including both low-Z

and high- Z targets. For finite temperature plasmas, the model accounts for the stopping effects due to electrons in ground states, excited states, and continuum states in a self-consistent manner. We have also compared our calculated results of proton ranges in gold plasmas with those from a GOS model and a scaled-Bethe model. Our results lie between the results of these two different models. Unlike the GOS results, no initial range lengthening feature is seen in our calculated results. We conclude that this difference could be caused by the different treatments of less bound electrons in excited states.

It is also worth pointing out that this model is developed in the framework of first Born approximation for the projectile. For low-energy heavy ions, the first Born approximation is no longer appropriate and higher-order Born corrections should be included [31]. This can be done by directly including the Barkas term [37] and Bloch term [38] into our model. We expect to further develop the model in this direction in the future.

Acknowledgement

Support for this work provided by Sandia National Laboratories, U.S. Department of Energy.

References

1. Mehlhorn, T.A., *J. Appl. Phys.* **52**, 6522 (1981).
2. Bailey, J.E., private communication (1994).
3. Chung, H.-K., MacFarlane, J.J., Moses, G.A., and Wang, P., Presented at APS Division of Plasma Physics Meeting, Bull. Amer. Phys. Soc. 39, 1688, Nov. 1994
4. MacFarlane, J.J., Wang, P., Bailey, J.E., Mehlhorn, T.A., Dukart, R.J., and Mancini, R.F., *Phys. Rev.* **E47**, 2748 (1993).
5. MacFarlane, J.J., “NLERT – A Code for Computing the Radiative Properties of Non-LTE Plasma,” Fusion Power Associates Report FPA-93-6 (December 1993).
6. Wang, P., MacFarlane, J.J., and Moses, G.A., *Phys. Rev.* **E48**, 3934 (1993).
7. Wang, P., “ATBASE User’s Guide,” Fusion Power Associates Report FPA-93-7 (December 1993).
8. Maron, Y. and Filuk, A., private communication (1994).
9. MacFarlane, J.J., Moses, G.A., and Peterson, R.R., “BUCKY-1 – A 1-D Radiation-Hydrodynamics Code for Studying Inertial Fusion Plasmas,” University of Wisconsin Fusion Technology Institute Report, in preparation (1995).
10. Haill, T.A., private communication (1995).
11. Moses, G.A., Magelssen, G., Israel, R., Spindler, T., and Goel, B., “PHD-IV – A Plasma Hydrodynamics, Thermonuclear Burn, Radiative Transfer Computer Code,” University of Wisconsin Fusion Technology Institute Report UWFD-194 (August 1985).
12. Olson, G.L., and Kunasz, P.B., *J. Quant. Spectrosc. Radiat. Transfer* **38**, 325 (1987).
13. Apruzese, J.P., Davis, J., Duston, D., and Whitney, K.G., *J. Quant. Spectrosc. Radiat. Transfer* **23**, 479 (1980).
14. Apruzese, J.P., *J. Quant. Spectrosc. Radiat. Transfer* **34**, 447 (1985).
15. Peterson, R.R., MacFarlane, J.J., and Moses, G.A., “CONRAD – A Combined Hydrodynamics-Condensation/Vaporization Computer Code,” University of Wisconsin Fusion Technology Institute Report UWFD-670 (July 1988).
16. Moses, G.A., Peterson, R.R., and McCarville, T.J., “MF-FIRE — A Multifrequency Radiative Transfer Hydrodynamics Code,” *Comput. Phys. Commun.* **36**, 249 (1985).

17. MacFarlane, J.J., “Collisional-Radiative Equilibrium (CRE) Model for the CONRAD Radiation-Hydrodynamics Code,” University of Wisconsin Fusion Technology Institute Report UWFD-937 (December 1993).
18. MacFarlane, J.J., Peterson, R.R., Wang, P., and Moses, G.A., “Radiation Transport Effects in the Target Chamber Gas of the Laser Fusion Power Reactor SIRIUS-P,” *Fusion Technology*, in press (1995).
19. Wang, P., “EOSOPA – A Code for Computing the Equations of State and Opacities of High Temperature Plasmas with Detailed Atomic Models,” University of Wisconsin Fusion Technology Institute Report UWFD-933 (December 1993).
20. MacFarlane, J.J. and Wang, P., “Theoretical Diagnostic Analysis of K_{α} Emission Spectra Obtained in PBFA-II Li Beam Experiments,” University of Wisconsin Fusion Technology Institute Report UWFD-945 (March 1994).
21. Mehlhorn, T.A., *J. Appl. Phys.* **52**, 6522 (1981).
22. Mehlhorn, T.A., Peek, J.M., McGuire, E.J., Olsen, J.N. and Young, F.C., *J. de Physique*, Colloque C8, Supplement Au Noll, **44**, 39 (1983).
23. Deutsch, C., *Lasers and Particle Beams* **2**, 449 (1984).
24. Peter, T., and Meyer-Ter-Vehn, J., *Phys. Rev.* **A43**, 1998 (1990).
25. Nardi, E., Peleg, E., and Zinamon, Z., *Phys. Fluids* **21**, 574 (1978).
26. Bethe, H.A., *Handbuch Der Physik*, Edited by S. Flugge, Springer-Verlag, Berlin, Vol. 24, 273 (1933).
27. More, R.M., *Adv. Atomic Molec. Phys.* **21**, 305 (1985).
28. Linhard, J., Scharff, M., and Schiott, H.E., *Kgl. Danske Videnskab. Selskab. Mat. Fys. Medd.* **33**, 14 (1963).
29. Rousseau, C.C., Chu, W.K., and Powers, D., *Phys. Rev.* **A4**, 1066 (1970).
30. D.A. Liberman, *Phys. Rev.* **B20**, 4981 (1979).
31. Maynard, G., and Deutsch, C., *J. de Physique* **46**, 71 (1985).
32. Linhard, J., and Scharff, M., *Mat. Fys. Medd. Dan. Vid. Selsk.* **27**, 1 (1953).
33. Moruzzi, V.L., Janak, J.F., and Williams, A.R., *Calculated Electronic Properties Of Metals*, Pergamon Press, New York (1978).

34. Lafrate, G.J., Ziegler, J.F., and Nass, M.J., *J. Appl. Phys.* **51**, 984 (1980).
35. Ziegler, J.F., *Stopping Cross Sections For Energetic Ions In All Elements*, Pergamon, New York, Vol. 5 (1980).
36. McGuire, E.J., *Phys. Rev.* **A26**, 1871 (1982).
37. Barkas, W.H., Dyer, J.W., and Heckmann, H.H., *Phys. Rev. Lett.* **11**, 26 (1963).
38. Bloch, F., *Ann. Phys.* **16**, 285 (1933).

Appendix A

Time-Dependent Collisional-Radiative Modeling for Analyzing Spectra Obtained in Light Ion Fusion Experiments

H.-K. Chung, J. J. MacFarlane, G. A. Moses, P. Wang

Presented at the APS Division of Plasma Physics Meeting
November 7–11, 1994
Minneapolis, MN

ABSTRACT

Time-Dependent Collisional-Radiative Modeling for Analyzing Spectra Obtained in Light Ion Fusion Experiments.

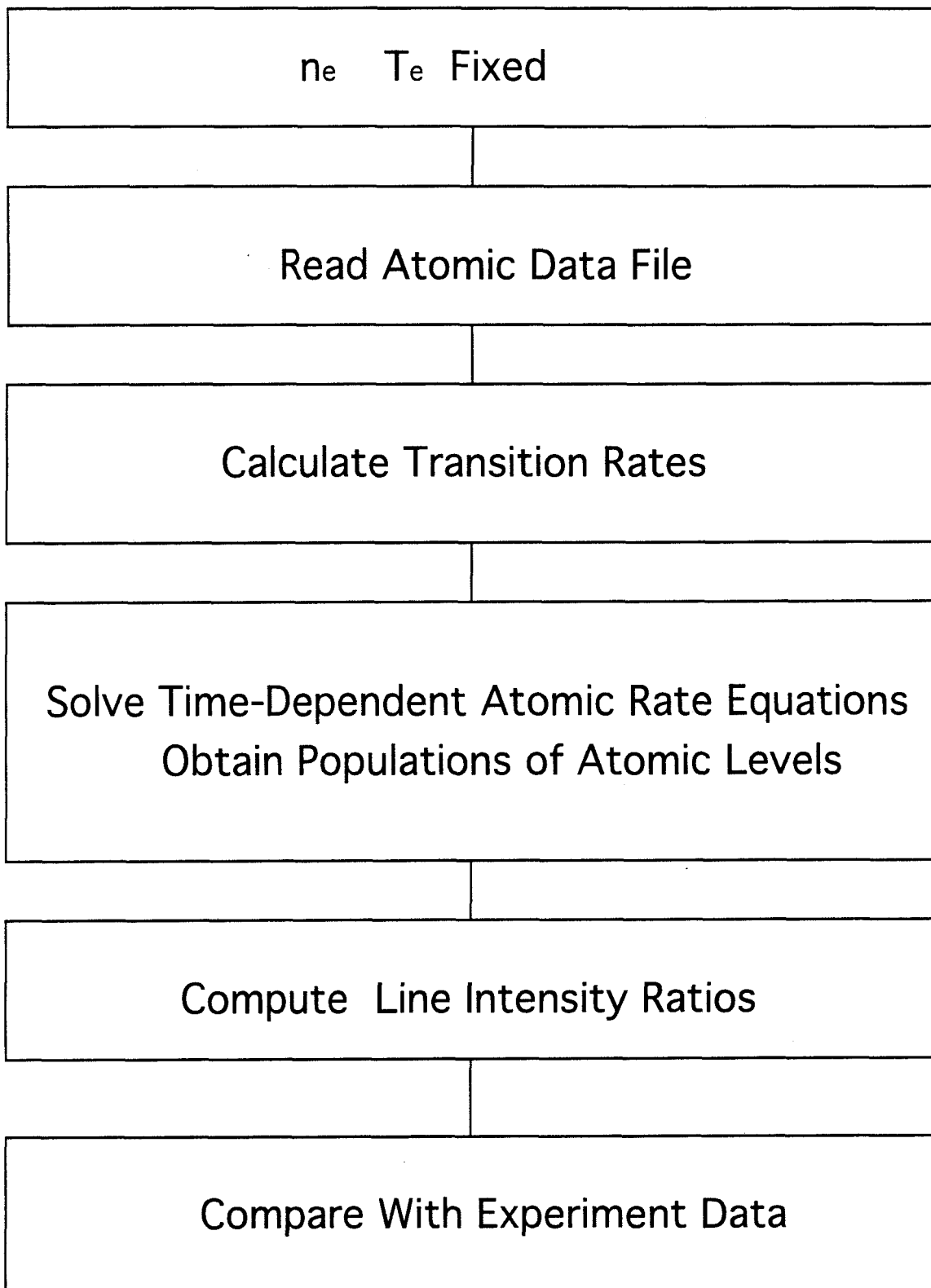
**H. K. CHUNG, J. J. MACFARLANE, G. A. MOSES,
AND P. WANG, Fusion Technology Institute,
University of Wisconsin**

We present results from time-dependent collisional-radiative calculations to investigate the properties of moderate-density plasmas in light ion fusion experiments at Sandia National Laboratories.

Our models will be applied to studies of anode plasmas and ion beam transport within a neutralizing gas. In both cases, electron densities are 10^{16} - 10^{18} cm⁻³ while experimental time scales are 10^{-9} - 10^{-8} sec. In our analysis, atomic level populations are obtained from the solution of multilevel time-dependent atomic rate equations.

We will compare our preliminary results with experimental spectra.

CODE DESCRIPTION



ATOMIC DATA DESCRIPTION

- Atomic data is prepared by Wang Ping in University of Wisconsin-Madison.
- Energy levels and Oscillator Strengths are calculated using a configuration interaction (CI) model with relativistic Hartree-Fock Wave Functions
- Photoionization cross sections are calculated for all subshells of each electronic configuration using a single-particle approximation with Hartree-Fock potential.
- Electron collision data is computed using a combination of distorted wave, Coulomb-Born, and semi-empirical methods.

ANALYSIS

If Source Rate is linear, that is, αt the Population Ratio between two arbitrary levels is independent of α , from the Rate Equation.

$$\frac{dn_1}{dt} = \alpha t - a_1 n_1 + a_2 n_2$$

$$\frac{dn_2}{dt} = b_1 n_1 - b_2 n_2$$

Divide it by ,

$$\frac{d\tilde{n}_1}{dt} = t - a_1 \tilde{n}_1 + a_2 \tilde{n}_2 \quad \tilde{n}_1 = \frac{n_1}{\alpha}$$

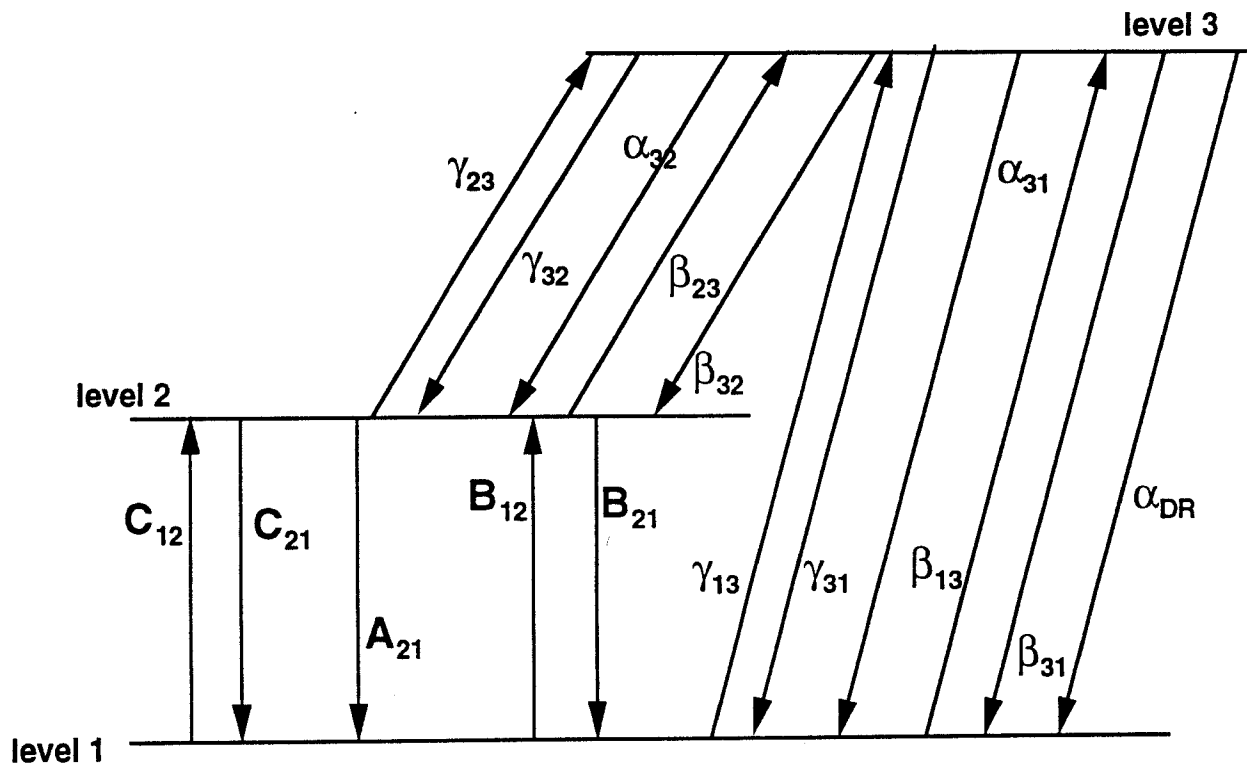
$$\frac{d\tilde{n}_2}{dt} = b_1 \tilde{n}_1 - b_2 \tilde{n}_2$$

Then the Rate Equation is independent of α ,

$$\frac{n_1}{n_2} = \frac{\tilde{n}_1}{\tilde{n}_2}$$

Therefore the Population Ratios remain the same regardless of α . Population Ratios are used for determining plasma conditions.

Schematic Illustration of the Transitions in a 3-Level Atom



- C_{ij} --> collisional excitation ($i < j$) or deexcitation ($i > j$)
- A_{ij} --> spontaneous emission
- B_{ij} --> photoexcitation ($i < j$) or stimulated emission ($i > j$)
- γ_{ij} --> collisional ionization ($i < j$) or recombination ($i > j$)
- α_{ij} --> radiative recombination
- α_{DR} --> dielectronic recombination

Fundamentals

Rate Equations: ($L \equiv$ number of atomic levels)

$$\begin{aligned}\frac{dn_1}{dt} &= n_1 P_{11} + n_2 P_{12} + \dots + n_L P_{1L} + S_1 \\ \frac{dn_2}{dt} &= n_1 P_{21} + n_2 P_{22} + \dots + n_L P_{2L} \\ &\vdots \\ \frac{dn_L}{dt} &= n_1 P_{L1} + n_2 P_{L2} + \dots + n_L P_{LL}\end{aligned}$$

The $\{P_{ij}\}$ consist of collisional and radiative terms:

Radiative rate coefficient:

$$\bar{J}_{ij} = \frac{1}{4\pi} \int_0^\infty d\nu \phi_\nu \oint d\Omega I_{\mu\nu}$$

Transport equation:

$$\mu \left(\frac{\partial I_{\mu\nu}}{\partial \tau_\nu} \right) = I_\nu - S_\nu$$

PROBLEM DESCRIPTION

1. Atomic level populations are obtained by solving multi-level time-dependant atomic rate equations.
2. A total of 170 atomic levels are considered for OI through OVI.
3. Initially, all atoms are assumed at the ground state of neutral oxygen. Cold Oxygen(OI) is continuously injected into the system; the source rate is assumed to increase linearly with time.
4. Assume that n_e , T_e are fixed.
5. Assume that the plasma is optically thin.
 - Photoexcitation effects to be included later.
6. Calculated line intensities for OIII - OV are compared with experiment.

EXPERIMENTAL DATA DESCRIPTION

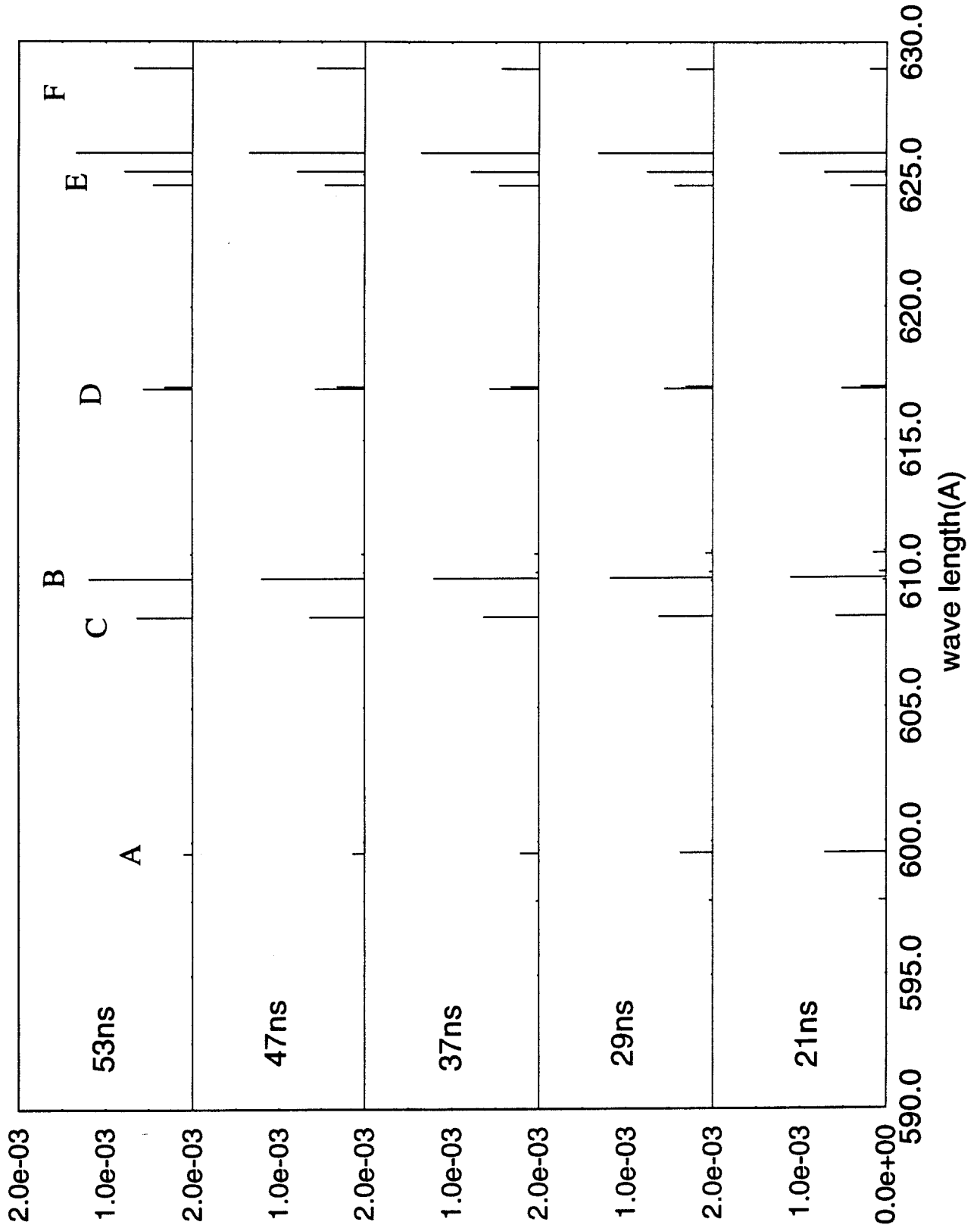
- This experiment uses VUV spectra to diagnose the anode plasma
- Oxygen emission line intensities from 580Å to 630Å have been measured.
- Detected lines:

<u>Line ID</u>	<u>Ion</u>	<u>Wave length</u>
A	OIII	600Å
B	OIII	610Å
C	OIV	608.4Å 609.8Å
D	OIV	617Å
E	OIV	625.13Å 625.62Å 625.85Å
F	OIV	629.7Å

Line intensity ratios are used to determine plasma conditions.

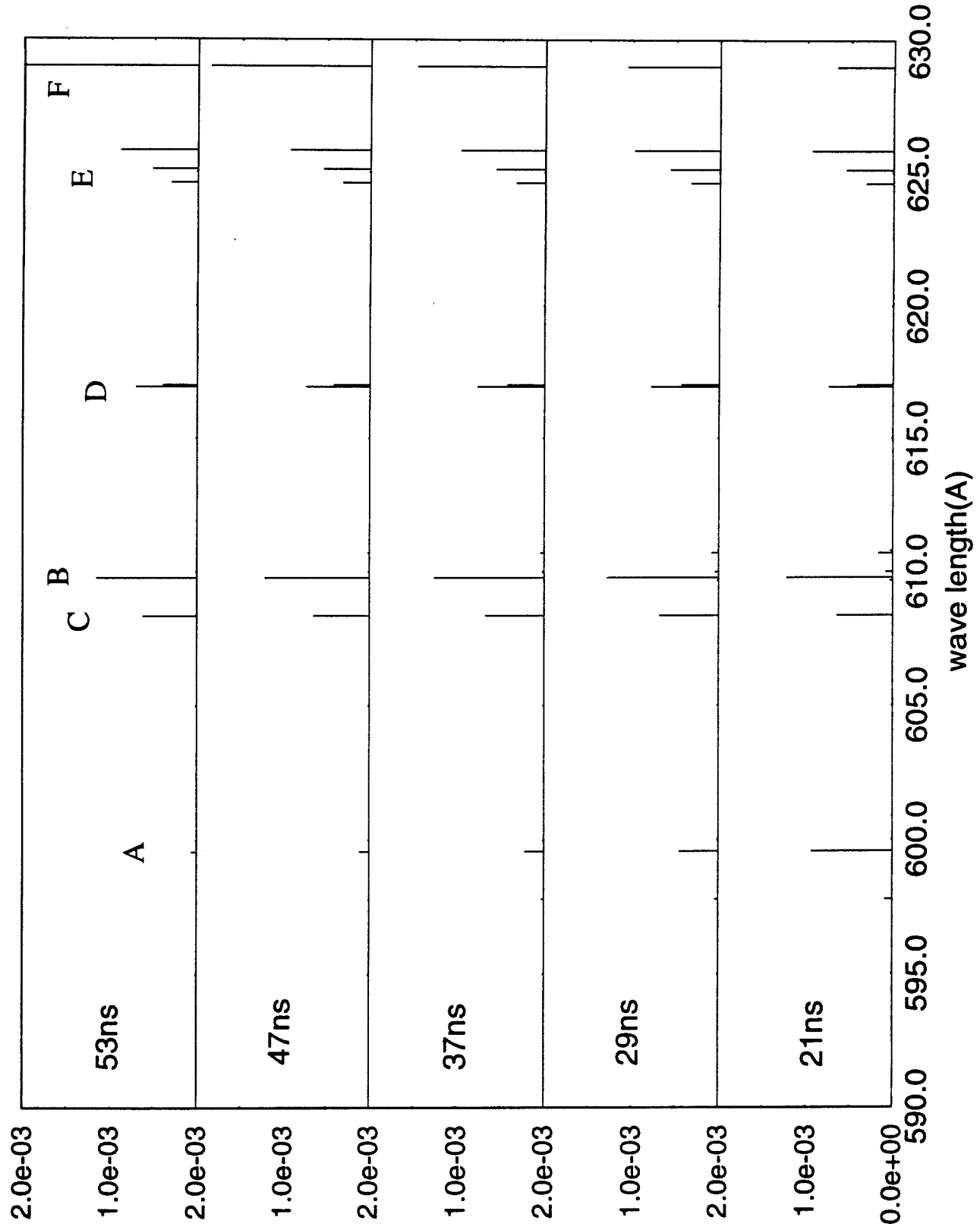
Time Evolutions of Line Intensities

Ne=1E18 Te=10eV

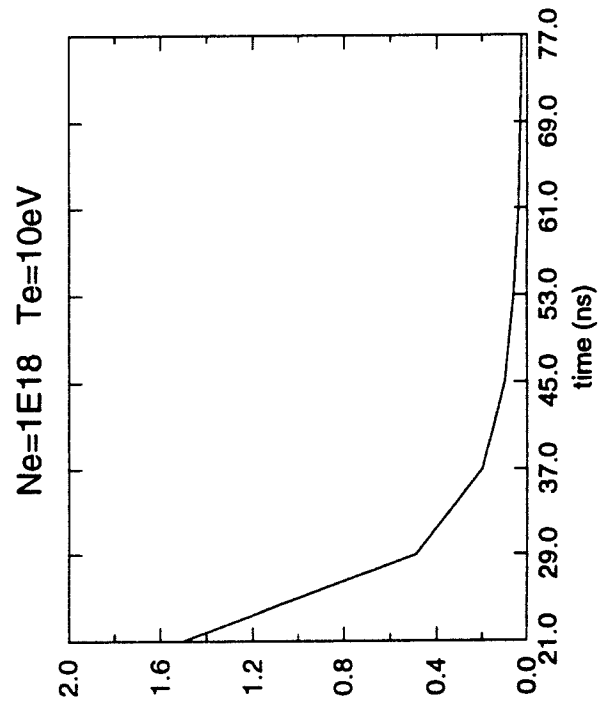
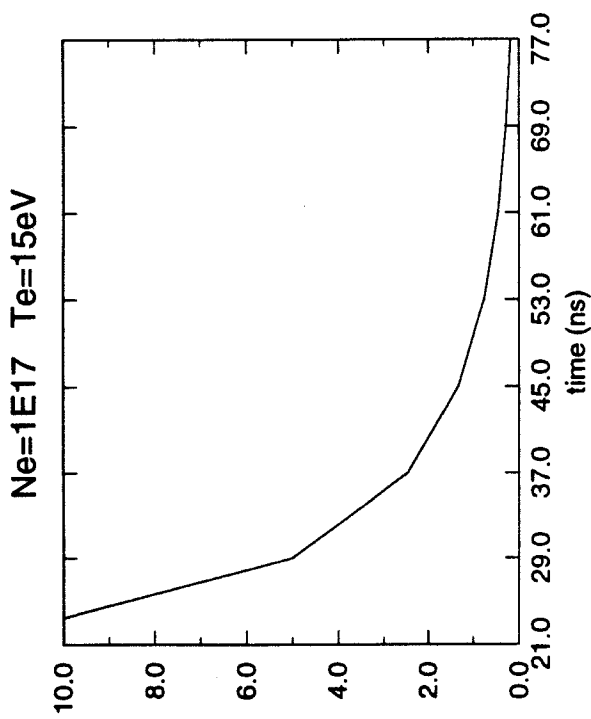
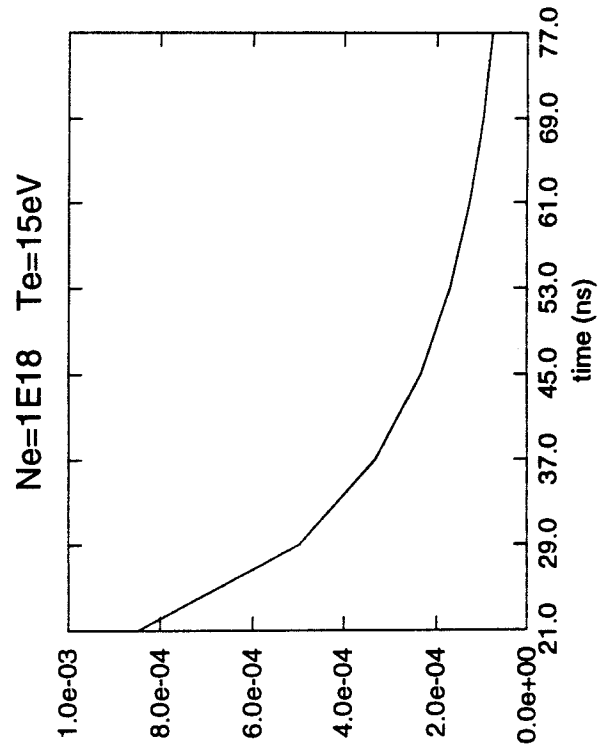
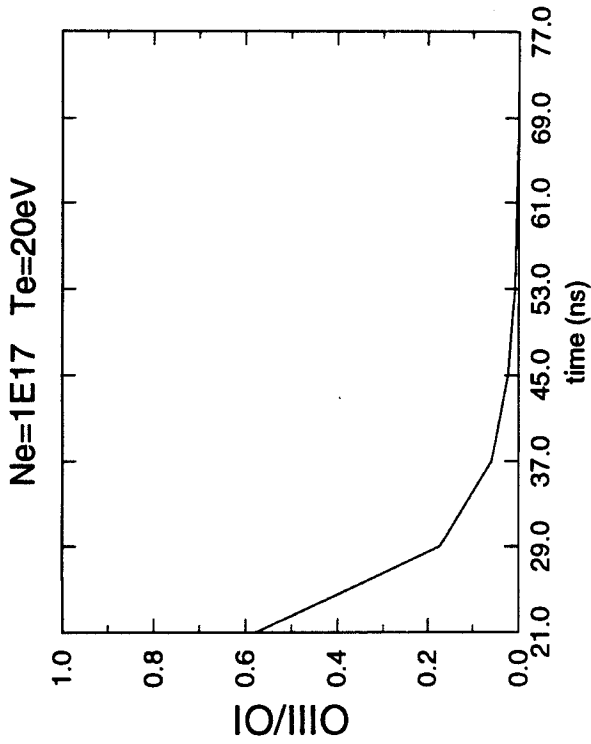


Time Evolutions of Line Intensities

Ne=1E17 Te=20eV

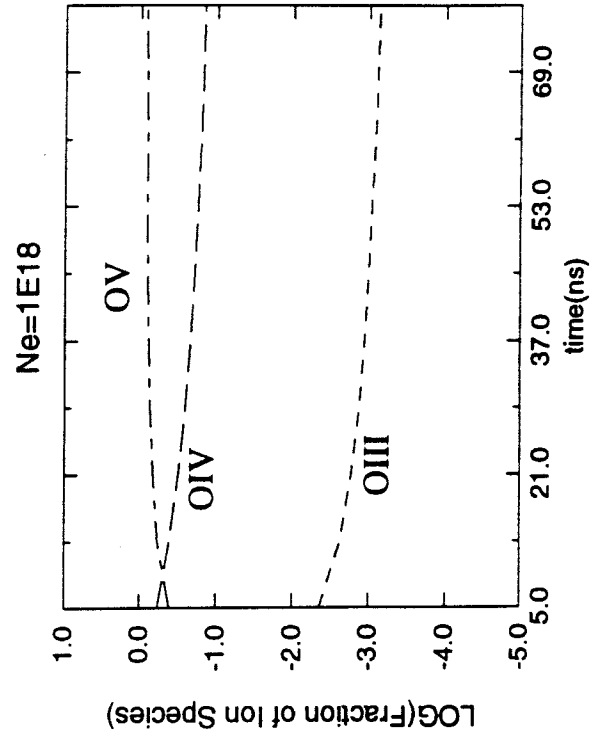
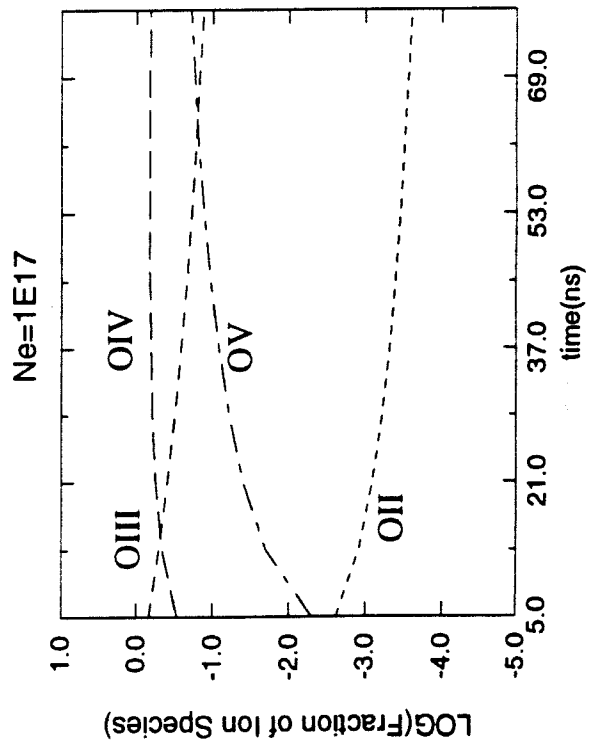
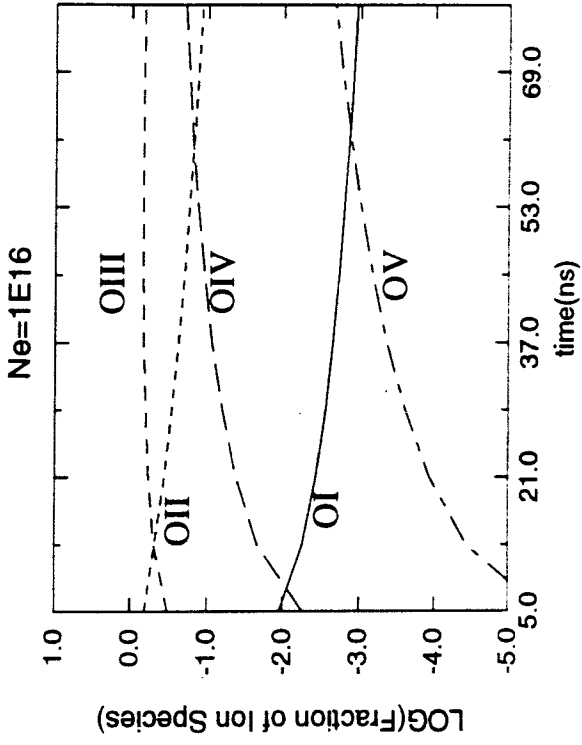


Population Ratio between $OIII\lambda 600A$ and $OVI\lambda 630A$



Time Evolution of Populations of Oxygen Ion Species

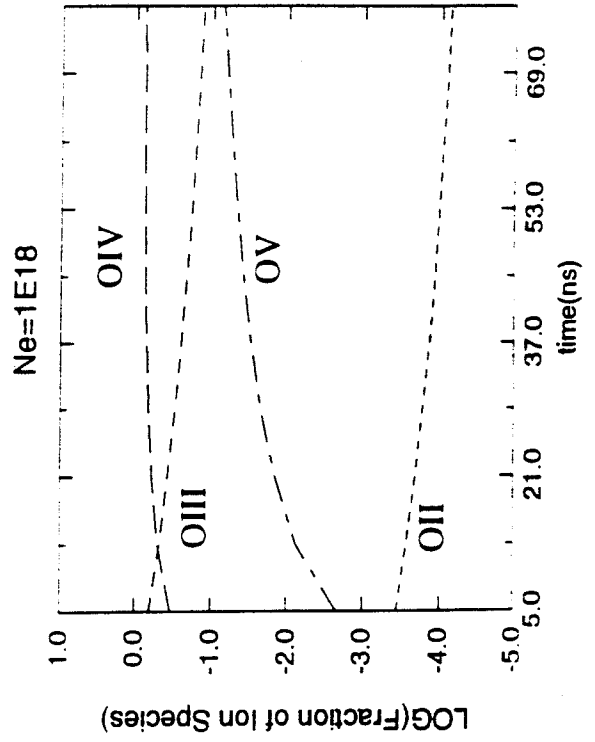
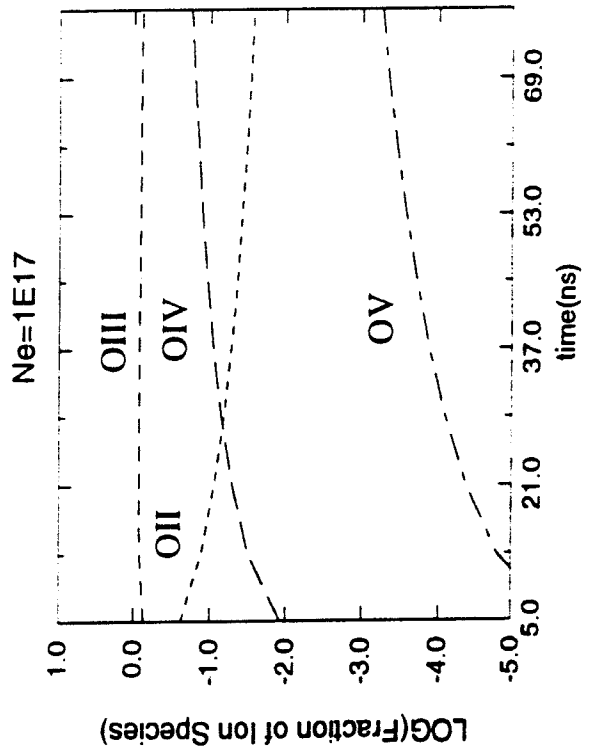
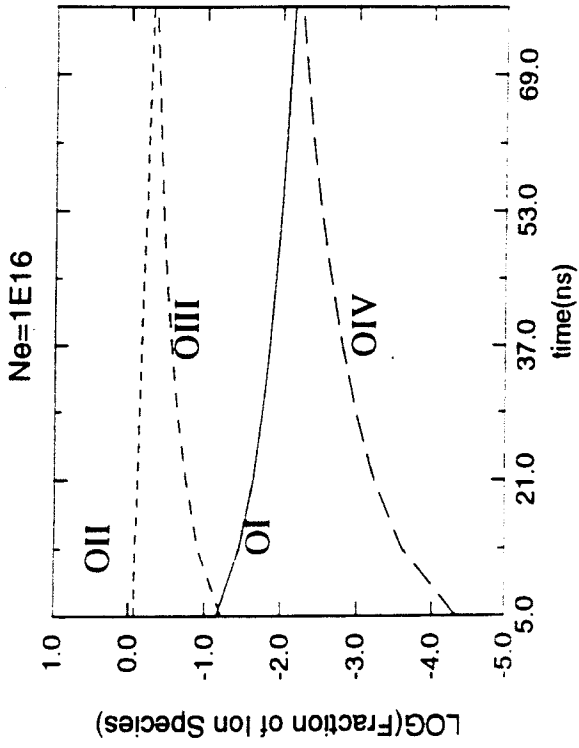
Te = 20 eV



Time Evolution of Populations of Oxygen Ion Species

Te=10eV

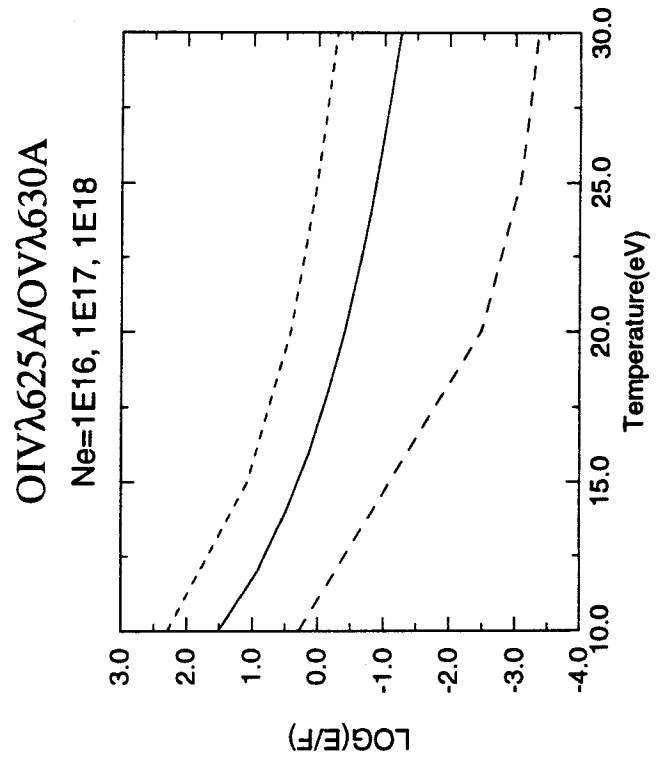
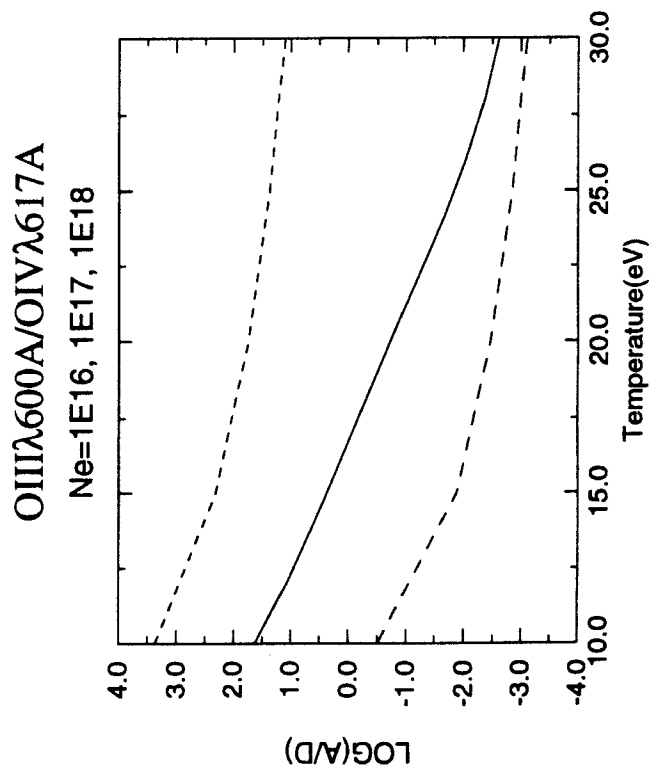
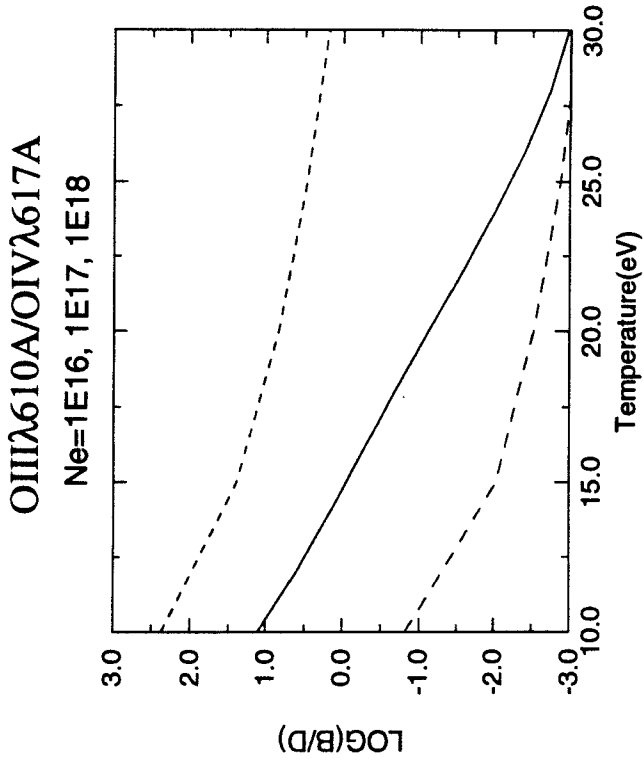
Time Dependence of Populations of Ion species are different depending on Electron Densities. Higher ionization stages can be attained at higher electron densities.



Sensitivity of Level Population Ratios on the Electron Temperature

Time = 45 ns

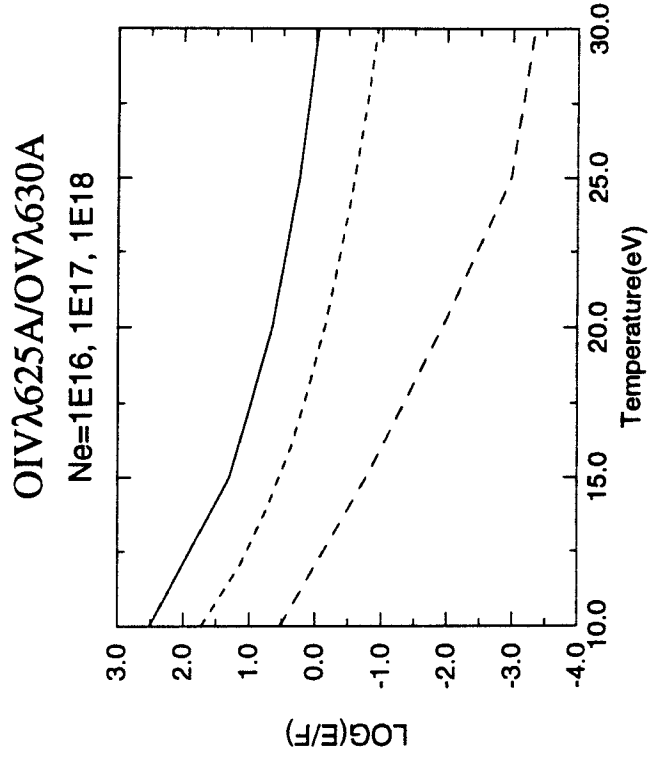
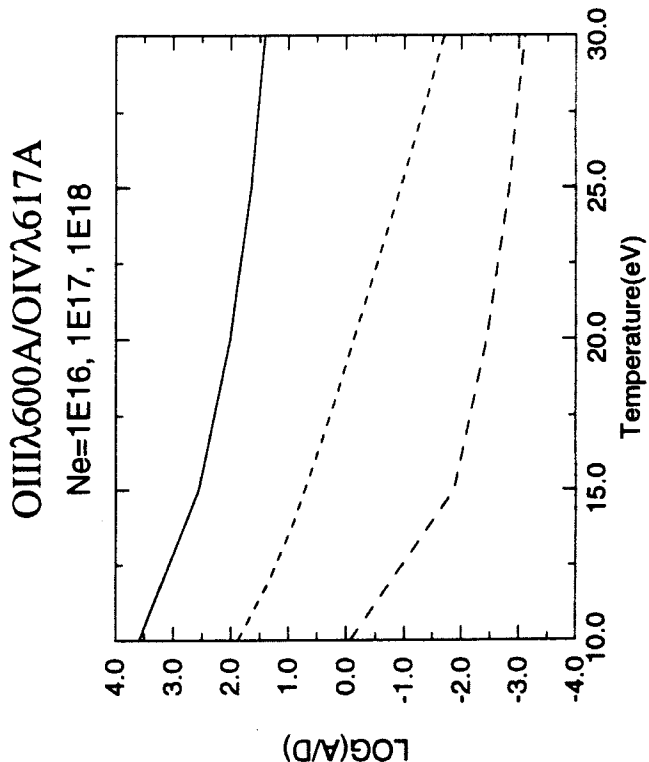
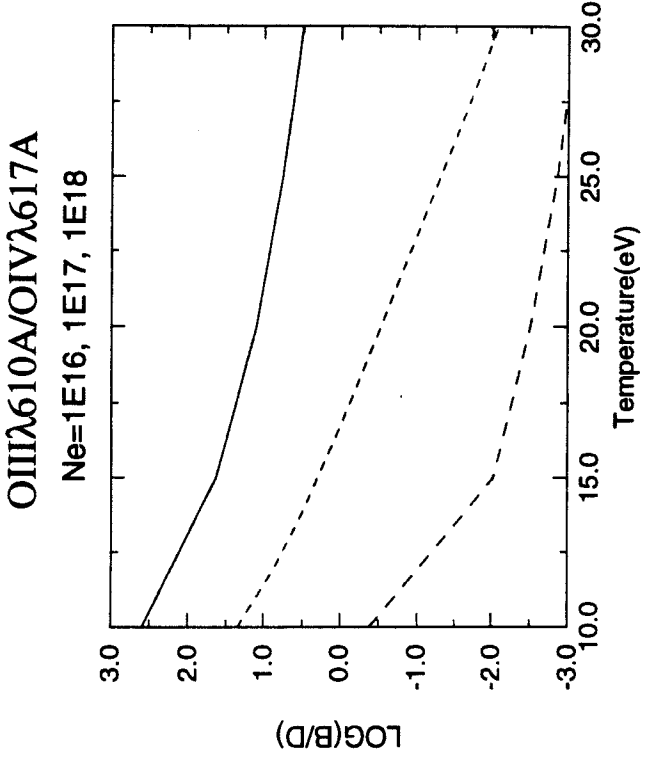
- Ne=1E17
- - - Ne=1E16
- - - Ne=1E18



Sensitivity of Level Population Ratios on the Electron Temperature

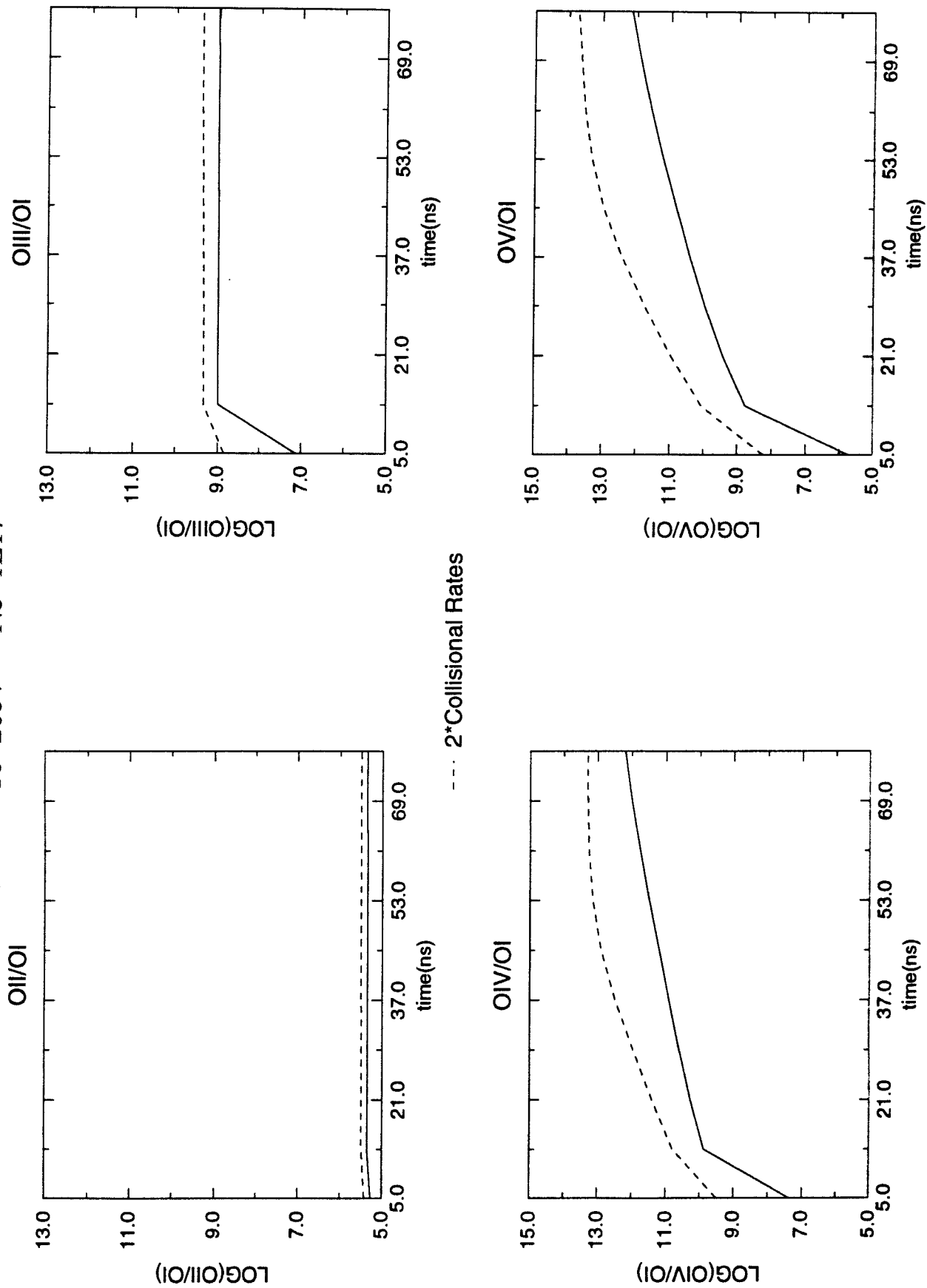
Time = 29 ns

- Ne=1E16
- - - Ne=1E17
- · - · Ne=1E18



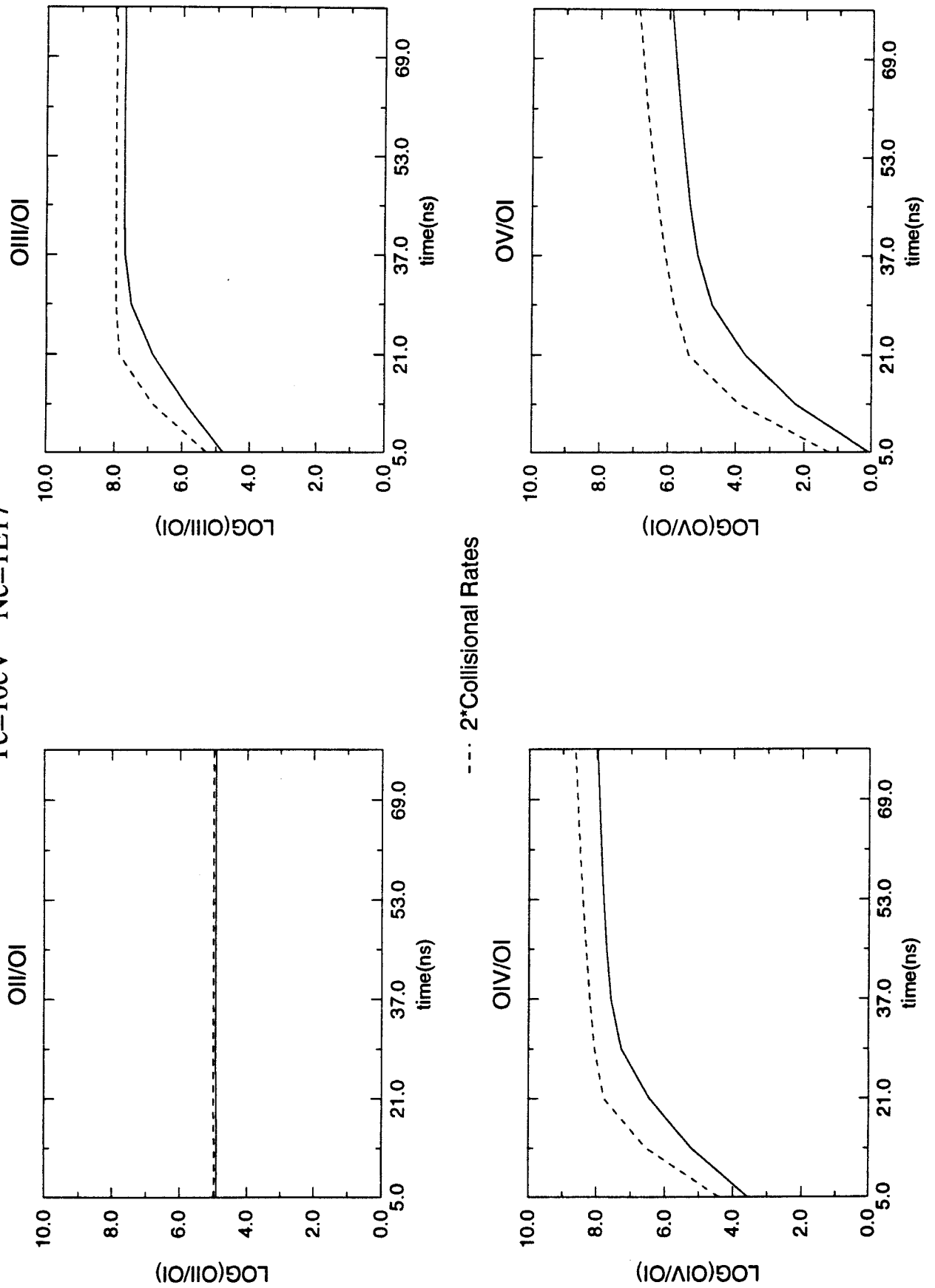
Change in Collisional Rates by a factor of 2 is more significant
in higher electron temperature

Te=20eV Ne=1E17



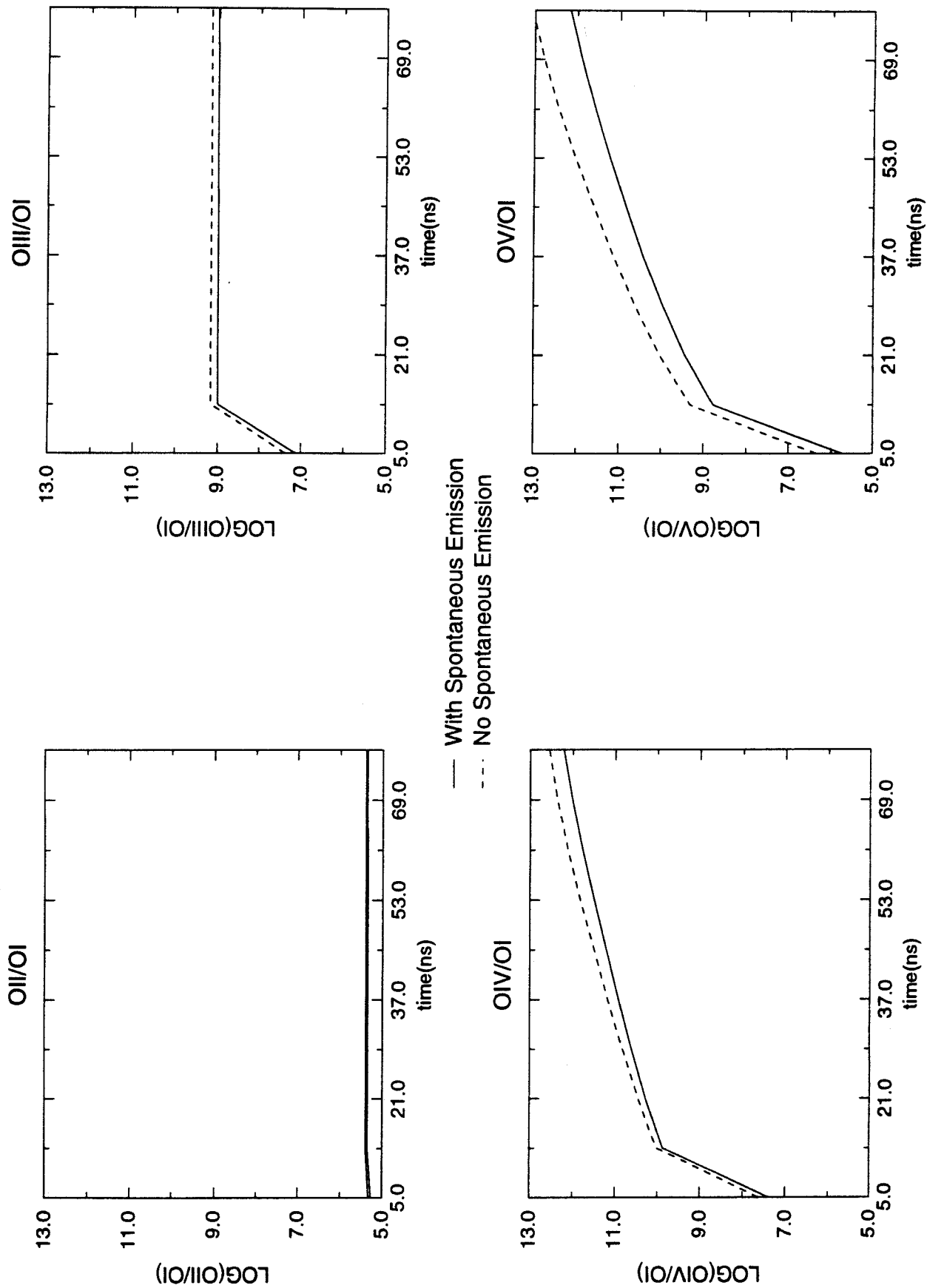
Change in Collisional Rates by a factor of 2 affects significantly
 Populations in higher ionization stages

Te=10eV Ne=1E17



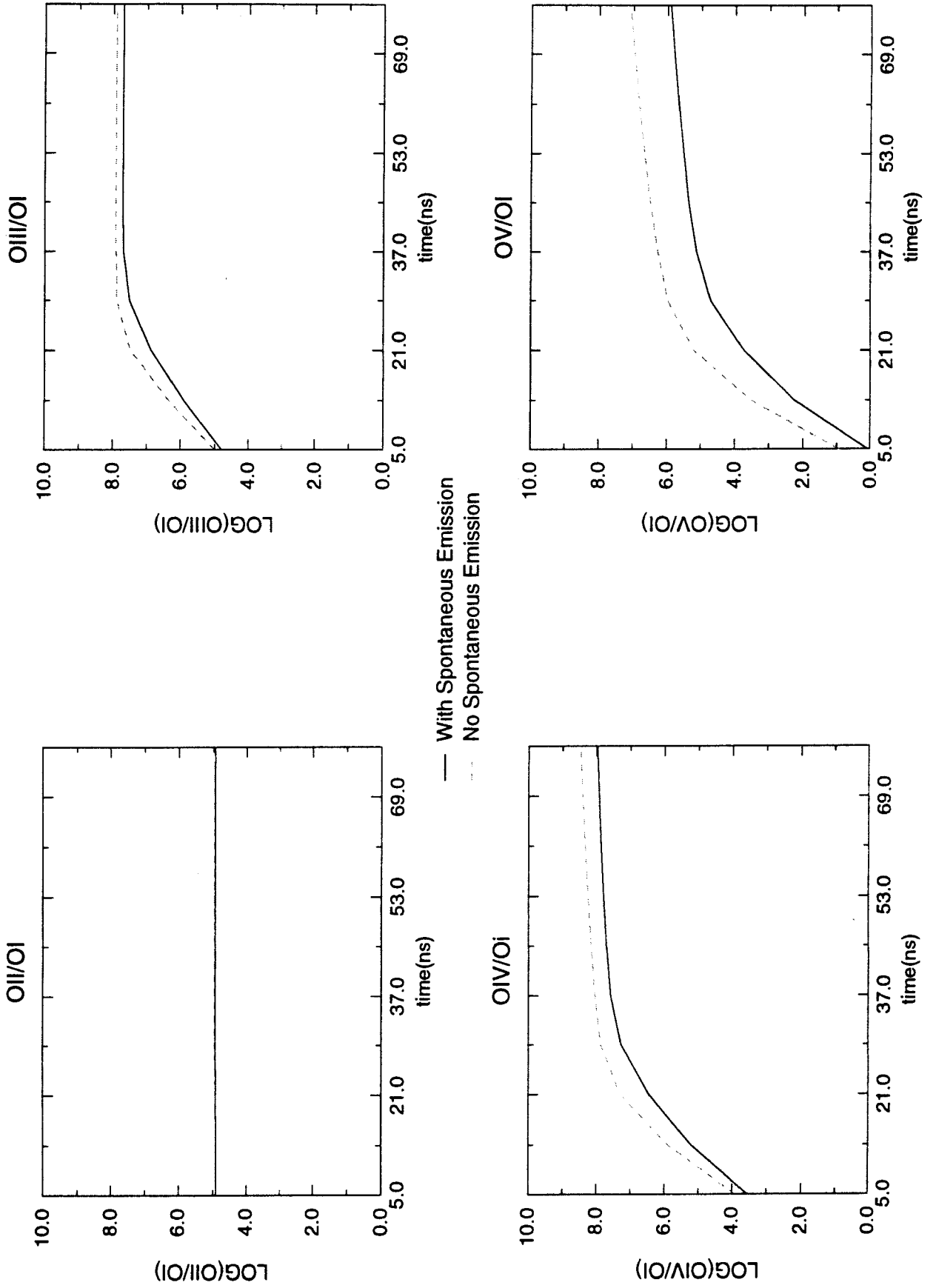
Spontaneous Decay Rate is less significant at higher Temperature

Te=20eV Ne=1E17



Spontaneous Decay Rate is more significant at higher ionization stages

Te=10eV Ne=1E17



SUMMARY and FUTURE WORK

1. We are using a time-dependent collisional-radiative model to analyze VUV spectra obtained from anode plasmas.
2. Preliminary analysis of Oxygen lines in the SABRE experiments suggest;
 $n_e \sim 10^{17} \text{ cm}^{-3}$
 $T_e \sim 20 \text{ eV}$
3. Future calculation will include effects of resonant self-absorption on both the atomic level populations and spectra.
4. We also intend to apply this model to analyze visible and UV spectra obtained from the PBFA-II Argon gas cell to help constrain models of ion beam transport physics.

Appendix B

K_α Spectral Diagnostics for Mg and Al Plasmas Irradiated by Intense Li Beams

In this appendix, we describe K_α spectral calculations for Mg–Al foils heated with intense Li beams. This work was presented at the 10th International Conference on High Power Particle Beams at San Diego, CA, in June 1994. The paper contributed to the proceedings of this meeting is attached.

K_α SPECTRAL DIAGNOSTICS FOR Mg AND Al PLASMAS IRRADIATED BY INTENSE Li BEAMS

J. J. MacFarlane and P. Wang
Fusion Technology Institute
University of Wisconsin
1500 Johnson Drive
Madison, WI 53706

J. E. Bailey, T. A. Mehlhorn, and R. J. Dukart
Sandia National Laboratories
P. O. Box 5800
Albuquerque, NM 87185

Abstract

K_α spectroscopy can be a valuable diagnostic method for determining plasma conditions in ion beam-heated targets. In intense light ion beam experiments, K_α emission lines can be observed as 2p electrons drop down to fill 1s vacancies created by beam-impact ionization. In this paper, we present results from collisional-radiative equilibrium (CRE) calculations for Al and Mg target tracer layers being irradiated by an intense Li beam. Presently, 9 MeV Li beams with power densities of 1-2 TW/cm² can be generated in Particle Beam Fusion Accelerator-II (PBFA-II) experiments at Sandia National Laboratories. It is shown that both emission and absorption K_α spectra show good sensitivity to temperature and density for the range of plasma conditions typically achieved in present PBFA-II experiments.

I. Introduction

K_α satellite spectroscopy has been shown to be a valuable technique in determining plasma conditions in high energy density plasma experiments [1-7]. K_α lines result from electronic 2p ↔ 1s transitions. Thus, in intense light ion beam experiments emission lines can be produced as 2p electrons drop down to fill 1s vacancies created by the ion beam. K_α absorption lines can be seen in the presence of an x-ray backlighter when the target ions have at least one vacancy in

the 2p subshell. Bailey et al. [2] reported the first spectroscopic measurements of K_α x-ray satellites in an intense proton beam experiment. K_α emission spectra have also recently been measured in intense Li-beam experiments on PBFA-II [8].

The purpose of this paper is to show how K_α satellite spectroscopy can be used to diagnose conditions in target plasmas heated by intense Li beams. To do this, we have performed a series of collisional-radiative equilibrium (CRE) calculations to generate K_α emission and absorption spectra for Mg and

Al plasmas. In previous light ion beam experiments, only K_α satellite emission spectra from single-component tracers (i.e., Al) have been used for diagnosing plasma conditions [2,5,8-10]. However, it is expected that multicomponent tracers will be utilized in upcoming experiments to provide additional information for constraining the plasma temperature and density. This paper presents our initial results for Mg/Al tracers.

II. Theoretical Models

Next, we briefly describe the major features of our CRE and atomic physics models. Additional details can be found elsewhere [5,9-11]. Atomic level populations are determined by solving multilevel statistical equilibrium equations self-consistently with the radiation field and ion beam properties. Our atomic models for intermediate-Z tracer elements (here, Mg and Al) typically consist of $\sim 10^3$ energy levels distributed over all ionization stages. Roughly 60% of these are autoionization states with K-shell vacancies. Atomic structure and radiative data are computed using a configuration interaction (CI) model with Hartree-Fock wavefunctions. Ion beam-impact ionization is included in the statistical equilibrium equations, including multiple ionization transitions (i.e., the simultaneous ejection of a K-shell and one or more L-shell electrons). Ion-impact ionization cross sections are computed using a plane-wave Born approximation model with corrections for Coulomb-deflection, binding energy, and relativistic effects. Multiple ionization cross sections are then obtained using an independent event binomial distribution model [11]. Auger rates and fluorescence yields are calculated for each autoionizing level using a LS coupling formalism with Hartree-Fock wavefunctions. Calculated emission and absorption spectra include contributions from bound-bound, bound-free, and free-free transitions. In the calculations

described below, radiation is transported using an escape probability model. Resonant self-absorption effects are included in computing both the photoexcitation rates and the emergent spectra. Line profiles include the effects of natural, Doppler, Auger, and Stark broadening.

III. Results

A series of calculations were performed independently for thin, planar Mg and Al tracers of uniform temperature and density. Temperatures were varied between 30 and 50 eV. In all cases the tracer density was $n = 10^{-3} n_{\text{solid}}$ and the thickness was 200 μm , which corresponds to a 2000 \AA foil which has expanded by a factor of 10^3 . The ion beam was assumed to be composed of Li^{+3} with an energy of 9 MeV per ion. All calculated spectra include instrumental broadening, where a resolution of $\lambda/\Delta\lambda = 1500$ was assumed.

Calculated emission and absorption spectra for K_α satellite spectral region of Mg are shown in Fig. 1. The absorption spectra (shown in lower panels) probe the lower state populations of the K_α bound-bound transitions, and therefore provide a direct measure of the ionization distribution. For instance, B-like and Be-like Mg are the dominant ionization stages at $T = 40$ eV, while Li-like and Be-like Mg are prevalent at $T = 50$ eV. K_α satellite emission spectra (upper panels) reflect the populations of the upper levels of the K_α transitions (i.e., the autoionizing levels), which are populated by ion beam-impact ionization. Because of this, lines from one to two ionization stages higher are seen in emission. For example, the He_α line ($1s2p^1P \rightarrow 1s^2^1S$) and Li-like satellites are strongest in emission at $T = 40$ eV.

Additional information about plasma conditions can be obtained by performing experiments with multi-component tracers.

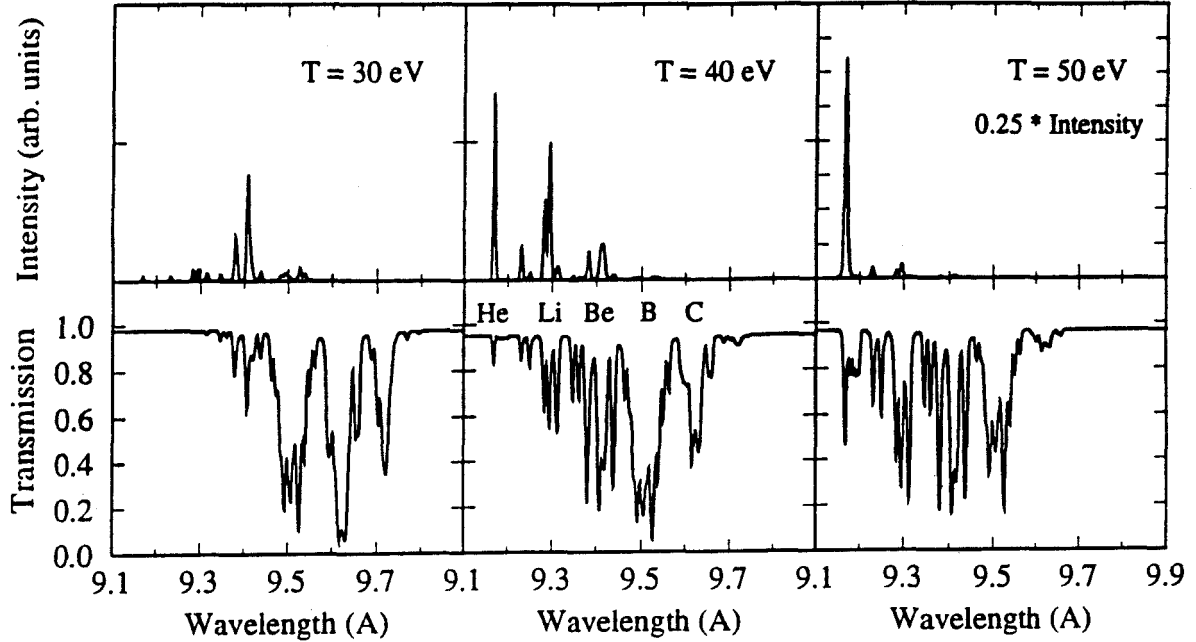


Fig. 1. Calculated Mg K_{α} emission (top) and absorption (bottom) spectra at $T = 30, 40,$ and 50 eV. In each case, $n = 10^{-3} n_{\text{solid}}$ and $L = 200 \mu\text{m}$. The satellite ionization stages are shown with the $T = 40$ eV absorption spectrum. Note the larger scale in the $T = 50$ eV emission plot due to the strong He_{α} line at 9.168 \AA .

Figure 2 shows the K_{α} emission spectrum calculated for Al at $T = 40$ eV, along with the K_{β} absorption spectrum (involving $1s \rightarrow 3p$ transitions) for Mg at $T = 50$ eV. Here, we examine whether K_{α} emission from one of the tracers can be absorbed by the other. Note that in several instances the K_{β} lines of Mg are capable of absorbing K_{α} line emission from Al. In particular the Mg He_{β} line at $\lambda = 7.850 \text{ \AA}$ lies directly between the two strongest Li-like Al K_{α} emission features. Also it is seen that Li-like Mg K_{β} satellites between 8.0 and 8.1 \AA can absorb line radiation from the B-like Al K_{α} satellites. The overlap of part of the Al K_{α} spectrum with the Mg K_{β} satellites, however, need not necessarily lead to significant problems in analyzing the spectra. This is because the K_{α} satellite emission from the highest ionization stages (He-, Li-, and perhaps Be-

like) will most likely be utilized to determine the peak temperatures obtained in light ion beam experiments, in which case only the Mg He_{β} line is capable of producing significant absorption.

Our results therefore indicate that K_{α} satellite emission spectra obtained from two-component Mg/Al tracers should provide enough information to accurately determine target plasma temperatures in the 30 eV to 50 eV range. New data from Mg/Al tracers will be obtained in upcoming PBFA-II Li beam experiments. Similar data will be obtained from NaF tracers in proton beam experiments at the Karlsruhe Light Ion Facility (KALIF) in Germany [12]. We also expect to utilize line intensity ratios from the He-, Li-, and Be-like K_{α} satellites to determine plasma temperatures

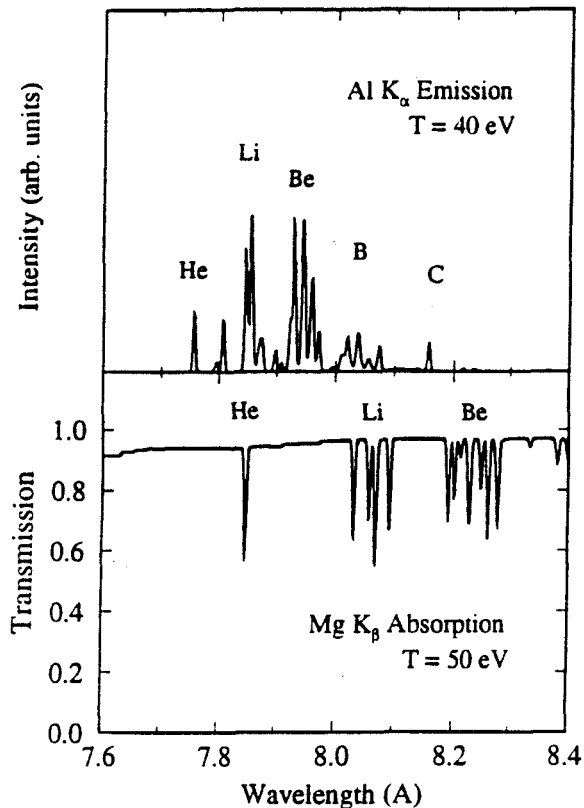


Fig. 2. Calculated Al K_{α} satellite emission spectrum at $T = 40$ eV and Mg K_{β} absorption spectrum at $T = 50$ eV. In each case, $n = 10^{-3} n_{\text{solid}}$ and $L = 200 \mu\text{m}$. Note that at several wavelengths Al K_{α} emission lines can potentially be absorbed by Mg K_{β} lines.

and densities. This work will be described in detail elsewhere [13].

References

1. Nardi, E. and Zinamon, Z., 1981, *J. Appl. Phys.* **52**, 7075.
2. Bailey, J., Carlson, A. L., Chandler, G., Derzon, M. S., Dukart, R. J., Hammel, B. A., Johnson, D. J., Lockner, T. R., Maenchen, J., McGuire, E. J., Mehlhorn, T. A., Nelson, W. E., Ruggles, L. E., Stygar, W. A. and Wenger, D. F., 1990, *Lasers and Particle Beams* **8**, 555.
3. Perry, et al., 1991, *Phys. Rev. Lett.* **67**, 3784.
4. Chenais-Popovics, C., Fievet, C., Geindre, J. P., Gauthier, J. C., Luc-Koenig, E., Wyart, J. F., Pepin, H. and Chaker, M., 1989, *Phys. Rev. A* **40**, 3194.
5. MacFarlane, J. J., Wang, P., Bailey, J., Mehlhorn, T. A., Dukart, R. J. and Mancini, R. F., 1993, *Phys. Rev. E* **47**, 2748.
6. Abdallah, J., Clark, R. E. H., and Peek, J. M., 1991, *Phys. Rev. A* **44**, 4072.
7. Foster, et al., 1991, *Phys. Rev. Lett.* **67**, 3255.
8. Bailey, J. E. et al., 1993, presented at the 6th International Workshop on Atomic Physics for Ion Driven Fusion, Santa Fe, NM.
9. Wang, P., MacFarlane, J. J. and Moses, G. A., 1993a, *Phys. Rev. E* **48**, 3934.
10. MacFarlane, J. J., Wang, P., Bailey, J. E., Mehlhorn, T. A., and Dukart, R. J., 1994, *Lasers and Particle Beams*, in press.
11. Wang, P., MacFarlane, J. J., and Moses, G. A., 1994, *Lasers and Particle Beams*, in press.
12. Goel, B., Ludmirsky, A., Baumung, K., Bluhm, H., Buth, L., Höbel, W., Meisel, G., Rusch, G., Stolz, O., MacFarlane, J. J., and Wang, P., 1994, these proceedings.
13. MacFarlane, J. J., Wang, P., Bailey, J. E., Mehlhorn, T. A., and Dukart, R. J., 1994, in preparation.